UNCLASSIFIED

SECURITY CLASSIFICATION OF THIS PAGE (When Data Entered)

REPORT DOCUMENTATION PAGE	READ INSTRUCTIONS BEFORE COMPLETING FORM
1. REPORT NUMBER: AFOSR-TR-81-0510 / 2. GOVT ACCESSION NO.: AD-A101 C89	3. RECIPIENT'S CATALOG NUMBER
4. TITLE (and Subtitle): COMBINED INFLUENCE OF FREE-STREAM TURBULENCE AND FAVORABLE PRESSURE GRADIENTS ON BOUNDARY LAYER TRANSITION AND HEAT TRANSFER	5. TYPE OF REPORT & PERIOD COVERED: INTERIM, 1 JUN 80-31 MAR 81 / 6. PERFORMING ORG. REPORT NUMBER
7. AUTHOR(s): M. F. BLAIR, M. J. WERLE	8. CONTRACT OR GRANT NUMBER(s): F49620-78-C-0064
9. PERFORMING ORGANIZATION NAME AND ADDRESS: UNITED TECHNOLOGIES RESEARCH CENTER, EAST HARTFORD, CT 06108	10. PROGRAM ELEMENT, PROJECT, TASK AREA & WORK UNIT NUMBERS: 2307/A4, 61102F
11. CONTROLLING OFFICE NAME AND ADDRESS: AIR FORCE OFFICE OF SCIENTIFIC RESEARCH/NA, BOLLING AFB, DC 20332	12. REPORT DATE: April 81 / 13. NUMBER OF PAGES: 91
14. MONITORING AGENCY NAME & ADDRESS (if different from Controlling Office)	15. SECURITY CLASS. (of this report): UNCLASSIFIED / 15a. DECLASSIFICATION DOWNGRADING SCHEDULE

16. DISTRIBUTION STATEMENT (of this Report)

Approved for public release; distribution unlimited.

17. DISTRIBUTION STATEMENT (of the abstract entered in Block 20, if different from Report)

18. SUPPLEMENTARY NOTES

19. KEY WORDS (Continue on reverse side if necessary and identify by block number)

TURBULENT BOUNDARY LAYERS
FREE-STREAM TURBULENCE
TRANSITION
HEAT TRANSFER
BOUNDARY LAYER PROFILES
PRESSURE GRADIENTS

20. ABSTRACT (Continue on reverse side if necessary and identify by block number)

Experimental research was conducted to examine the combined effects of free-stream turbulence and streamwise acceleration on transitional boundary layer flows. During this period convective heat transfer coefficients, boundary layer mean velocity and temperature profile data, and wall static pressure distribution data were obtained for four combinations of streamwise acceleration and free-stream turbulence intensity. Free-stream multicomponent turbulence intensity, longitudinal integral length scale, and spectral distribution

DD FORM 1 JAN 73 1473

4-1082

UNCLASSIFIED

SECURITY CLASSIFICATION OF THIS PAGE (When Data Entered)

data were obtained for the four test cases. The profile results indicate that the data are accurate and consistent and that the experimental boundary layers were highly two-dimensional. The freestream turbulence distributions generated for these tests have been shown to be both homogeneous and nearly isotropic. It is anticipated that these results will provide a needed set of fundamental, well documented experimental test cases to which analytical predictions can be compared. Examinations of the transitional profile shape factors and wall heat transfer distribution data indicate that fully turbulent mean velocity profiles are achieved upstream of fully turbulent wall heat transfer rates. The present data suggest that the turbulent mean velocity profile is established in a shorter length than is required for the development of the equilibrium turbulence distribution. Transition location data obtained in the present program agree very well with data from other flat wall studies. Suggested correlation curves are given for predicting flat wall transition locations with the combined effects of free-stream turbulence and streamwise acceleration.

Also during this period, a boundary layer prediction method has been assessed as to its ability to predict transition with the combined effects of pressure gradient and free-stream turbulence. It was demonstrated that the code provided good predictions of the influence of these effects on the boundary layer kinematic parameters. Prediction of heat transfer was less satisfactory.

UNITED TECHNOLOGIES RESEARCH CENTER

UNITED TECHNOLOGIES

East Hartford, Connecticut 06108

R81-914388-17

Combined Influence of Free-Stream Turbulence and Favorable Pressure Gradients on Boundary Layer Transition and Heat Transfer

Contract No. F49620-78-C-0064
Project Task 2307/A4
61102 F

REPORTED BY M F Blair
M. F. Blair

M J Werle
M. J. Werle

APPROVED BY R E Olson
R. E. Olson

DATE March 1981

NO. OF PAGES _____ COPY NO. _____

FOREWORD

This report was prepared for the Air Force Office of Scientific Research, United States Air Force by the United Technologies Corporation Research Center, East Hartford, Connecticut, under Contract F49620-78-C-0064, Project Task No. 2307/A4 61102 F. The performance period covered by this report was from 1 June 1980 to 31 March 1981. The project monitors were Dr. D. G. Samaras and Dr. James O. Wilson.

The experimental portions of the investigation were conducted in the UTRC Boundary Layer Wind Tunnel. This facility was constructed during 1977 and underwent a series of flow quality evaluation tests during 1978. The UTRC Uniform Heat Flux Flat Wall Model, was also constructed, instrumented, and tested during 1978. Finally, a computer controlled data acquisition system for the UTRC Boundary Layer Wind Tunnel was designed, constructed and made operational during 1978. The construction and evaluation testing of the Boundary Layer Wind Tunnel, Uniform Heat Flux Flat Wall Model, and Data Acquisition system were conducted under UTC Corporate sponsorship.

Contract funded efforts have been devoted to the measurement and analysis of the heat transfer distributions, boundary layer profile and turbulence data presented in this report.

This report covers Tasks C and D of the Statement of Work of the subject contract. Work conducted under Tasks A and B was reported in detail in Ref. 1.

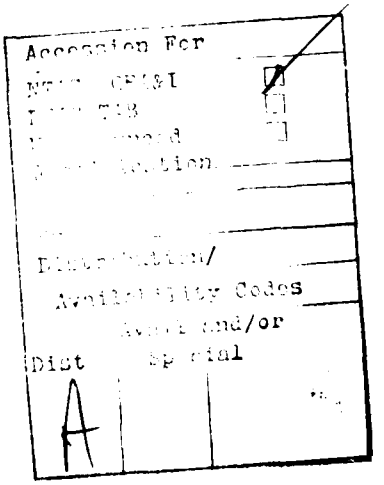

ABSTRACT

During the final year of the contract period experimental research was conducted to examine the combined effects of freestream turbulence and streamwise acceleration on transitional boundary layer flows. During this period convective heat transfer coefficients, boundary layer mean velocity and temperature profile data, and wall static pressure distribution data were obtained for four combinations of streamwise acceleration and freestream turbulence intensity. Freestream multicomponent turbulence intensity, longitudinal integral length scale, and spectral distribution data were obtained for the four test cases. The profile results indicate that the data are accurate and consistent and that the experimental boundary layers were highly two-dimensional. The freestream turbulence distributions generated for these tests have been shown to be both homogeneous and nearly isotropic. It is anticipated that these results will provide a needed set of fundamental, well documented experimental test cases to which analytical predictions can be compared. Examinations of the transitional profile shape factors and wall heat transfer distribution data indicate that fully turbulent mean velocity profiles are achieved upstream of fully turbulent wall heat transfer rates. The present data suggest that the turbulent mean velocity profile is established in a shorter length than is required for the development of the equilibrium turbulence distribution. Transition location data obtained in the present program agree very well with data from other flat wall studies. Suggested correlation curves are given for predicting flat wall transition locations with the combined effects of freestream turbulence and streamwise acceleration.

Also during this period, a boundary layer prediction method has been assessed as to its ability to predict transition with the combined effects of pressure gradient and freestream turbulence. It was demonstrated that the code provided good predictions of the influence of these effects on the boundary layer kinematic parameters. Prediction of heat transfer was less satisfactory.

These data and code assessments fulfill the requirements of Task C and D of the Statement of Work of the subject contract.

R81-914388-17

Combined Influence of Freestream Turbulence and Favorable Pressure Gradients on Boundary Layer Transition and Heat Transfer

TABLE OF CONTENTS

TABLE OF CONTENTS (Cont'd)

INTRODUCTION

Improved techniques for calculating heat transfer coefficient distributions on gas turbine airfoils have been sought by engine manufacturers for the entire history of the industry. These heat transfer distributions must be known so that cooling schemes can be tailored to produce the required metal temperature. Accurate heat transfer predictions are an essential feature of gas turbine design because of the need to maximize performance through minimal use of cooling air and the need to minimize development costs through provision of adequate airfoil cooling on the initial design,

In the design of an airfoil cooling scheme the lack of any required heat transfer distribution information may be compensated for by simply overcooling the component. This overcooling may easily exist since gas turbine thermal design systems are typically not based on fundamental fluid mechanics and heat transfer data and analysis alone but rather are calibrated, or adjusted, to provide agreement with engine experience. Among the more obvious benefits that result from elimination of overcooling are reduced aerodynamic cooling penalties, increased burner and turbine mainstream mass flow rates (i.e., increased power) and potentially reduced cost for the fabrication of the airfoil cooling scheme. Furthermore, without a more complete first-principles understanding there is the likelihood that a designer will unknowingly go beyond the range of validity of the design system calibration. There is, then, a clear requirement for the development of airfoil heat transfer distribution prediction procedures which are based on fundamental fluid mechanics and heat transfer data. The great emphasis placed on the development of accurate boundary layer calculation techniques over the past few years reflects the recognition of these needs.

One particularly important topic in the general context of turbine airfoil convective heat transfer is the influence of the freestream turbulence on both transitional and fully turbulent boundary layer profile development. It has, of course, long been recognized that increasing the freestream turbulence level can cause a forward shift of the laminar to turbulent transition region. This particular phenomenon, the reduction of the boundary layer transition Reynolds number with increased freestream turbulence level, is well documented in the open literature for zero pressure gradient flows and can be accurately predicted with at least one currently available boundary layer prediction scheme. The influence of the freestream turbulence on fully turbulent boundary layers, however, is less certain. A number of investigators have studied the effects of freestream turbulence level on flat wall turbulent boundary layer heat transfer rates and have reported conflicting results. One group of experiments has shown significant effects of the freestream turbulence on heat transfer while a second group has indicated negligible or very small influence. Other experiments which documented the effects of freestream turbulence on boundary layer growth, profile structure, and skin friction

distribution consistently reported very large and important influences. The current contract was conducted in order to clarify these contradictions. Both wall heat transfer and detailed boundary layer profile data were obtained for fully turbulent boundary layers for a range of freestream turbulence levels to provide data which will definitively indicate the influence that freestream turbulence level has on fully turbulent boundary layer heat transfer. In addition, these experimental data were employed to evaluate the turbulence entrainment models currently incorporated in an existing boundary layer calculation technique.

As previously discussed, the effects of freestream turbulence on the zero pressure gradient boundary layer transition Reynolds number are well understood. The influence of the freestream turbulence on the transition process becomes considerably less well defined, however, for cases in which the boundary layer is also exposed to a pressure gradient. The net result of the combined influence of turbulence and pressure gradient is dependent upon the sign of the pressure gradient and the relative strength of the two effects. For adverse pressure gradients both the turbulence and the deceleration promote the transition process and in this case the net result is simply to hasten transition. For favorable pressure gradients, however, the flow acceleration acts to stabilize the boundary layer and tends to counteract the effect of the freestream turbulence. This interplay of pressure gradient and turbulence results in at least two effects on the transition process: (1) the location of the onset of transition is influenced and (2) the length and character of the transitional boundary layer flow region may be altered significantly. At the present time, only very limited experimental data documenting these effects are available. To further complicate the matter, much of the currently available data are contradictory making it impossible to assess the relative quality of boundary layer calculation techniques for these flows. For these reasons, as part of the present contract both wall heat transfer and detailed velocity and temperature profile data were obtained for accelerating transitional boundary layer flows exposed to high freestream turbulence levels. These data were utilized to evaluate the current capability of an existing boundary layer calculation procedure to predict boundary layer development with combined favorable pressure gradients and high freestream turbulence levels.

The present contract program provides wall heat transfer and detailed mean boundary layer profile development data required to determine the influence of freestream turbulence level on both fully turbulent and accelerating transitional boundary layers. These data are fundamental in nature and can be employed by both UTRC and other workers in the field of boundary layer computation for evaluation of analytical models. In addition, the contract experiments provide a valuable body of detailed heat transfer and boundary layer profile data directly relevant to the problem predicting heat transfer distributions on gas turbine airfoils. Finally, as mentioned above, the information could result in more accurate blade heat transfer distribution prediction techniques and thereby the more efficient use of blade cooling air.

The contract effort consisted of the documentation and analysis of experimental flat wall boundary layer profile and heat transfer data to determine the influence of freestream turbulence on transitional and fully turbulent boundary layer flows. For fully turbulent, zero pressure gradient boundary layer flows the following data were obtained for a range of freestream turbulence intensities: convective heat transfer coefficients; boundary layer mean velocity and temperature profiles; test wall static pressure distributions and freestream turbulence intensity, spectral and longitudinal integral scale distributions. These same measurements were obtained for various combinations of favorable pressure gradients and freestream turbulence levels for transitional boundary layer flows. From these data the integral properties of the test boundary layers were calculated and, where applicable, the profile data were reduced to the "universal" coordinates for turbulent boundary layers U^+, Y^+ and T^+. Finally, the measured heat transfer distributions and boundary layer profile development were compared to predictions of the UTRC Finite-Difference Boundary Layer Deck. These comparisons were employed to evaluate the computation methods currently incorporated in the UTRC deck.

DESCRIPTION OF TEST EQUIPMENT

1. UTRC Boundary Layer Wind Tunnel

All experimental data for the present investigation were obtained in the United Technologies Research Center (UTRC) Boundary Layer Wind Tunnel. complete description of this facility is given in Ref. 2. This tunnel was designed for conducting fundamental studies of two-dimensional, incompressible flat wall boundary layer flow. Incorporated in the tunnel is a versatile, adjustable test section constructed so that laminar, transitional, or turbulent boundary layers can be subjected to favorable, zero, or adverse pressure gradients. In addition, test boundary layers can be subjected to a wide range of freestream turbulence levels. Low freestream turbulence flows can be investigated in this facility since it is designed to have a very low residual test section turbulence level. Higher turbulence levels can be generated within the test section through the use of various rectangular grids.

An overall sketch of the Low Speed Boundary Layer Tunnel is shown in Fig. 1. The tunnel is of recirculating design and consists of a blower, a settling chamber/plenum, a contraction nozzle, the boundary layer test section, a downstream diffuser, and a return duct. The settling chamber/plenum consists of a series of perforated part span baffles which even out gross irregularities in the flow from the blower and a honeycomb which removes large-scale flow swirl. Downstream of the honeycomb are a series of fine mesh damping screens which progressively reduce both the flow nonuniformity and the residual tunnel turbulence level. A nozzle with a 2.8:1 contraction ratio mounted downstream of the damping screens accelerates the flow to produce the required test section Reynolds number. Following the contraction nozzle the flow passes through the 34-in. wide flat wall boundary layer test section. At the entrance to the test section an upstream facing scoop bleed assembly forms the leading edge of the boundary layer test surface. The purpose of this leading edge bleed scoop is to divert all the flow near the tunnel upper wall. With this arrangement the test section flow consists of the uniform "core" flow from the main contraction nozzle. A sketch showing details of the scoop assembly is presented in Fig. 2. The scoop assembly consists of a two-stage leading edge adjustable bleed and, as shown in Fig. 2, is attached to the flat wall boundary layer test surface. The upstream and by far the larger of the two scoops diverts the flow nearest the upper wall of the contraction exit duct. This large scoop is intended to trap both the two-dimensional boundary layer which develops along the contraction nozzle wall and the vortices which develop in the contraction corners. The flow rate along the scoop opening is adjusted by locally restricting protions of the perforated plate located at the scoop exit (see Fig. 2). The local scoop flow rate can be adjusted to produce uniform pressure (in the transverse direction) at the static taps along the entire scoop. The downstream and much smaller of the two scoops is mounted directly on the front edge of the Uniform Heat Flux Flat Wall Model. The test

section boundary layer begins growing at the leading edge of this smaller scoop. The purpose of this small-scale second scoop is to provide as short an unheated starting length upstream of the heated test surface as practical by bleeding off any boundary layer which develops along the large scoop lip. As with the larger upstream scoop the flow rate along the small scoop is adjusted by locally restricting portions of the perforated plate located at the small scoop exit (see Fig. 2). The leading edge of the small downstream scoop is a 4 x 1 ellipse shape in order to prevent a local separation bubble and a premature transition of the test surface boundary layer. As shown in both Figs. 1 and 2, the flow diverted by the leading edge scoop assembly is returned to the main tunnel loop through a small duct.

The main test section of the Boundary Layer Tunnel consists of the flat upper wall test surface, a lower flexible, adjustable stainless steel wall and transparent vertical sidewalls. The vertical sidewalls were constructed of plexiglass to facilitate positioning of boundary layer probes and for purposes of conducting flow visualization studies. Downstream of the test section a diffuser/corner combination reduces the test section velocity and delivers the flow to the return duct. Mounted in this return duct are an air filter and a liquid chilled heat exchanger which controls and stabilizes the tunnel air temperature at approximately 70°F.

Higher turbulence levels required for this investigation can be generated within the test section by installing coarse grids at the entrance to the tunnel contraction (see Fig. 1). Four rectangular bar turbulence generating grids were designed and fabricated for use in this investigation. These grids were designed, using the correlations of Ref. 3 to produce test section total turbulence levels ranging from approximately 1 to 7 percent. A diagram of the turbulence generating grid configurations including all pertinent grid dimensions is presented in Fig. 3. Photographs of the four assembled grids are presented in Fig. 4. For Grid Nos. 1 and 2 (small bars) a locating jig was employed to secure the grid bars at precise intervals while the bars were welded at their intersections. This step assured that the grid configurations were both permanent and uniform over their entire area. For Grid Nos. 3 and 4 (larger bars) the rectangular bars are very rigid making this unnecessary. The tunnel, then, can be operated with 5 different levels of freestream turbulence in the test section; (1) no turbulence grid installed (minimum turbulence level), and (2) through (5) with Grid Nos. 1 through 4 installed at the contraction entrance.

A photograph of the Boundary Layer Wind Tunnel is presented in Fig. 5. Also shown in Fig. 5 are both the telescope used to position probes relative to the test wall and the computer controlled probe transverse mechanism.

2. Uniform Heat Flux Flat Wall Model

As discussed in the Boundary Layer Wind Tunnel description, the test boundary layer development begins at the leading edge of the small bleed scoop and continues along the flat test wall. For these present studies the flat wall test surface consists of an electrically heated plate instrumented for the measurements of local convective coefficients. This heated test surface is designed to produce a nearly uniform heat flux distribution over its entire surface and will be referred to as the Uniform Heat Flux Flat Wall Model. This flat wall model consists of a block of rigid urethane foam 34-in. wide by 96-in. long by 4-in. thick mounted in a plexiglass frame with 6-in. wide strips of metal foil cemented to the test surface. A sketch of the Flat Wall Model and its instrumentation is presented in Fig. 6. Rigid foam was employed for the substrate of the Flat Wall Model because of its extremely low thermal conductivity (k = 0.025 Btu/hr ft °F). Because of this low foal conductivity less than 1/2 percent of the heat generated on the surface of the plate is conducted through the model wall.

Electric current passing through the metal foil strips cemented to the Flat Wall Model test surface produces the surface heating. The metal foil strips are wired in series and are powered by a single low ripple, regulated dc power supply. Use of series wiring assures that precisely the same current passes through each of the metal foil surface strips. The metal foil employed for the model surface was 316 stainless, "3/4 hard" temper, 0.0012-in. thick by 6.00-in. wide. The temperature-resistance characteristics of three samples of this foil were determined using an Electro Scientific Industries 1701 B Precision Ohmmeter. A low temperature oven was used to control the temperature of the foil samples. Resistance data obtained for the three samples are presented in Fig. 7. The extremely small scatter for these data indicates that for any test surface temperature the local foil resistance can be calculated within an accuracy of 1 percent using the following expression:

$$R_{foil} = R_{ref} \left(1 + \alpha_{ref} \left(T_{foil} - T_{ref}\right)\right) \qquad (1)$$

where

$T_{ref} = 71°F$

$R_{ref} = 0.0500\ \Omega/ft\ @\ 71°F$

$\alpha_{ref}\ @\ 71°F = 0.000504\ \Omega/°F$

The foil test surface is instrumented with an array of 203 Cr-Al 0.005 in. wire diameter bead welded thermocouples. The thermocouple array is shown in Fig. 6. Each thermocouple was welded to the back surface of the foil through a hole in the rigid foam plate. Welding the thermocouple beads directly to the foil insures that the local foil temperatures can be accurately measured.

In order to insure a known, constant test surface emissivity and hence a known radiation loss the completed foil test surface was coated with 3M C-101 high emissivity flat black paint ($\varepsilon = 0.99$). Forty-eight surface static pressure taps were also installed in the Flat Wall Model. The locations of these static taps are shown in Fig. 6.

Photographs of the Uniform Heat Flux Flat Wall Model at various stages of completion are presented in Figs. 8, 9 and 10. Figure 8 shows the plexiglass frame for the Flat Wall Model prior to casting the rigid urethane foam wall. A photograph of the back surface of the Flat Wall Model is presented in Fig. 9. This photograph shows the leading edge scoop lip mounted on the front edge of the model and the routing of the thermocouple and static pressure leads. Figure 10 shows the test surface of the model before it was coated with high emissivity black paint. In Fig. 10 the surface foil strips have been connected to their respective buss bars. The buss bar/strip circuit is arranged in series so that the total power current passes through each individual strip.

The dc power current passing through the surface strips is measured using two precision shunt resistors and a digital voltmeter. The temperature of the test surface thermocouples are measured relative to a single test section freestream reference junction using a digital voltmeter.

The local generated power on the test surface is determined by measuring the local wall temperature, T_w, and calculating the local dissipation.

$$q_{power} = I^2 R_{foil} = I^2 R_{ref} (1 + \alpha_{ref} (T_w - T_{ref})) \qquad (2)$$

The local convective coefficient can then be determined by ignoring the negligible conduction losses, subtracting that power lost through thermal radiation, and dividing by the temperature difference from the wall (T_w) to the freestream (T_e).

$$h = \frac{q_{power} - q_{radiation}}{T_w - T_e} \qquad (3)$$

As an example to illustrate the magnitude of the radiation losses from the test surface, for $U_e = 100$ fps, for turbulent boundary layer flow with $T_w - T_e = 25°F$, the radiation loss is approximately 4 percent of the total surface power. Aside then, from the small differences in local dissipation and radiation reflected by Eqs. (2) and (3), respectively, the test surface produces uniform convective heat flux for turbulent flow test cases.

3. Test Section Inserts

Two test section inserts, to be installed opposite the heated flat wall test plate, were designed to produce flows with a nearly-constant acceleration parameter ($K = \nu/U^2\ \partial U/\partial X = 0.2$ and 0.75×10^{-6}, wedges 1 and 2 respectively). These two test section inserts, sketches of which are shown in Fig. 11, consist of simple wedge-shaped bodies with a 2 in. long steeper wedge attached to the leading edge. These "modified shape" wedges were designed, using the inviscid potential flow analysis of Ref. 4 to provide a near constant acceleration of the test section flow along the entire test wall. Important dimensions of the two wedge inserts are given in Fig. 11. Probe transverse slots, aligned with slots in the test section bottom wall, have been incorporated into the wedge inserts.

4. Instrumentation

Boundary layer mean velocity profile data were measured using United Sensor Model BA-0.020 impact probes with flattened tips. A photograph of a typical probe is presented in Fig. 12. The probes used in the program were inspected using both a Nikon Model II toolmakers microscope and a Jones and Lamson Model PC14 Shadowgraph. Probe dimensions obtained with these instruments are included in Fig. 12.

Mean temperature data were measured with miniature thermocouple probes designed using the results of Ref. 5. Photographs of thermocouple probes No. 1 and 2 are presented in Fig. 13. The thermocouple sensing element for these probes was constructed from 0.001 in. dia Chromel-Alumel bead welded wires. The thermocouple bead ($\approx$ 0.003 in. dia) is located at the center of the probe support prongs which are fabricated of heavier Chromel and Alumel wire. The results of Ref. 5 indicate that a probe of this design will be virtually free of wire conduction errors and is capable of measuring boundary layer mean temperature profile data into the viscous sublayer region.

5. Data Acquisition System

Experimental data for the UTRC Boundary Layer Wind Tunnel is recorded using a data acquisition system specifically designed for this facility. This data acquisition system is capable of recording time mean analog signals from the various pressure, temperature and hot wire/hot film probes and test section transducers used in the facility. In addition, the system controls the movement of the various boundary layer probes through the use of an L.C. Smith ball/screw traverse drive linked to an InterData Model 6/16 computer. Signals from the various probes are recorded using InterData magnetic disks. The data system consists of two units (1) a console containing the InterData computer and disk recording unit and a Perkin-Elmer Model 1100

scope/keyboard control terminal, and (2) a remote cabinet unit, linked by cables to the console unit, which contains the sensor transducers and traverse controls. The computer cabinet is relatively mobile and can be moved to convenient locations near the tunnel test section. A photograph of Units 1 and 2 of the data acquisition system is presented in Fig. 14. Also, in Fig. 5 (tunnel test section photograph) the remote unit can be seen at the downstream end of the test section.

DATA ACQUISITION AND ANALYSIS TECHNIQUES

1. Description of the Hot Film Anemometer and Signal Processing System

Measurements of the turbulence quantities downstream of the various generating grids were obtained with single and X hot film probes and their associated anemometry. These data include measurements of the multi-component (u', v', and w') distributions of turbulence intensity and measurements of the streamwise component (u') distirbutions of the integral scale and power spectral density. Complete descriptions of the anemometer and signal processing equipment and the techniques employed to reduce and interpret the measured quantities can be found in Ref. 1. Descriptions of the following are included in Ref. 1: (1) Measurement of Multi-Component Turbulence with an X hot Film Array, (2) Calibration of the Single Film and X Film Probes, and (3) Measurement of the Length Scale and Spectral Distribution Data.

A block diagram of the various anemometers, signal processing circuits, and voltmeters used to obtain the multi-component turbulence measurements is presented in Fig. 15. For measurements of the u' and v' components (streamwise and vertical fluctuations) the X film array was oriented in a plane parallel to the streamwise direction and perpendicular to the horizontal test wall. For measurements of the u' and w' components (streamwise and transverse fluctuations) the X film array was oriented in a plane parallel to the streamwise direction and parallelto the horizontal test wall.

Measurements of the turbulent length scales and spectral distributions were obtained using single-sensor hot film probes. For all these data the hot-film probes were powered by a TSI Model 1050 Constant Temperature Anemometer, the output of which was linearized using a TSI Model 1052 4th order polynomial linearizer. Measurement of the length scales was accomplished by generating autocorrelations of the linearized hot-film signals using a Saicor Model SAI-42 Correlator and Probability Analyzer. The power spectral density distributions were determined using a Spectral Dynamics Model SD 340 MICRO FFT narrow band analyzer. A block diagram of the instrument arrangement used to measure these autocorrelations and spectral density distributions is presented in Fig. 16.

2. Boundary Layer Data Analysis

A complete description of the analysis techniques used to interpret both the mean velocity and temperature boundary layer profile data of the present program can be found in Ref. 1. This description includes detailed information concerning the analytical foundations of the boundary layer data reduction techniques.

A computer program has been written which reduces, plots, and tabulates the velocity and temperature boundary layer profile data obtained by the UTRC Boundary Layer Wind Tunnel Data Acquisition System. Following is a brief description of this reduction program for (a) mean velocity, (b) friction velocity and (c) integral parameters.

(a) Mean velocities (U) are measured with miniature flattened pitot probes. These velocities are corrected for probe Reynolds number and wall blockage effects using the results of Refs. 6, 7, and 8. Except for those measurements extremely close to the wall ($y \sim < 0.010$ in.) the corrections were less than 1% of the measured velocity. The maximum velocity correction (5%) resulted for the case of the probe touching the wall.

(b) Friction velocities (U_τ) for each profile are determined by a least squares fit of the velocity profile data from $50 \sim < y+ \sim < 500$ to the "law-of-the-wall" (Eq. 4)

$$\frac{U}{U_\tau} = \frac{1}{\kappa} \ln \frac{yU_\tau}{\nu} + C \tag{4}$$

where $\kappa = 0.41$
$C = 5.0$
as recommended by Coles (Ref. 9).

Using this value of U_τ the velocity and temperature data are plotted in universal coordinates $U^+ = \frac{U}{U_\tau}$ and $t^+ = \frac{(t_w - t)\rho_w C_p \sqrt{\tau_w/\rho}}{q_w}$ vs $y^+ = \frac{yU_\tau}{\nu}$. The velocity profile data are compared with Eq. (4) and the temperature data with Eq. (5).

$$t^+ = Pr_t \left(\frac{1}{\kappa} \ln y^+ + C + P_s \right) \tag{5}$$

where $Pr_t = 0.9$
$\kappa = 0.41$
$C = 5.0$
$Ps + -2.0$

(c) The following integral properties are determined

(i) displacement thickness $\delta^* = \int_0^\delta \left(1 - \frac{\rho U}{\rho_e U_e} \right) dy$

(ii) momentum thickness $\theta = \int_0^\delta \frac{\rho U}{\rho_e U_e} \left(1 - \frac{U}{U_e} \right) dy$

(iii) energy-dissipation thickness $\delta^{**} = \int_0^\delta \frac{\rho U}{\rho_e U_e} \left(1 - \frac{U^2}{U_e^2} \right) dy$

(iv) enthalpy thickness $$\delta_H = \int_0^{\delta_1} \frac{\rho U}{\rho_e U_e} \left(\frac{T - T_e}{T_e}\right) dy$$

(v) kinematic displacement thickness $$\delta_K^* = \int_0^{\delta} \left(1 - \frac{U}{U_e}\right) dy$$

(vi) kinematic momentum thickness $$\theta_K = \int_0^{\delta} \frac{U}{U_e} \left(1 - \frac{U}{U_e}\right) dy$$

(vii) Clauser delta $$\Delta = \int_0^{\delta} \left(\frac{U_e - U}{U_\tau}\right) dy$$

(viii) Clauser shape parameter $$G = \frac{1}{\Delta} \int_0^{\delta} \left(\frac{U_e - U}{U_\tau}\right)^2 dy$$

Measurement of velocity profile data very close ($y+ \lesssim 30$) to a wall is difficult because of the extremely large local velocity gradients and the finite probe tip size. For the velocity profiles measured in this program a flattened impact probe with a probe tip height of approximately 0.007 in. (see instrumentation section) is employed. This tip height corresponds to $\Delta y+ \approx 10$ for most of the profiles (depending on the individual profile U_τ). Because the true distance from the wall to the effective center of the probe tip is uncertain (uncertainty of approximately $\pm$0.001 in.) the recommendation of Coles (Ref. 10) has been followed and the integral thicknesses are evaluated using standard sublayer functions very close to the wall. For values of $y+ < 35$ (approximately three probe tip heights) the integral thicknesses are evaluated using the standard velocity sublayer and buffer zone function (Eq. (6)) of Burton (Ref. 11).

$$y^+ = U^+ + \left(\frac{U^+}{8.74}\right)^7 \tag{6}$$

The thermocouple boundary layer probes, as described in the instrumentation section, are constructed with 0.001-in.-dia sensing elements. Because of this design, accurate temperature data can be obtained very close to the wall (for some profiles even within the viscous sublayer). For this reason it has been possible to use measured temperature data for evaluation of the integral thicknesses from $y+ = 5$ to the edge of the boundary layer. For $y+ < 5$ (viscous sublayer) the integral thicknesses are evaluated using Eq. (7).

$$t^+ = Pr\, U^+ \tag{7}$$

WIND TUNNEL FLOW QUALITY EVALUATION TESTS

1. Total Pressure Uniformity Surveys

Surveys of the total pressure distribution in the tunnel test section core flow were obtained for all 5 tunnel turbulence configurations using a traversing impact probe. A complete description of these measurements can be found in Ref. 1.

Assuming that the static pressure across the measurement planes is uniform, these total pressure measurements indicate that the following maximum non-uniformities in core flow velocity were associated with the various grids:

% NONUNIFORMITIES AT THE TEST WALL LEADING EDGE

Grid Number	$\frac{P_{T_{MAX}} - P_{T_{MIN}}}{2q}$ (%)	$\frac{\approx \pm U}{U}$ (%)
no grid	0.5	0.25
1	1.0	0.5
2	1.0	0.5
3	3.4	1.7
4	4.0	2.0

The conclusion reached from these results is that, on the scale of the tunnel test section, the flow through the various grid configurations is extremely uniform. The turbulence grids appear to have been fabricated precisely (even bar spacing) and to produce uniform flow resistance over their surfaces.

2. Flat Wall Heat Transfer Distributions (Evaluation Tests)

Stanton number distributions measured on the Uniform Heat Flux Wall for constant nominal free-steam velocities of 40 and 100 fps are presented in Fig. 17. Examination of Fig. 17 reveals that for the nominally 100 fps test case the measured heat transfer distribution, upstream of boundary layer transition ($Re_x < 1.2 \times 10^6$, $x < 23$ in.), agrees very well with the analytical solution of Ref. 12 (Equation 8 below) for zero pressure gradient, laminar boundary layer flow with a uniform convective heat flux wall and an unheated starting length ξ. For this test plate $\xi = 1.69$ in.

$$St\ Pr^{2/3} = 0.453\ Re_x^{-1/2}\ \left[1 - (\xi/x)^{3/4}\right]^{-1/3} \qquad (8)$$

For the 40 fps test case the measured heat transfer distribution agreed with Eq. 8 within approximately 5 percent from the beginning of wall heating ($x = \xi = 1.69$ in) to $Re_x \approx 5 \times 10^5$ ($x = 25$ in.). Between $Re_x \approx 5 \times 10^5$ and $Re_x \approx 1.1 \times 10^6$ (where the test boundary layer underwent transition), the measured heat transfer was up to 10 percent less than was calculated by the uniform heat flux prediction of Eq. 8. This deviation from Eq. 8 is a result of significant surface radiation heat losses present for the 40 fps test case. Unlike the example of high speed turbulent boundary layer flow cited earlier, for the case of low speed laminar boundary layer flow the convective coefficient drops to extremely low values and surface radiation losses become large. For the 40 fps test case at $Re_x = 1 \times 10^6$ nearly 50 percent of the power being generated on the test surface was lost through thermal radiation. Because of these relatively large test wall radiation losses in the 40 fps test case, the convective heat flux progressively and significantly decreases with increasing x. As a result of these radiation losses, the uniform convective heat flux solution (Eq. 8) is inappropriate for the 40 fps test case. A prediction of the Stanton-number distribution for the 40 fps test case was computed using the UTRC Finite-Difference Boundary Layer Computation code. The code was used to predict a laminar boundary layer flow with the convective wall heat flux distribution present for the actual experimental test case. A comparison of this prediction, also shown in Fig. 17, and the measured distribution shows excellent agreement.

Downstream of $Re_x \approx 1.2 \times 10^6$ the test wall boundary layers passed through transition for both the 40 and 100 fps cases. From $Re_x \approx 1.68 \times 10^6$ to the downstream end of the plate the measured heat transfer data agreed within approximately ± 3 percent with the fully turbulent correlation of Ref. 12.

$$St\ Pr^{0.4} = 0.0307\ Re_x^{-0.2}\ \ (Tw/Te)^{-0.4} \qquad (9)$$

The conclusion reached from Fig. 17 is that there is excellent agreement, even at very low freestream velocities, between low freestream turbulent heat transfer data measured in this facility and the appropriate analytical predictions or established data correlations.

3. Laminar Boundary Layer Profiles (Evaluation Tests)

Mean velocity and temperature profile data were measured in the laminar flow upstream of boundary layer transition for the 100 fps test case of the preceding section. Profile data were obtained at three transverse positions at equal distance from the plate leading edge. These profiles, presented in Fig. 18, were obtained on the tunnel centerline and at stations 6 in to the east and west of the tunnel

centerline at x ≈ 12 in, $Re_x = 0.63 \times 10^6$. The measured velocity and temperature profile data agree extremely well with the laminar boundary layer profile solutions of Blasius (velocity, Ref. 13) and Levy (temperature, Ref. 14) and show negligible transverse variations. The conclusion reached from Fig. 18 is that these profile data are consistent with the wall heat transfer data of the preceding section. Both the heat transfer and profile data indicate that the test boundary layer was highly two-dimensional at that at x = 12 in it was still laminar.

EXPERIMENTAL RESULTS

1. Test Section Velocity and Acceleration Distributions

Sample freestream velocity distributions for the two acceleration configurations are presented in Figs. 19 and 20, both of which were obtained with no turbulence grid installed in the tunnel. Velocity distributions measured with the same wedge configurations but turbulence Grid Nos. 1 through 4 installed agreed within $\pm$ 1 percent of the data of Figs. 19 and 20 are omitted for clarity. Acceleration configurations 1 and 2 were designed to produce "sink" or constant acceleration parameter flows. Idealized "sink" flow is represented in the following sketch.

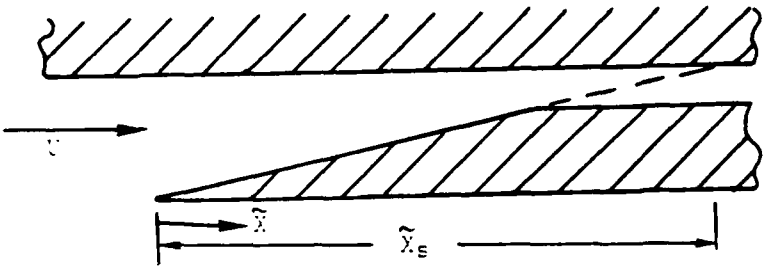

where $\tilde{X}$ is the distance from the beginning of acceleration and $\tilde{X}_s$ is the distance to the potential "origin". The velocity distribution for idealized sink flow is

$$U = C(\tilde{X}_s - \tilde{X})^{-1}$$

The velocity distribution produces a constant acceleration parameter

$$K = \nu/U^2 \ \partial U/\partial \tilde{X} = \nu/C = \text{constant}$$

An examination of Figs. 19 and 20 reveals that the flows generated in the two acceleration configurations closely approximate ideal sink flow. Test boundary layers developing along the heated flat wall will be subjected to nearly constant acceleration. The velocity ratio curve plotted for Fig. 19 is the analytical relationship determined from the velocity distribution data:

$$U = 14{,}800\ (200 - X)^{-1.066}$$

where U is in ft/sec and X is in inches. The acceleration parameter K was calculated using this same analytical relationship. As shown in Fig. 19 the acceleration parameter is nearly constant along the entire test wall with a value very near the design target of $K = \nu/U^2\ \partial U/\partial X = 0.2 \times 10^{-6}$.

For Fig. 20 the velocity ratio and acceleration plots are calculated from the relationship

$$U = 3780\ (83.3\text{-}X)^{-1.075}$$

where again U is in ft/sec and X is in inches. The streamwise acceleration parameter is nearly constant along the entire test wall with $K = 0.75 \times 10^{-6}$.

2. The Experimental Test Matrix

Convective heat transfer coefficients, boundary layer mean velocity and temperature profiles, wall static pressure distributions and free-stream turbulence intensity, spectral and longitudinal integral scale distributions were measured for the following four acceleration/turbulence combinations:

Flow Condition (1) $K = 0.20 \times 10^{-6}$; Grid No. 1
Flow Condition (2) $K = 0.20 \times 10^{-6}$; Grid No. 2
Flow Condition (3) $K = 0.75 \times 10^{-6}$; Grid No. 2
Flow Condition (4) $K = 0.75 \times 10^{-6}$; Grid No. 3

These particular combinations were selected to cover a wide range of both acceleration parameter and turbulence intensity. Two turbulence levels were studied at each acceleration level while one of the turbulence grids was common to both acclerations.

K	Flow Condition No.	Grid No. 1	Grid No. 2	Grid No. 3
	0.20×10^{-6}	1	2	
	0.75×10^{-6}		3	4

21

As discussed in the previous subsection the velocity distribution for a given wedge was not significantly influenced by changes in the turbulence level. It will be shown in a following section, however, that the turbulence generated by Grid No. 2 was affected by the acceleration level. Note then that while the acceleration level

is practically identical between flow conditions 1 and 2 and 3 and 4 respectively the turbulence intensity distributions are somewhat different for configurations 2 and 3 even though both employed Grid No. 2.

3. Free-Stream Turbulence Distributions in the Wind Tunnel Test Section

3.1 Intensity and Length Scale Measurements at the Test Section Entrance Plane

The purpose of the present subsection is to demonstrate the consistency of both the tunnel/grid performance and the turbulence measurement techniques. In this subsection comparison are made between turbulence intensity and length scale measurements obtained at the test section entrance plane for a number of tunnel velocity/grid combinations. Data were obtained in both the present study and two earlier projects (Refs. 1 and 15). The test section entrance plane is located 12 inches upstream of the test wall leading edge (at the nozzle exit) and is well upstream of the beginning of test section flow acceleration for both the present study and the study of Ref. 15. Turbulence measurements were also obtained under the present contract at this location for zero pressure gradient test section flow (Ref. 1). Since the test section entrance plane is well upstream of any flow acceleration imposed in the test section, valid comparisons can be made between the entrance plane turbulence measurements obtained for these various test configurations. The following table lists the velocity/grid combinations and the type of data obtained.

TURBULENCE MEASUREMENTS AT THE TEST SECTION ENTRANCE PLANE

Velocity at Test Section Entrance (ft/sec)	Grid No.	Measurements Obtained	Reference
51	1	T, Λ	Present Study
51	2	T, Λ	Present Study
32	2	T, Λ	Present Study
32	3	T, Λ	Present Study
100	1	T, Λ	1
100	2	T, Λ	1
100	3	T, Λ	1
22.5	2	T	15

The turbulence intensity measurements for these various tests are presented in Fig. 21a. This figure indicates that the turbulence levels measured for each grid are nearly constant over a wide range of tunnel velocities. This result agrees with the data and recommended correlations of Ref. 3. Figure 21b presents the stramwise integral scale measurements obtained for the various tests. As with the turbulence

intensity data the streamwise integral scale measurements for each grid are nearly independent of tunnel speed. Results from a recent comprehensive study of grid generated turbulence (Ref. 16 - Fig. 31) also indicate that streamwise length scale is not speed dependent. The conclusion reached from Figs. 21a and b is that the data taken in the UTRC tunnel for the various velocity/grid combinations are in agreement with the results from other investigators. In addition, the self-consistency of the results from the present facility indicates that the experimental techniques employed to obtain these measurements are highly accurate.

3.2 Test Section Turbulence Intensity Distributions

As previously described, turbulence intensity measurements were obatined with X film probes and an associated anemometry system. The u' (streamwise) and v' (vertical) components of the turbulence were measured with the X film array oriented in a plane parallel to the streamwise direction and perpendicular to the horizontal test wall. For measurements of the u' (streamwise) and w' (transverse) components the X film array was oriented in a plane parallel to the streamwise direction and perpendicular to the horizontal test wall. Turbulence distributions were obtained for all four acceleration/turbulence grid flow conditions. For both wedge 1 ($K = 0.20 \times 10^{-6}$) and 2 ($K = 0.75 \times 10^{-6}$) surveys of the turbulence distributions were obtained over five planes located at the following streamwise distances from the test wall leading edge: for wedge 1 the surveys were obtained at X = -12, 4, 16, 40 and 64 inches; for wedge 2 the surveys were obtained at X = -12, 4, 16, 28 and 52 inches. For each survey plane data were obtained at approximately 2 in. vertical intervals for 3 transverse locations; $Z = C_L$ and $\pm$ 6 inches. At the test section inlet (X = -12 inches) these spacings resulted in a 12 point matrix of measurements for each configuration. At survey planes further downstream the number of measurement locations was restricted by the decreasing height of the test section. For most of the streamwise locations turbulence measurements were obtained at 6 locations.

The multi-component (u', v', and w') turbulence intensity distributions for the various acceleration/grid combinations are presented in Figs. 22 through 25. Composite plots showing the total turbulence intensity distributions for wedges 1 and 2 are presented in Figs. 26 and 27 respectively. Prior to examining the results measured for the individual configurations, the following details common to Figs. 22 though 27 should be noted: (1) the u' (streamwise) turbulence levels plotted in these figures are the average of the u' values determined with the X probe oriented in the vertical and horizontal directions; and (2) for all three components (u', v', and w') of turbulence the levels plotted are the average of all values measured at that data plane. For cases when all the turbulence levels over the data plane did not fall within the plotting symbol uncertainty bars indicate the range of the measured results.

The multi-component turbulence intensity distributions are presented in Figs. 22 through 25 for the four acceleration/grid combinations. For all four combinations the relationship between the magnitudes of the three components in the test section was $v' > w' > u'$ with the difference between the various components decreasing slightly with increasing X.

The anisotropy of the turbulence at the tunnel test section entrance results from combined effects of flow through coarse grids and the influence on the grid turbulence of the main tunnel contraction. As shown by Comte-Bellot and Corrsin (Ref. 17), lattice-type turbulence generating grids such as those used for the present study produce turbulence with $v' = w'$ and $u' \approx 5/4$ of the other components. For the present test facility (see Fig. 1) the main tunnel nozzle is located just downstream of the turbulence generating grids. Prandtl (Ref. 18) has provided a well known semiquantitative theory for predicting the influence of a contraction on the various components of turbulence. Prandtl's theory has been verified as being at least qualitatively correct by a large number of experiments (e.g., Uberoi, Ref. 19). Applying Prandtl's arguments to the present contraction shape, it would be expected that in passing through the nozzle u' would decrease ($\approx$ 1/contraction ratio) and v' and w' would increase (less than the decrease in u'). Because the contraction is two-dimensional (no contraction in the w' direction), the increase of the w' component should be less than the increase of the v' component. The measured turbulence intensity levels for the various components are arranged as expected ($v' > w' > u'$). The streamwise component (u') which should have had a slightly greater intensity than the other components at the grid location was significantly reduced as the flow passed through the contraction. The vertical and transverse (v' and w') components should have been approximately equal at the grid location and as the flow passed through the contraction the v' component was increased and the w' component was slightly increased.

It might be anticipated that the accelerations along the test section would also effect the relative strengths of the turbulence components. A comparison of the present multi-component turbulence distributions and the results measured for zero pressure gradient flow (Ref. 1) indicate that the test section acceleration had an effect on the component distribution for only one of the test cases. The anisotropy indicated by Figs. 22 through 24 (Grids 1 and 2) was approximately the same as measured for these grids in zero pressure gradient flow (Ref. 1). For Grid 3, however, there was a slight increase in anisotropy measured for the accelerating flow case (Fig. 25) relative to the zero pressure gradient flow (Ref. 1 - Fig. 31). Tan-atichat et al. (Ref. 16) clearly demonstrated that the influence of a given contraction on incoming turbulence is an extremely complex function of intensities, anisotropy and length scales. In particular, Ref. 16 demonstrated that the larger the scale of the incoming turbulence the greater the influence on turbulence anisotropy of a given contraction. In light of the results of Ref. 16 it is not surprising that the largest effect of the test section acceleration on the anisotropy resulted for the turbulence of largest scale (Grid 3).

For all locations with Grids Nos. 1 and 2 and for the far downstream locations for Grid Nos. 3 the turbulence data over the various survey planes were extremely uniform with all data falling within the plotting symbols. The largest non-uniformities in measured turbulence resulted for $X \leq 20$ for Grid No. 3. This region is within 10 grid mesh spacings (M) from the grid location. This result is in agreement with Ref. 3 which indicates that a distance of approximately 5 to 10 mesh lengths downstream of a grid are required to establish uniform flow. It should be noted here that the specific reason for locating the turbulence grids at the contraction entrance instead of at the test section entrance was to minimize turbulence nonuniformities in the test section. If the turbulence grid station had been located at the test section entrance, most of the test section would have fallen within the 5 to 10 mesh length flow establishment region and the test section turbulence would have been much less uniform.

Total turbulence distributions for the various acceleration/grid combinations were calculated from the multi-component turbulence data and are presented in Figs. 26 and 27. The nonunformity of the turbulence very near Grid No. 3 is again evident.

In summary, the conclusions reached from the free-stream turbulence intensity distribution measurements are:

(1) The relationship between the three components of the free-stream turbulence measured in the test section for all four acceleration/grid combinations was $v' > w' > u'$. This anisotropy resulted from the turbulence generating grids, the specific shape of the main tunnel contraction nozzle, and the accelerations along the test section. The measured anisotropy is in qualitative agreement with both the theory of Ref. 18 and the measured results of Ref. 16.

(2) The turbulence intensity measurements were very uniform over all transverse survey planes for Grid Nos. 1 and 2 and for the downstream survey planes for Grid No. 3. At the near-grid survey planes (less than 10 grid mesh lengths) for Grid No. 3 some slight nonuniformities were detected.

3.3 Test Section Turbulence Length Scale Distributions

Measurements of the longitudinal integral scale of the test section turbulence were obtained using single sensor hot film probes and the previously described anemometer system. Integral scale measurements were obtained for the four acceleration/grid combinations over the same survey plane locations as described in the previous section (Turbulence Intensity Distributions).

Streamwise integral scales were determined from autocorrelations of the single sensor signals as described in detail in Ref. 1. Accurate measurement of the length scale was possible for all measurement stations for the $K = 0.75 \times 10^{-6}$/Grid No. 3 case as the autocorrelation fell to zero beyond a reasonable time delay. For the

far downstream stations of the test cases with Grids No. 1 and 2, however, the autocorrelation data were contaminated by very low frequency fluctuations. These low frequency fluctuations prevented the autocorrelations from falling to zero for even very large time delays and made interpretation of the data uncertain. Similar low frequency signal contamination was encountered in the studies of Refs. 20 and 21. The low frequency contributions to the fluctuating signals are almost certainly not associated with the grid generated turbulence but with some other tunnel circuit unsteadiness. For this reason only those data for which reliable measurements could be made are presented. The reason that all the data for the Grid No. 3 case could be accurately interpreted was that the grid generated turbulence level was so high for this case (see Fig. 27) that the low frequency unsteadiness was insignificant. Spectral analysis of the signals obtained at the far downstream stations for Grids No. 1 and 2 indicate that nearly all the low frequency contribution to the fluctuating signal was for frequencies less than 5 Hz.

The length scale measurements for the various acceleration/grid combinations are presented in Fig. 28. As described above, data are presented only for those stations where accurate interpretations of the autocorrelations could be made. Also included are dashed fairings of measurements obtained at stations with high uncertainty. The length scale data of Fig. 28 are presented as ratios to the length scales measured for that configuration at the test section entrance (X = -12 in.). An examination of Fig. 28 reveals that the growth rate of the length scales is a function of both the acceleration and inlet turbulence characteristics. The strongest effect on length scale growth was recorded for the $K = 0.20 \times 10^{-6}$/Grid 1 configuration while the smallest growth rate effect results for the $K = 0.75 \times 10^{-6}$/Grid 3 case. Although no qualitative relationship is presently known for prediction of the effects of acceleration on length scale growth the present results can be compared with measurements obtained in Ref. 16. Tan-atichat et al. (Ref. 16) demonstrated similar dependence of length scale growth rate effects in a given acceleration on the characteristics of the inlet turbulence.

3.4 Test Section Power Spectral Density Distributions

Spectral distribution data were obtained along the tunnel centerline at tunnel mid-height for the same streamwise locations described in Section 3.2 (Turbulence Intensity Distributions). These data were obtained using a single sensor hot-film probe and the previously described anemometer/spectrum analyzer system. Figures 29 through 32 present these measured spectral distribution data for the four acceleration/grid combinations. For all four test configurations the measured data are in very good agreement with the von Karman one-dimensional spectrum (Ref. 22). This result indicates that the test section turbulence has the classic characteristics of grid generated turbulence and that the spectral distributions are not altered by the flow acceleration. Note that no power spectra are presented for the far downstream stations of Figs. 29, 30, and 31. As previously discussed, measurements of the integral length scale which appears in both the abcissa and ordinate of the PSD plots was considered unreliable at these stations.

4. Transition Location for Zero Pressure Gradient Flow

Under the first phase of this contract (Ref. 1) heat transfer distribution data were obtained for flows along the same flat test wall as used in the present study, but with constant free-stream velocity and a series of free-stream turbulence levels. For these earlier tests the boundary layer flow along the flat plate began laminar, passed through natural transition and continued developing in the fully turbulent state. These earlier tests were designed to determine the effects of the free-stream turbulence on fully turbulent boundary layer heat transfer and profile development. Since the test boundary layers of Ref. 1 passed through natural transition the heat transfer distributions (Ref. 1 - Figs. 41, 45, and 49) can be utilized to infer the effect of the free-stream turbulence on the location and length of transition. In Fig. 33 the transition locations determined from these heat transfer distributions are compared to the results of 8 other experiments and the prediction of the McDonald-Fish (Ref. 31) transition model. As can be seen from an examination of Fig. 33, the results from the present facility for T = 1.2 and 2.5 percent are in excellent agreement with the other data and the prediction. For T = 0.25 percent, however, the results from the present facility indicate earlier transition than either the other data or the McDonald-Fish prediction. As discussed in Section 4.2.1 of Ref. 1, for the T = 0.25 percent test case the transition process was dominated by the tunnel sidewall and corner flows. The off-centerline wall thermocouples indicated that transition began at both sides of the test wall and progressively encroached on the tunnel centerline flow. Figure 33 indicates that for the two cases with higher freestream turbulence (where the transition process was approximately two-dimensional) the data from the present facility are in excellent agreement with those from other sources.

Figure 34 presents a comparison of the transition length as indicated by (1) the measured heat transfer distributions, (2) data from 12 other sources, and (3) the prediction of the McDonald-Fish procedure. Although there is considerable scatter in the other data it is clear that the present results indicate transition lengths much larger than the mean of the other results. This point will be discussed further in a later section.

5. Heat Transfer and Boundary Layer Profile Measurements

5.1 Heat Transfer Distributions, $K = 0.20 \times 10^{-6}$

Heat transfer distributions measured for wedge 1 with no grid and 4 turbulence grids installed are presented in Fig. 35. To demonstrate the fact that the measurements obtained for Grids No. 1 and 2 are part of a consistent trend additional heat transfer distribution data obtained with no turbulence grid and with turbulence Grids No. 3 and 4 are included in Fig. 35. Free-stream turbulence distribution data were not obtained for the no-grid or the Grid Nos. 3 or 4 cases with wedge 1 (but it is certainly reasonable to expect that the turbulence intensity increased progressively with increasing grid coarseness). See, for example, Ref. 1 - Fig. 33. Also shown in Fig. 35 are the velocity and acceleration parameter distributions for this accelerating configuration.

The heat transfer distributions presented in Fig. 35 demonstrate the progressive upstream movement of the transition process with increasing freestream turbulence. For no turbulence grid (T ~ 1/4 percent) the test boundary layer apparently remained laminar for the entire length of the test section. With increasing turbulence the transition process moved progressively upstream until, for Grid No. 4, transition began about 3 inches from the plate leading edge. The data of Fig. 35 also indicate that for the fully turbulent regions of the various flows the freestream turbulence level increases the heat transfer (Ref. 1).

5.2 Profile Data - Flow Condition 1, $K = 0.20 \times 10^{-6}$/Grid No. 1

Integral quantities computed from the mean velocity and temperature boundary layer profile data for $K = 0.20 \times 10^{-6}$ and Grid No. 1 are presented in Figs. 36 and 37. The thermal energy balance data for Fig. 36a is a measure of both the accuracy of these boundary layer profile data and is the two-dimensionality of the test flow. The thermal energy balance is a ratio of the total convective heat generated per unit tunnel width upstream of any profile location to the measured thermal energy contained in the boundary layer at the location. An examination of Fig. 36a reveals that the thermal energy balance is within approximately 10 percent of unity for most of the measured profiles. The largest deviations from unity in the thermal energy balance were measured between X = 30 and 42 inches where the boundary layer is passing through transition. These relatively large errors in the transitional boundary layer measurements are probably a result of the intermittent character of transitional flows. Some errors in the measured velocity profiles could be expected from imperfect time averaging of the pitot probe system for the intermittant velocity bursts. In general, however, Fig. 36a indicates a high degree of accuracy, consistency and two-dimensionality for the measured profiles.

The measured momentum and displacement thicknesses for the various boundary layer profiles of the test condition are presented in Fig. 36b. As can be seen from an examination of this figure, profiles measured at various transverse but fixed streamwise locations on the test surface are in good agreement.

The distribution of the boundary layer shape factor along the test wall is presented in Fig. 37. Also included in Fig. 37 are shape factor distributions for fully laminar and fully turbulent flow as predicted by the numerical boundary layer code of Refs. 33 and 34. These predicated distributions are for the test velocity distribution and test wall heat flux. An examination of Fig. 37 reveals that the measured shape factors for $X \lesssim 25$ and $X \gtrsim 48$ inches agree reasonably well with the predicted laminar and turbulent values respectively. The transition of the boundary layer from laminar to turbulent flow is clearly indicated through the rapid drop in shape factor between approximately X = 25 and 48 inches.

5.3 Profile Data - Flow Condition 2, $K = 0.20 \times 10^{-6}$/Grid 2

Integral boundary layer quantities for the profiles of flow condition 2 are presented in Figs. 38 and 29. As for Flow Condition 1, the thermal energy balance

data of Fig. 38a fall within approximately 10 percent of unity. Again somewhat larger deviations were measured within the region of boundary layer transition. The plots of momentum and displacement thickness distributions (Fig. 38b) reveal that spanwise variations of the profiles were very slight.

Figure 39 indicates that with Grid 2 installed the boundary layer transition process extended from approximatley X = 4 to 21 inches. The measured shape factors downstream of transition are in excellent agreement with the prediction of Ref. 43.

5.4 Heat Transfer Distribution, $K = 0.75 \times 10^{-6}$

Heat transfer distributions for wedge 2 with Grids Nos. 2 and 3 installed are presented in Fig. 40. As with Fig. 35, additional (Grids Nos. 1, 4, and no grid) heat transfer distribution data are presented in Fig. 40 to demonstrate the fact that the data obtained with Grids Nos. 2 and 3 installed are part of a consistent trend. No free-stream turbulence distribution data were obtained for the no-grid or the Grid Nos. 1 or 4 cases with wedge 2 but it is expected that the turbulence intensity increased progressively with increasing grid coarseness. See, for example, Ref. 1 - Fig. 33. Also shown in Fig. 40 are the velocity and acceleration parameter distributions for this configuration.

As with the results for wedge 1 the heat transfer distributuions of Fig. 40 demonstrate the progressive upstream movement of the transition process with increasing freestream turbulence. There were, however, significant differences between the heat transfer distributions measured for wedges 1 and 2. For the higher acceleration level (wedge 2) transition was suppressed for the entire test flow for both the no-grid and Grid No. 1 test cases. In addition, for Grid No. 2 installed the length of the transition region is much greater for the more highly accelerated test case.

5.5 Profile Data - Flow Condition 3, $K = 0.75 \times 10^{-6}$/Grid No. 2

Integral boundary layer quantities for the profiles of flow condition 3 are presented in Figs. 41 and 42. The thermal energy balance data of Fig. 41a fall within approximately 5 percent of unity indicating high degrees of accuracy and flow two-dimensionality. The momentum and displacement thickness distributions for this test case (Fig. 41b) indicate only small transverse variations of the measured profiles. Because of the very strong acceleration for this case, both the momentum and displacement thicknesses decrease for approximately the downstream 30 percent of the test length.

Figure 42 indicates that with Grid No. 2 installed the transition process is spread out over a significant fraction of the test section length. While agreement between measurement and prediction was less satisfactory upstream of transition the masured shape factors closely approach the predicted turbulent values for $X \gtrsim 45$ inches.

5.6 Profile Data - Flow Condition 4, $K = 0.75 \times 10^{-6}$/Grid No. 3

Integral boundary layer quantities measured for flow condition 4 are presented in Figs. 43 and 44. As with flow condition 3 the thermal energy balance data of Fig. 43a fall within approximately 5 percent of unity. Again this result indicates high degrees of accuracy and flow two-dimensionality. For flow condition 4 the maximum values of momentum and displacement thicknesses were reached approximately half way along the test section. Downstream of approximately X = 30 inches the strong flow acceleration for this case resulted in progressively decreasing integral thicknesses.

Figure 44 indicates that for this case the transition process was completed at approximately X = 17 inches. The measured shape factors agreed with the predicted laminar and turbulent values upstream and downstream of transition respectively.

5.7 Outline of Profile Data Report

A report (Ref. 32) has been prepared in which the boundary layer profile data of this study are both tabulated and plotted. For all turbulent profiles the boundary layer integral quantities as well as the following values are tabulated in Ref. 32:

$$y,\ \frac{y}{\delta},\ U,\ T,\ \frac{U}{U_e},\ \frac{T_w - T}{T_w - T_e},\ \frac{U - U_e}{U_\tau},\ U^+,\ Y^+,\ T^+$$

For all turbulent profiles the following plots are presented in Ref. 32:

i) $\frac{U}{U_e}$ vs $\frac{y}{\delta}$

ii) $\frac{T_w - T}{T_w - T_e}$ vs $\frac{y}{\delta}$

iii) U^+ vs Y^+

iv) T^+ vs Y^+

v) $\frac{U - U_e}{U_\tau}$ $\frac{Y}{\delta}$

For those profile stations where the boundary layer was either laminar or transitional the turbulent "law-of-the-wall" analysis is inapplicable. For those profiles the data are plotted as velocity and temperature ratios only. Tabulated values are given for the measured velocities, temperatures, velocity and temperature ratios, and for the calculated integral values of the boundary layer profiles.

ANALYSIS AND DISCUSSION OF RESULTS

The combined effects of freestream turbulence and steamwise acceleration on boundary layer transition have been experimentally studied for four turbulence intensity/acceleration combinations. The position, extent and character of the transitional flows for these cases were determined using both mean profile and wall heat transfer distribution measurements. In the present section comparisons are made between these different indications of the onset and length of transition. In addition, the velocity and temperature boundary layer profile data for one of the test cases are examined in detail. Finally the transition location data for this study are compared to similar transition data from other experimental studies.

1. Development of the Mean Velocity and Temperature Profiles Through Transition

Mean velocity and temperature boundary layer profile data were obtained for each of the four acceleration/turbulence intensity combinations examined in this study. Distributions of the measured boundary layer integral thicknesses and shape factors for the four test cases were presented in the previous section.

As an example of the information available for these four test cases, the individual velocity and temperature profile data for Flow Condition 2 ($K = 0.20 \times 10^{-6}$/grid 2) are presented in Figs. 45 through 47. In Fig. 45a and b the developing mean velocity and temperature profiles are presented in the form of velocity and temperature ratio versus $Y/\delta_{0.995}$. The growth of the velocity boundary layer thickness ($\delta_{0.995}$) along the test wall is given in Fig. 45c. Both the velocity and temperature profiles demonstrate the progressive change from laminar-like distributions to the "full" profiles associated with turbulent flow.

Figure 46 presents the velocity profile data of Fig. 45a in the universal turbulent coordinates U^+ vs Y^+. For the most upstream profile ($x = 4.4$ inches) U_τ was determined from the slope of the mean velocity profile at the wall and the molecular viscosity. For the downstream profiles ($x = 24.4$, 36.4 and 68.4 inches) U_τ was determined from fits of the profile data to the law of the wall. For the intermediate profiles U_τ was calculated using the two-dimensional von Karman momentum integral equation and the measured integrals of the mean velocity profiles. As can be seen from an examination of Fig. 46 there is an orderly change from laminar to fully turbulent boundary layer flow with increasing distance along the wall. At $x = 4.4$ inches the boundary layer is fully laminar with $U^+ = Y^+$ for $Y^+ \lesssim 20$. With the development of effective turbulent shear within the boundary layer the profiles become progressively more full with increasing x. For the most downstream profile ($x = 68.4$) the profile data fit the buffer region and logarithmic-wall laws for $Y^+ \lesssim 400$. The outer region of this most downstream profile shows a weak wake appropriate for this low Reynolds number ($Re_\theta = 2470$) and steamwise pressure gradient.

The mean temperature data of Fig. 45b are presented in the universal turbulent coordinates T^+ vs Y^+ in Fig. 47. Friction velocities for these profiles were the same as used for the corresponding velocity profiles of Fig. 46. At the most upstream location (x = 4.4 inches) the mean temperature profile is seen to be laminar-like and developing within the laminar velocity profile. Figure 46 shows that at x = 4.4 inches the laminar velocity profile extends to $Y^+ \sim 70$. In Fig. 47 the temperature profile at this same station extends to only $Y^+ \cong 40$. This difference between the velocity and temperature profiles at x = 4.4 inches results from the fact that there is a short but finite unheated length (ξ = 1.69 inches) on the leading edge of the heated test wall (see Description of Equipment). At x = 4.4 inches the thermal and momentum boundary layers have not yet reached equilibrium. See Ref. 35 for similar measurements of a temperature profile developing within a velocity profile. For the profiles measured from x = 8.4 through 24.4 inches the mean temperature profiles fall between the fully laminar and fully turbulent limits. Note that the development of the temperature profiles seem to lag that of the respective velocity profiles. This lag is clearly in evidence for x = 20.4 and 24.4 inches where the velocity profiles are in close agreement with the law of the wall while the temperature profiles exhibit no logarithmic region. At the furthest downstream location (x = 68.4 inches) the mean temperature profile agrees well with the buffer zone and logarithmic laws for $Y^+ \lesssim 200$. In contrast to the mean velocity profile at this station, the outer region of the most downstream temperature profile shows a strong wake component. This difference between the velocity and temperature profiles is produced by the streamwise pressure distribution. The boundary layer velocity distribution is directly dependent on the mainstream acceleration through the equations of motion. The temperature distribution, however, is only indirectly linked to the flow acceleration through the effect of the acceleration on the turbulent heat transport. For these reasons the most downstream temperature boundary layer is considerably thicker and less "full" than its velocity counterpart.

2. Measurements of Transition Length

The position and length of transitional boundary layer flow for the four test configurations were determined both through mean profile and wall heat transfer distribution measurements. As can be seen from an examination of Fig. 37, 39, 42 and 44, the scatter in the measurements of shape factor was most extreme for the upstream profiles. This scatter resulted from the fact that the upstream profiles were extremely thin and therefore difficult to accurately document. Bearing in mind the uncertainties in the laminar region measurements, comparisons of the locations of the beginning of transition as indicated by the shape factor (Figs. 37, 39, 42 and 44) and heat transfer data (Figs. 35 and 40) show good agreement.

For both test cases in which the turbulence intensity was high relative the strength of the flow acceleration (flow conditions 2 and 4) the mean profile and wall heat transfer distribution measurements were in very close agreement and indicated nearly identical short regions of transitional flow. For both test cases

in which the flow acceleration was relatively strong in relation to the turbulence intensity (test configurations 1 and 3), however, there were significant differences in the transition length as indicated by the profile and heat transfer measurements. For both test configurations 1 and 3 the lengths of transitional flow as determined from the heat transfer distributions were at least 50% longer than as indicated by the shape factor distributions. This discrepancy is reminiscent of the transition length data shown earlier in Fig. 34. In Fig. 34 transition lengths as determined from heat transfer distributions on the present heated wall for zero pressure gradient flow were compared with other zero pressure gradient transition length data. These other data were determined from hot wire and velocity profile data and in general indicated considerably reduced transition lengths in comparison to the present heat transfer data. These limited results indicate that for cases with extended transitional flow lengths the mean velocity profile may reach a shape typical of a fully turbulent condition in a shorter length than is required for the boundary layer turbulence to assume its equilibrium structure. The wall heat transfer, which is dominated by the turbulent transport through the boundary layer, does not reach fully turbulent values until well downstream of the establishment of the fully turbulent mean velocity profile.

3. Combined Influence of Turbulence and Acceleration on Transition Location

The transition location data of the present program are compared to the results of other investigators in Fig. 48. In this figure the momentum thickness Reynolds number of the boundary layer at the location of the beginning of transition is plotted as a function of the local Pohlhausen laminar acceleration parameter $\Lambda_\theta = \theta^2/\nu \ \delta U/\delta x$. The local turbulence intensity at the transition location is indicated beside each data point. Data for the present study are given for both zero pressure gradient and accelerating flow cases. Also shown in Fig. 48 are accelerating flow-flat wall data from Ref. 36 and the correlation curves (for airfoils) of Ref. 37. The data of Ref. 36 were obtained at a turbulence intensity of approximately 2.5% and for that level show excellent agreement with the results from the present study. Dashed fairings have been included in Fig. 48 to suggest possible transition location correlations for flat wall flows. Suggested correlations are given for T = 2.5, 2.2, and 1.2% turbulence. Note that these are for accelerating flows so the negative slopes for T = 2.2 and 2.5% turbulence do not imply an upstream movement of transition with increased acceleration. The correlation curves of Seyb (Ref. 37) suggest that transition was considerably delayed for airfoil suction surface flows in relation to the flat wall cases. This difference may very well be a result of the stabilizing effect of the convex streamline curvature for the airfoil suction surfaces.

ASSESSMENT OF THE UTRC TRANSITIONAL BOUNDARY LAYER CODE

Calculations were performed with the boundary layer code developed by McDonald et al. (Refs. 31 and 38) for the test configuration described above. Previous assessment of this code for zero pressure gradient fully developed turbulent flow has been presented in Ref. 1. For application to the current configurations, the principal input conditions were the wall temperature and the freestream turbulence distributions both of which were determined experimentally. For the wall temperature distribution, an unheated leading edge region 1.69 inches long was assumed at an adiabatic free-stream recovery temperature (see Description of Test Equipment for details of the test plate configuration) with the remaining regions represented by a least squares cubic spline fit to the experimental data shown in Figures 35 and 40. Also, as shown in Figures 26 and 27, the turbulence level data of Table 1 were represented by simple cubic spline curve fits. Calculations were performed with 200 grid points across the boundary layer and a variable longitudinal grid spacing to accurately represent the regions of rapid variations.

The most direct comparison available for the kinematic predictions of the transition region are the shape factor comparisons shown in Figure 49. In an overall sense it is seen that the turbulence model of McDonald and Kreskovsky (Ref. 38) clearly gives a good representation of both the turbulence level and pressure gradient effects on the shape factor variation during the transition regions. Assessment of these results shows that there is a tendency, most clearly seen in Fig. 11b, to predict transition too early for the low turbulence cases and too late for the higher turbulence levels. Also, as seen in Figure 11b, an anamolous rise in shape factor was encountered aft of the transition process for the high acceleration case. Nonetheless the overall transition region predictions of Fig. 11 provide a strong endorsement of the McDonald and Kreskovsky (Ref. 38) model.

Comparison of the current predictions with experimentally measured skin friction aft of transition are shown in Figure 50. For the low acceleration case, Fig. 50a shows that the model provides excellent comparison with the data for the high turbulence level (grid 2) and slightly underpredicts the low turbulence case (grid 1). This latter result is consistent with the shape factor plot of Figure 49a where it was seen that transition was predicted to occur around 6 inches ahead of the location observed experimentally. For the high acceleration case, the predictions model are seen in Fig. 50b to encounter difficulties aft of transition. Here the data shows typical monotonic decay while the theoretical results encounter an unexplained drop off as the flow continues to accelerate (see Fig. 10).

The final comparisons made were with the heat transfer data of Figs. 35 and 40. Figure 51 gives a direct comparison of the measured heating levels with those predicted with the model of McDonald and Kreskovsky (Ref. 38). The abrupt change in the predicted distribution at $x = 1.69$ inches follows directly from the step change in the surface temperature distribution that accompanies the change from an adiabatic to fixed heat flux state at this point. It is seen that the predictions in the laminar regions aft of this leading edge effect are quite good down to where transition effects become apparent. Thereafter it is seen that while the predictions show correct qualitative trends, serious quantitative differences are encountered. Apparently

the same errors observed in the shape factor and skin friction comparisons of Figs. 49 and 50 are encountered here but in a rather amplified form. One possible explanation of this behavior stems from the rather low heat transfer levels encountered in this test series. The current version of the prediction code cannot be run with a specified heat flux boundary condition, but rather employs the measured wall temperature levels as a surface condition. For the low overheat levels of the current experiments, it is known that the model is very sensitive to wall temperature levels due to simple numerical truncation errors. There is reason to believe that solutions obtained with a heat flux boundary conditions would provide a more accurate representation of flow field.

CONCLUSIONS

1. A detailed set of boundary layer profile, heat transfer distribution and freestream turbulence data have been generated for four accelerating transitional boundary layer flows. These data have been shown to be accurate, consistent, and highly two-dimensional. It is anticipated that these results will provide a needed set of fundamental, well documented experimental test cases to which analytical predictions can be compared.

2. Comparisons of transitional velocity profile shape factor and wall heat transfer distribution data indicate that fully turbulent mean velocity profiles are achieved upstream of fully turbulent wall heat transfer rates. The present data suggest that the mean velocity profile is established in a shorter length than is required for the development of the equilibrium turbulence distribution.

3. Transition location data obtained in the present program agree very well with data from other flat wall studies for both zero pressure gradient and accelerating flows. Suggested correlation curves are given for predicting flat wall transition locations with the combined effects of freestream turbulence and streamwise acceleration.

4. The UTRC code assessment tasks indicated that the transition/turbulence model of McDonald and Kreskovsky gives good quantitative prediction of the combined influences of pressure gradient and freestream turbulence on the shape factor of transitional boundary layer. Heat transfer predictions were found to be less satisfactory. This latter weakness may stem from current code limitations that require use of a wall temperature boundary condition on the energy equation.

LIST OF SYMBOLS

C_f - skin friction coefficient, $\frac{2\tau_w}{\rho U_e^2}$

c_p - specific heat at constant pressure

I - strip current

k - thermal conductivity

Pr - molecular Prandtl number

Pr_t - turbulent Prandtl number, $\frac{\epsilon_m}{\epsilon_h}$

q - heat flux

R_{foil} - unit resistance of heater foil

Re_x - Reynolds number based on distance from leading edge

Re_θ - Reynolds number based on boundary layer momentum thickness

St - Stanton number, $\frac{h}{\rho U c_p}$

t - temperature

t^+ - dimensionless temperature, $\frac{t_w - t}{q_w} \rho_w c_p \sqrt{\tau_w/\rho}$

U - velocity

U^+ - dimensionless velocity, $\frac{U}{U_\tau}$

U_τ - friction velocity

x - distance from leading edge

y - distance from wall

Y^+ - dimensionless distance from wall, $\frac{y U_\tau}{\nu}$

α - temperature coefficient of resistance

δ - boundary layer thickness

LIST OF SYMBOLS (Cont'd)

δ^* - displacement thickness, $\int_0^\delta \left(1 - \frac{\rho U}{\rho_e U_e}\right) dy$

δ^{**} - energy dissipation thickness, $\int_0^\delta \frac{\rho U}{\rho_e U_e}\left(1 - \frac{U^2}{U_e^2}\right) dy$

δ_H - enthalpy thickness, $\int_0^{\delta_1} \frac{\rho U}{\rho_e U_e}\left(\frac{T-T_e}{T_e}\right) dy$

ε - surface emissivity

θ - momentum thickness, $\int_0^\delta \frac{\rho U}{\rho_e U_e}\left(1 - \frac{U}{U_e}\right) dy$

κ - von Karman constant

μ - molecular viscosity

ν - kinematic viscosity

ξ - unheated starting length

ρ - fluid density

T - shearing stress

Subscripts

e - freestream

w - wall

REFERENCES

1. Blair, M. F. and M. J. Werle: The Influence of Freestream Turbulence on the Zero Pressure Gradient Fully Turbulent Boundary Layer. UTRC Report R80-914 388-12, Sept. 1980.

2. Blair, M. F., D. A. Bailey and R. H. Schlinker: Development of a Large Scale Wind Tunnel for the Simulation of Turbomachinery Airfoil Boundary Layer. ASME paper 81-GT-6 to be presented at ASME Gas Turbine Conference, Mar. 1981.

3. Baines, W. D. and E. G. Peterson: An Investigation of Flow Through Screens. Trans. of ASME, Vol. 73, p. 467-480, Jul. 1951.

4. Caspar, J. R., D. E. Hobbs and R. L. Davis: Calculation of Two-Dimensional Potential Cascade Flow Using Finite Area Methods. AIAA Journal, Vol. 18, No. 1, Jan. 1980.

5. Blackwell, B. F. and R. J. Moffat: Design and Conduction of a Low Velocity Boundary-Layer Temperature Probe, AIAA paper No. 74-709, ASME paper No. 74-HT-29, Jul. 1974.

6. MacMillan, F. A.: Viscous Effects in Flattened Pitot Tubes at Low Speeds, Journal of Royal Aeronautical Society, Vol. 58, 1954.

7. Quarmby, A. and H. K. Das: Displacement Effects on Pitot Tubes With Rectangular Mouths, The Aeronautical Quarterly, May 1969.

8. MacMillan, F. A.: Experiments in Pitot Tubes in Shear Flow, A.R.C. R & M 3028, 1957.

9. Coles, D. E.: The Turbulent Boundary Layer in a Compressible Fluid, Rand Report R-403-PR, 1962.

10. Coles, D.: Proceedings, Computations of Turbulent Boundary Layers - 1968, AFOSR-IFP, Stanford Conference, Vol. II, 1968.

11. Burton, R. A.: A Simple Universal Velocity Profile Equation, AIAA Journal 3, 1965.

12. Kays, W. M.: Convective Heat and Mass Transfer. McGraw-Hill Book Company, N. Y., p. 222 and 244, 1966.

13. Schlicting, H.: Boundary Layer Theory, 6th Edition, McGraw-Hill Book Company, N. Y., p. 125-133 and 544-556, 1968.

REFERENCES (CONT'D)

14. Levy, S.: Heat Transfer to Constant-Property Laminar Boundary-Layer Flows with Power-Function Freestream Velocity and Wall-Temperature Variation, Journal Aeronautical Sciences, Vol. 19, p. 341, 1952.

15. Sharma, O. P., R. A. Wells, R. H. Schlinker, D. A. Bailey: Boundary Layer Development in Turbine Airfoil Suction Surfaces, ASME paper No. 81-GT-204, to be presented at Gas Turbine Conference, Mar. 1981.

16. Tan-atichat, J., H. M. Nagib and R. E. Drubka: Effects of Axisymetric Contractions on Turbulence of Various Scales. NASA CR 165136, Sept. 1980.

17. Comte-Bellot, G and S. Corrsin: The Use of a Contraction to Improve Isotropy of Grid Generated Turbulence. Journal of Fluid Mech., Vol. 25, p. 657-682, 1966.

18. Prandtl, L.: Attaining a Steady Air Stream in Wind Tunnels. NASA TM 726, 1933.

19. Uberoi, M. S.: Effect of Wind-Tunnel Contraction on Freestream Turbulence. Journal of Aeronautical Sciences, Aug. 1956.

20. Meier, H. V. and H. P. Kreplin: Influence of Freestream Turbulence on Boundary Layer Development. AIAA Journal, Vol. 18, No. 1, Jan. 1980.

21. Ramjee, V. and A. K. M. F. Hussain: Influence of the Axisymetric Contraction Ratio on Freestream Turbulence. ASME Journal of Fluids Engineering, p. 506-515, Sept. 1976.

22. Hinze, J. O.: Turbulence. McGraw-Hill, N. Y., 1959.

23. Zysina-Molozhen and V. M. Kuznetsova: Investigation of Transition Conditions in a Boundary Layer. Teploenergetika, Vol. 16, No. 7, p. 16-20, 1969.

24. Sinclair, Wells, C.: Effects of Freestream Turbulence on Boundary Layer Transition. AIAA Journal, Vol. 5, No.1, p. 172-174, Jan. 1967.

25. Boltz, F. W., G. C. Kenyon and C. Q. Allen: The Boundary Layer Transition Characteristics of Two Bodies of Revolution, A Flat Plate, and an Unswept Wing in a Low Turbulence Wind Tunnel. NASA TN D-309, 1960.

REFERENCES (CONT'D)

26. Dryden, H. L.: Transition from Laminar to Turbulent Flow. Turbulent Flow and Heat Transfer. Princeton University Press, p. 3-74, 1959.

27. Schubauer, G. B. and H. K. Skramstad: Laminar Boundary Layer Oscillations and Transition on a Flat Plate. NASA Report 909, 1948.

28. Hall, A. and G. S. Hislop: Experiments on the Transition of the Laminar Boundary Layer on a Flat Plate. Aeronautical Research Committee of Great Britain, Reports and Memo, 1938, 1943.

29. Van der Hegge Zijen, B. G.: Measurements of the Velocity Distribution in the Boundary Layer Along a Plane Surface. Aeronautical Laboratory Technical H. S. Delft, Report No. 6, 1924.

30. Reynolds, W. C., W. M. Kays and S. J. Kline: Heat Transfer in the Turbulent Incompressible Boundary Layer, IV-Effect of Location and Transition and Prediction of Heat Transfer in a Known Transition Region. NASA Memorandum 12-4-58W, 1958.

31. McDonald, H. and R. W. Fish: Practical Calculations of Transitional Boundary Layers, Inter. Journal of Heat and Mass Transfer, Vol. 16, No. 9, p. 1729-1744, Sept. 1973.

32. Blair, M. F.: Final Data Report-Vol. II- Velocity and Temperature Profile Data for Accelerating, Transitional Boundary Layers, UTRC Report R81-914388-16, Jan. 1981.

33. Carter, J. E., D. E. Edwards, M. J. Werle: A New Coordinate Transformation for Turbulent Boundary Layer Flows - Numerical Grid Generation Techniques. NASA CP-2166, Oct. 6-7, 1980.

34. Edwards, D. E., J. E. Carter and M. J. Werle: Analysis of Boundary Layer Equation Including a New Adaptive Grid Technique, UTRC Report to be published early 1981.

35. Blom, J.: An Experimental Determination of the Turbulent Prandtl Number is a Developing Temperature Boundary Layer, Ph.D. Thesis, Technological University, Eindhoven, The Netherlands, 1970.

36. Edwards, A, B. N. Furber: The Influence of Freestream Turbulence on Heat Transfer by Convection from an Isolated Region of a Plane Surface in Parallel Air Flow. Proceedings of the Institution of Mechanical Engineers, Vol. 170, p. 941-953, 1956.

REFERENCES (CONT'D)

37. Seyb, N. J.: The Role of Boundary Layers in Axial Flow Turbomachines and the Prediction of Their Effects. Agardograph Conference Proceedings, 164, 241, 1972.

38. McDonald, H. and J. P. Kreskovsky: Effect of Freestream Turbulence on the Turbulent Boundary Layer, Intl. Journal of Heat and Mass Transfer, Vol. 17, 1974.

TURBULENCE INTENSITY DISTRIBUTIONS

Distance From Leading Edge x-inches	$K = 0.2 \times 10^{-6}$		$K = 0.75 \times 10^{-6}$	
	Grid 1	Grid 2	Grid 2	Grid 3
-12	.012	.026	.027	.066
4	.010	.020	.021	.049
16	.0092	.018	.017	.038
28			.014	.029
40	.0075	.014		
52			.080	.015
64	.0065	.011		

Table 1. Measured Total Turbulence Intensity Distribution for the Four Flow Conditions

Table II

Measured Wall Temperature Distributions

	Twall - Te (°R)			
	K = 0.2 x 10^{-6}		K = 0.75 x 10^{-6}	
X (inches)	Grid #1	Grid #2	Grid #2	Grid #3
2.19	10.80	10.50	12.76	13.10
2.69	14.85	14.44	17.34	17.37
3.19	17.01	16.53	19.84	19.47
3.69	19.61	19.04	22.58	21.74
4.19	21.08	20.55	24.29	23.14
4.69	22.71	22.13	26.05	24.33
5.19	24.07	23.29	27.50	25.30
5.69	25.80	24.67	28.96	25.99
6.19	26.67	25.39	30.20	26.63
6.69	27.95	26.49	31.21	26.92
7.19	28.76	27.06	32.22	26.26
8.19	29.82	27.67	33.22	26.46
9.19	31.87	28,12	35.09	26.56
10.19	32.83	27.55	35.92	25.54
11.19	34.29	28.29	37.17	24.99
13.19	36.86	27.19	39.32	24.42
15.19	38.21	24.25	40.00	23.01
17.19	40.09	21.56	41.16	22.77
19.19	41.32	19.98	41.87	22.38
21.19	42.10	18.13	41.00	21.38
23.19	43.88	17.77	41.00	21.39
25.19	45.24	17.80	40.00	21.11
27.19	44.97	17.21	38.66	20.30
29.19	44.94	17.57	36.82	20.36
31.19	44.65	17.65	35.32	20.19
33.19	43.33	17.63	32.90	19.70
35.19	41.30	17.77	31.36	19.40
37.19	40.21	18.01	28.93	19.23
39.19	36.53	17.29	26.23	18.07
41.19	34.28	17.80	24.47	18.07
43.19	30.21	17.80	23.70	17.56
46.19	28.39	17.68	21.29	16.67
49.19	25.19	17.91	19.70	16.12
52.19	23.09	17.52	17.54	14.96
55.19	21.21	17.47	16.35	14.05
58.19	19.94	17.28	14.73	12.94
61.19	18.89	17.25	13.66	11.87
64.19	18.34	17.19		
67.19	17.86	17.21		
70.19	17.48	16.81		

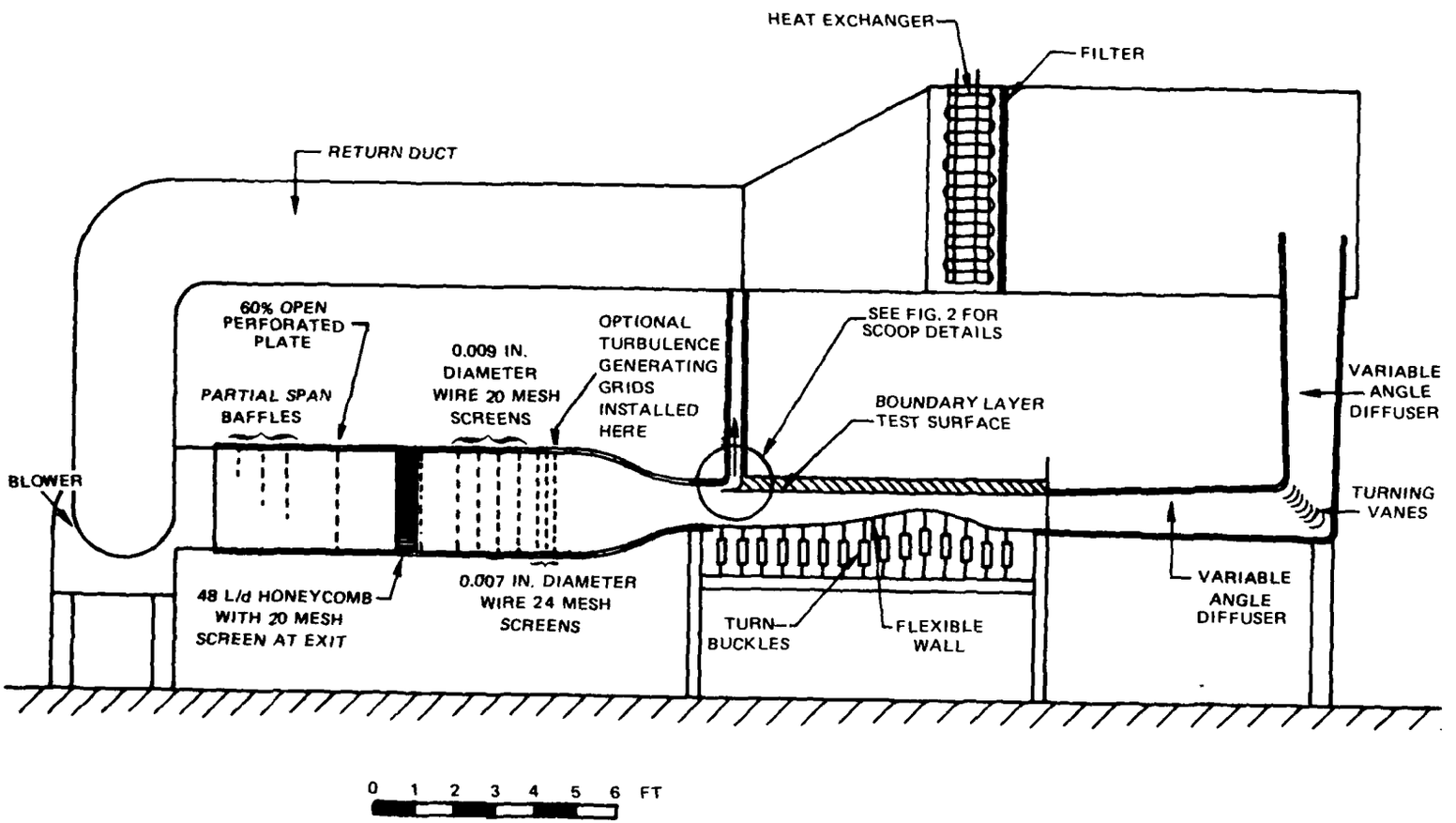

Figure 1. United Technolgies Research Center Boundary Layer Wind Tunnel

80-8-95-6

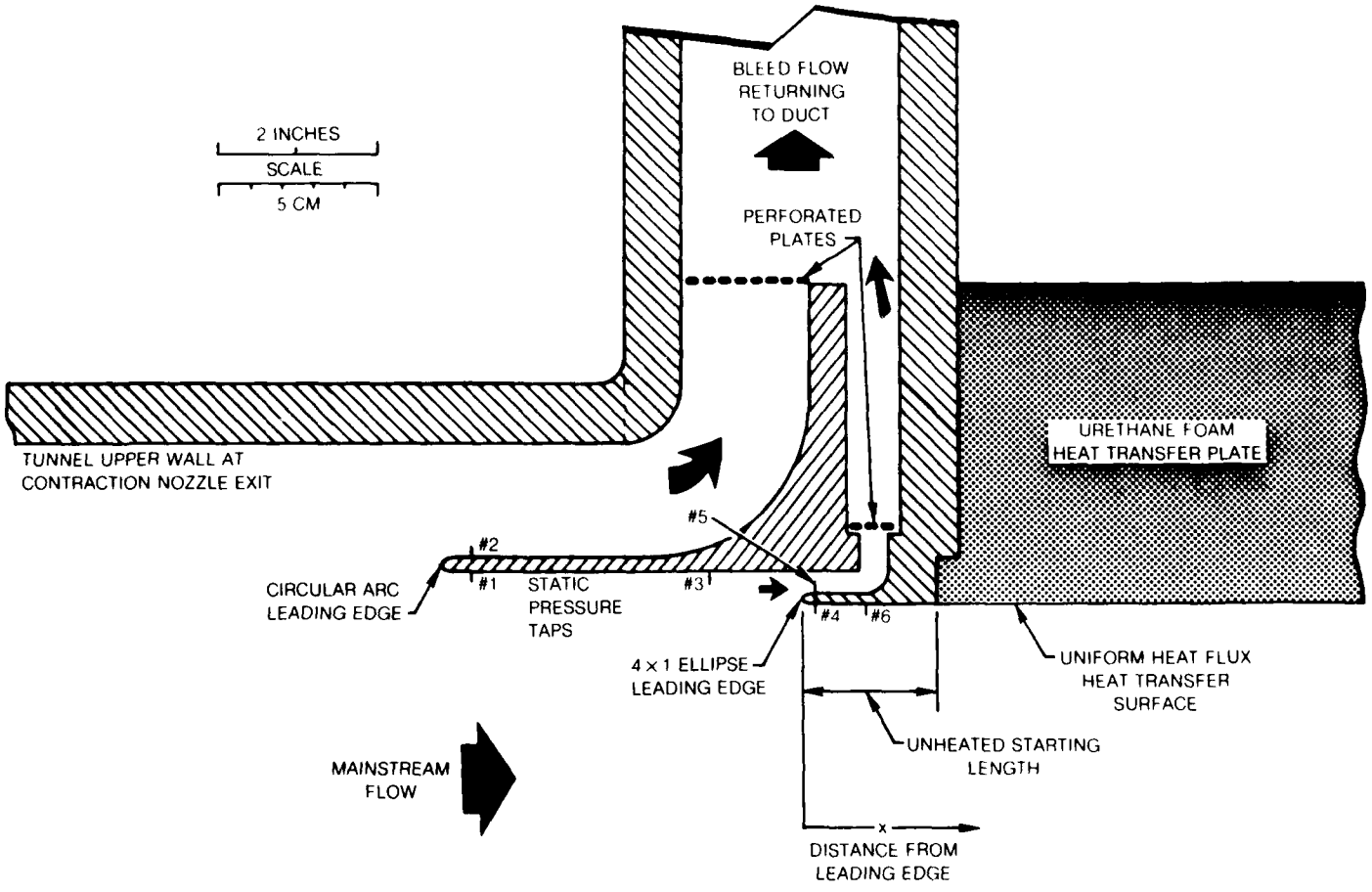

Figure 2: Detailed Sketch of Test Wall Leading Edge Bleed Scoop

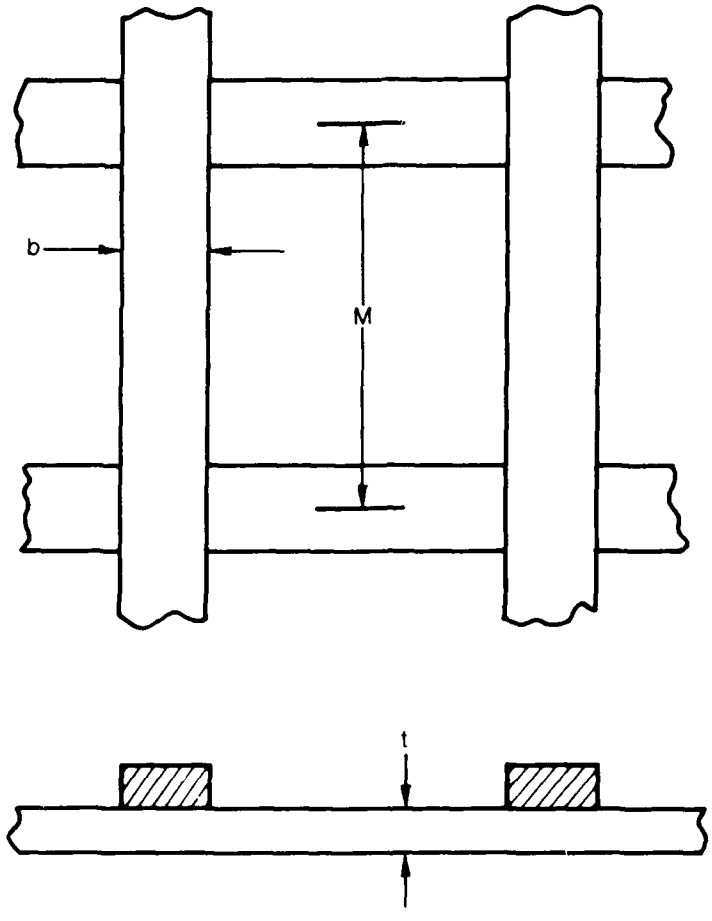

GRID NUMBER	b (inches)	M (inches)	t (inches)	M/b	% OPEN AREA
1	3/16	7/8	3/16	4 67	62
2	1/2	2 9/16	3/8	5 13	65
3	1 1/2	7	1/2	4 67	62
4	2	9	1/2	4.50	61

Figure 3. Turbulence Generating Grid Configurations for the Boundary Layer Wind Tunnel

79-11-93-13

GRID NUMBER 1

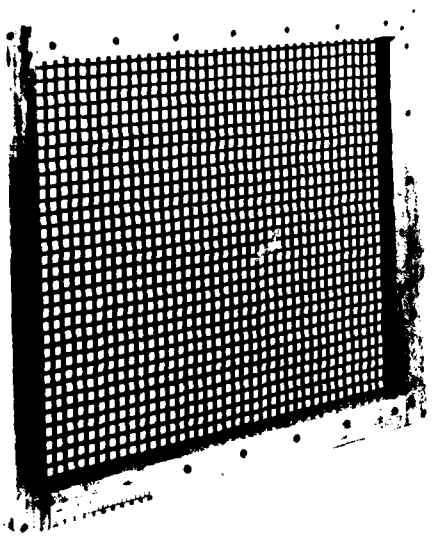

GRID NUMBER 2

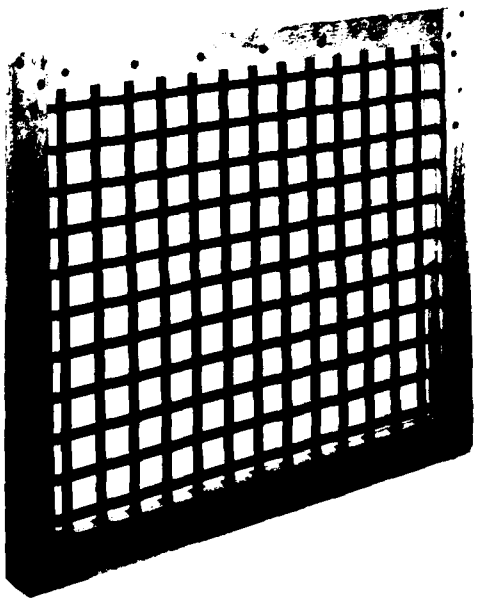

GRID NUMBER 3

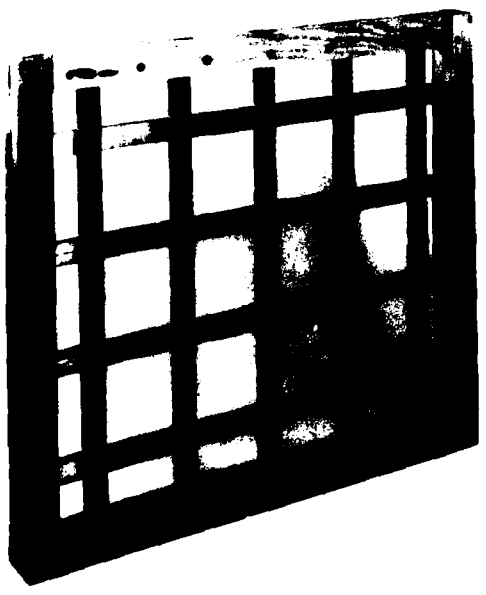

GRID NUMBER 4

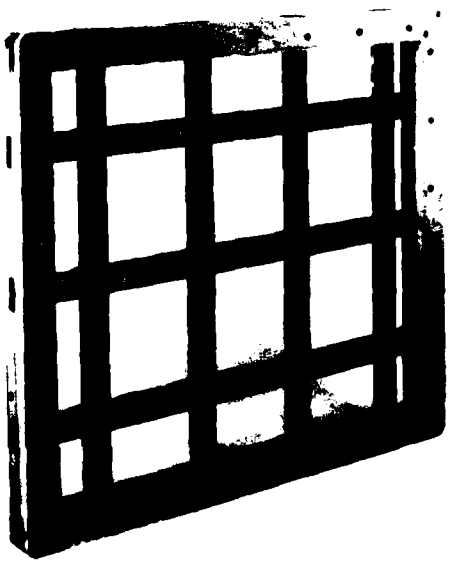

Figure 4. Photographs of Turbulence Generating Grids For The Boundary Layer Wind Tunnel

79-11-93-1

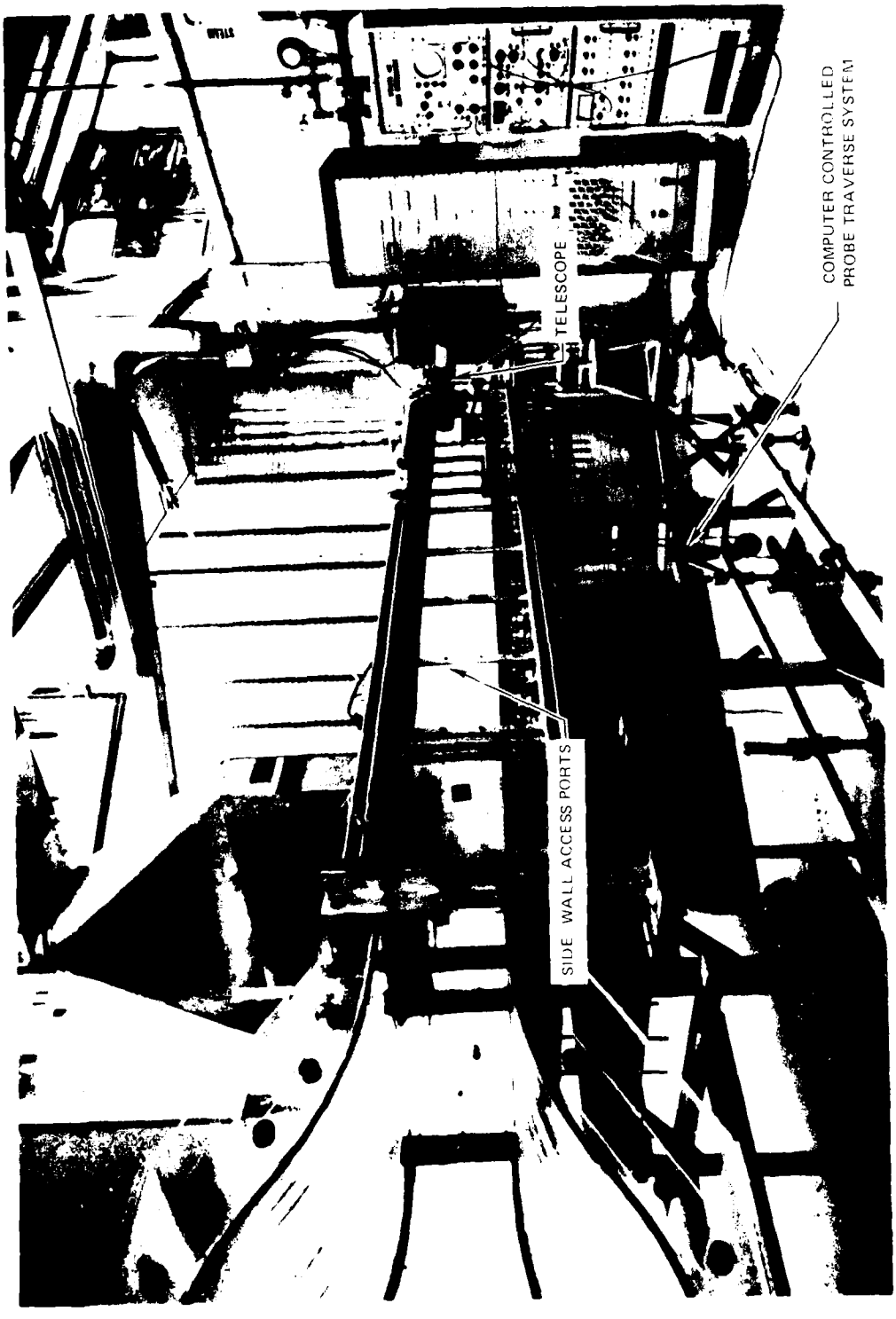

Figure 5 Photograph of UTRC Boundary Layer Wind Tunnel Test Section

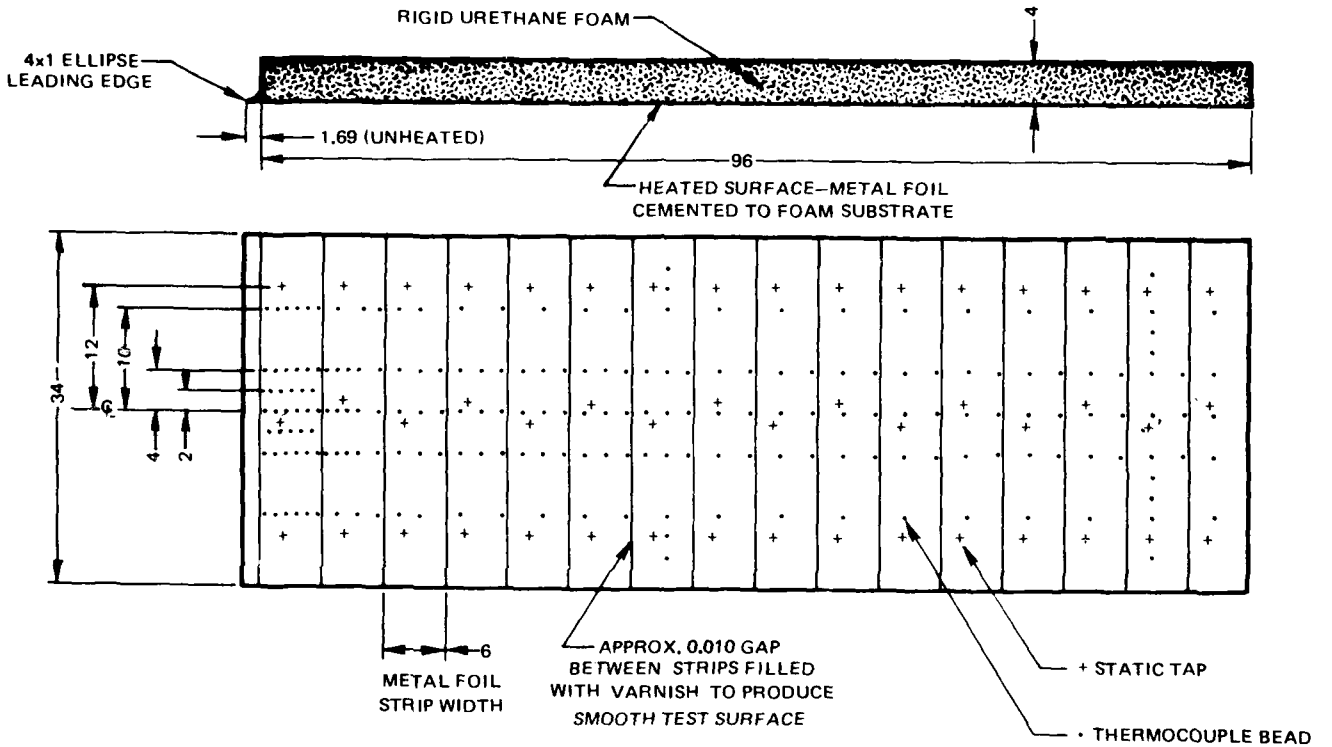

Figure 6. Instrumentation Diagram for the Uniform Heat Flux Flat Wall Model

76-05-70-4

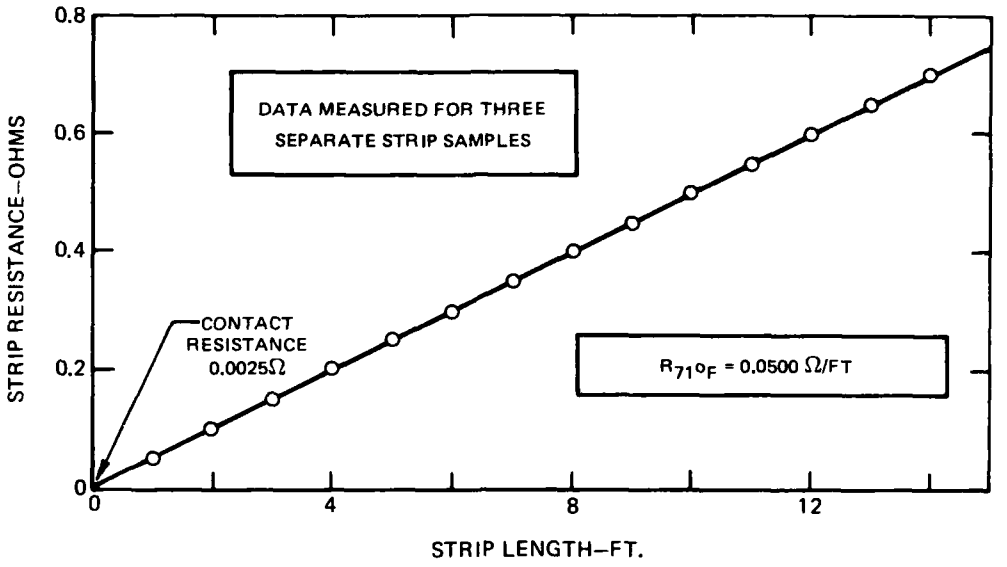

a. 316 STAINLESS STEEL FOIL RESISTANCE AT 71°F

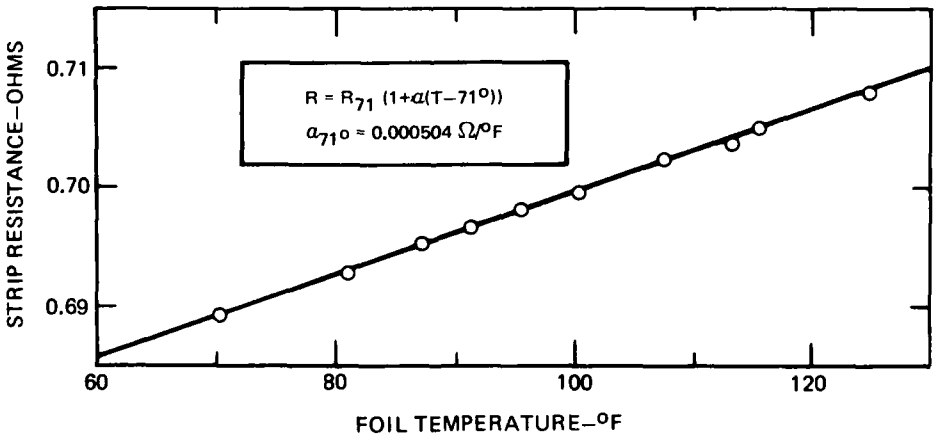

b. 316 STAINLESS STEEL FOIL TEMPERATURE RESISTANCE COEFFICIENT

Figure 7. Electrical Resistance Characteristics of the 316 Stainless Steel Foil Strip Used for the Heated Test Surface of the Uniform Heat Flux Flat Wall Model

79-05-70-5

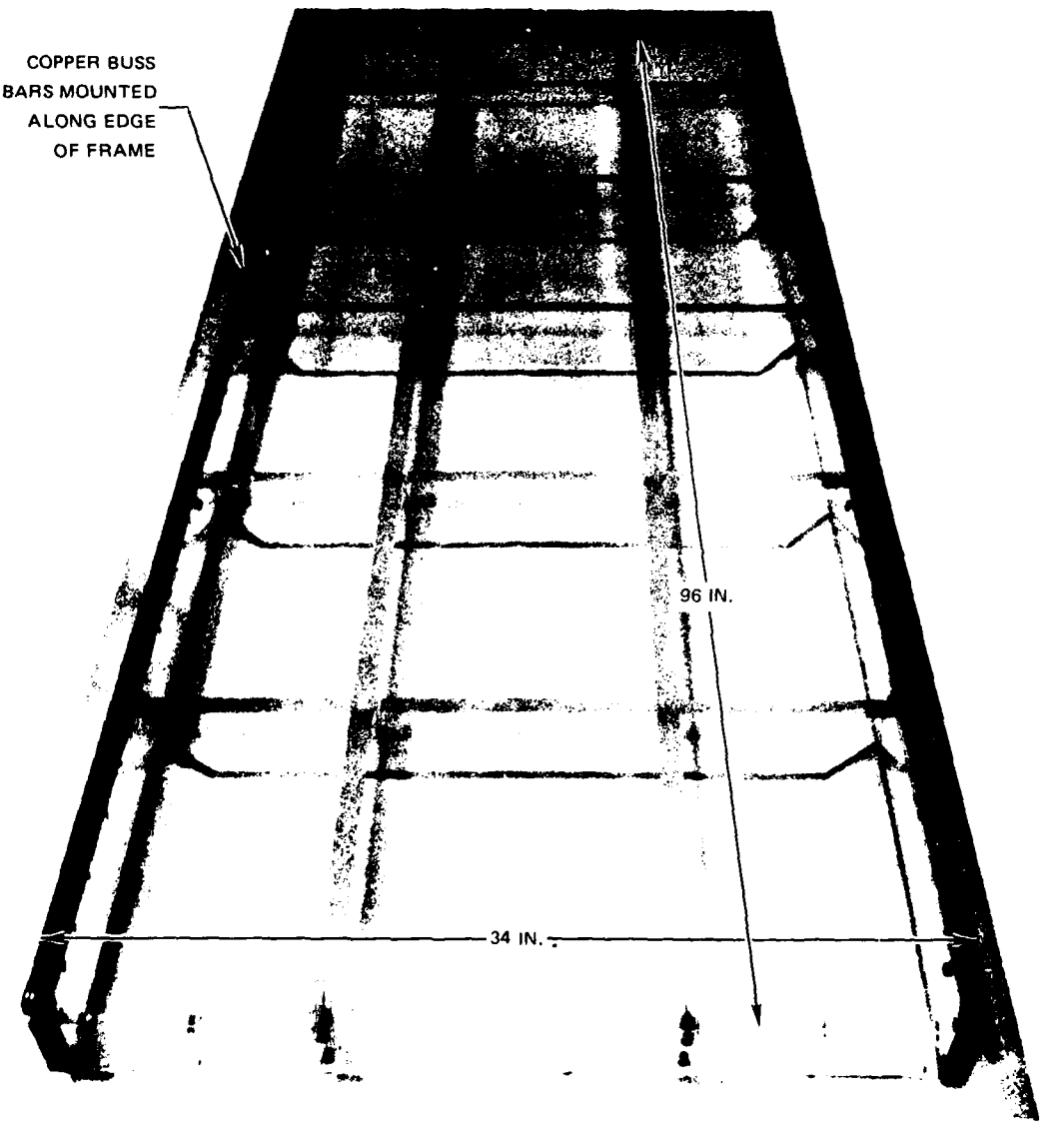

Figure 8. Photograph of the Assembled Plexiglas Frame for the Uniform Heat Flux Flat Wall Model with the Buss Bars Installed

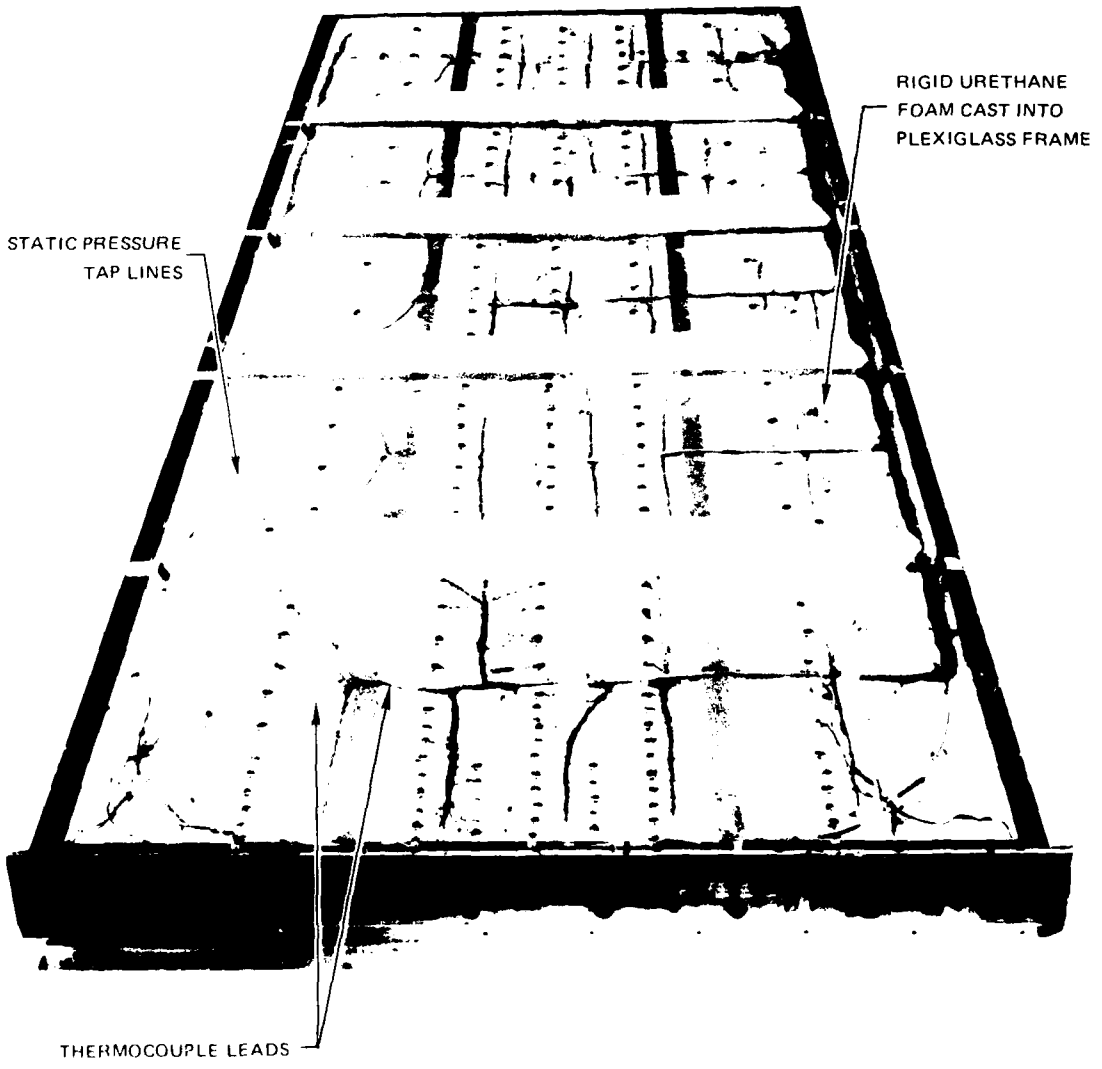

Figure 9. Photograph of the Backside of the Completely Assembled and Instrumented Uniform Heat Flux Flat Wall Model Showing the Routing of the Instrumentation Leads

79-05-70-2

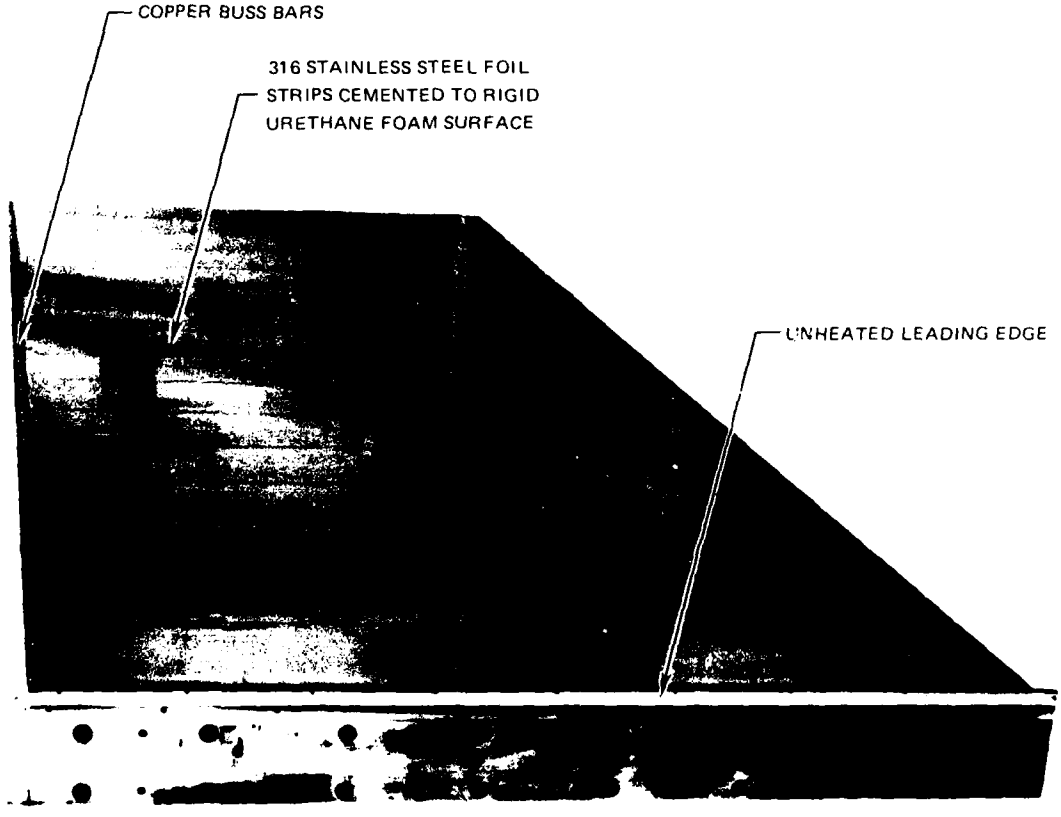

Figure 10. Photograph of Test Surface of the Uniform Heat Flux Flat Wall Model Prior to Coating with High Emissivity Paint

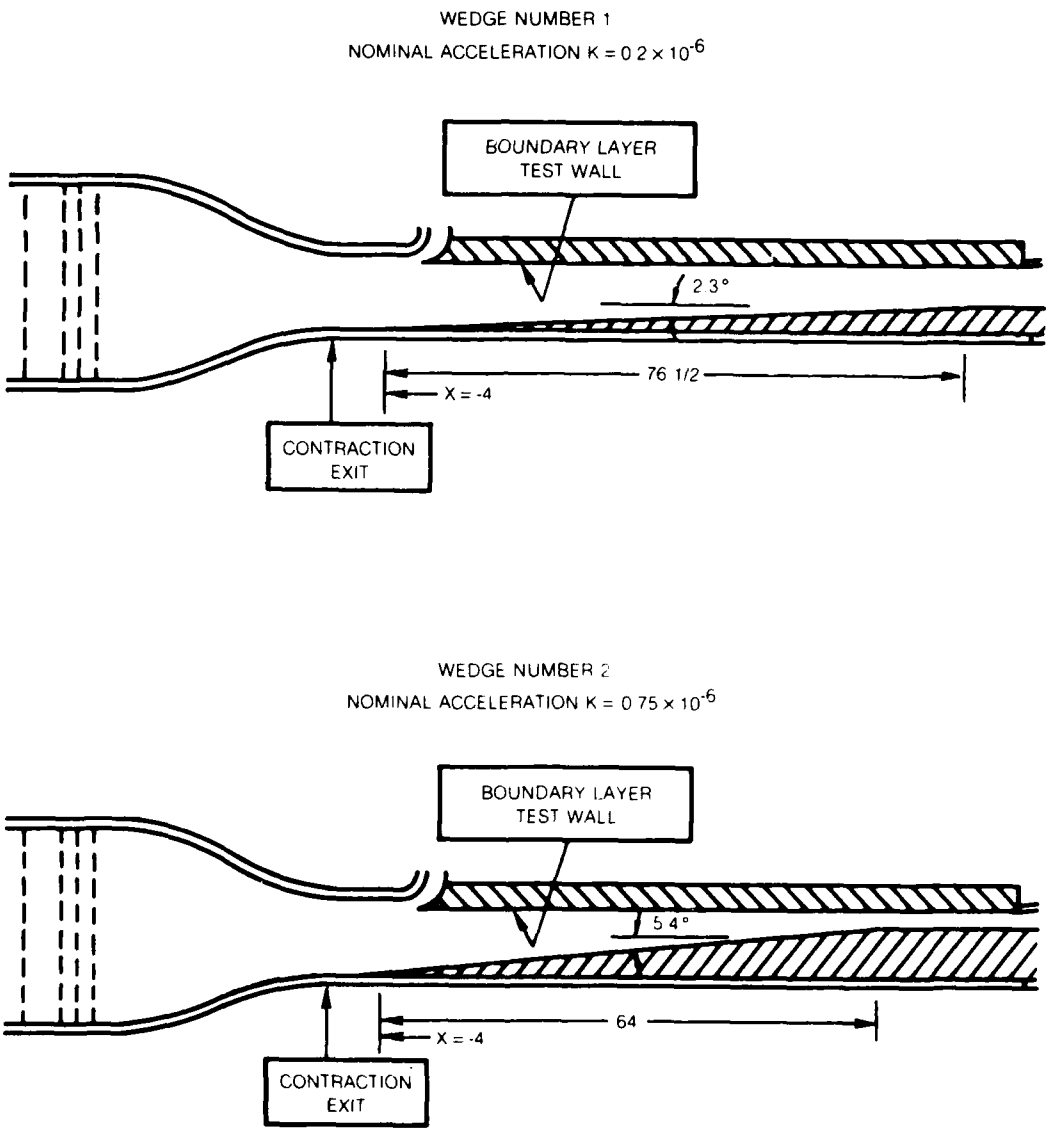

Figure 11. Diagrams of the Wedge Inserts Installed in the Wind Tunnel Test Section.

78-294-A

a) PROBE TIP DIMENSIONS MEASURED WITH NIKON MODEL II TOOLMAKERS MICROSCOPE

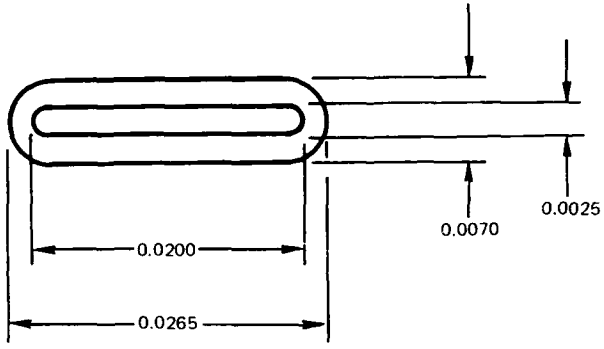

b) SIDE VIEW PHOTOGRAPH OF PROBE

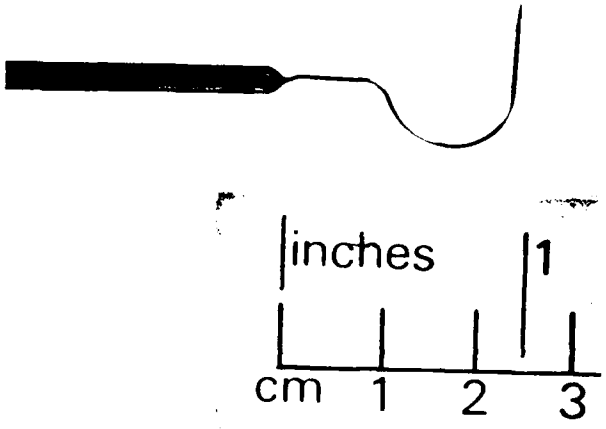

c) MAGNIFIED VIEWS OF PROBE TIP USING JONES AND LAMSON MODEL PC 14 SHADOWGRAPH

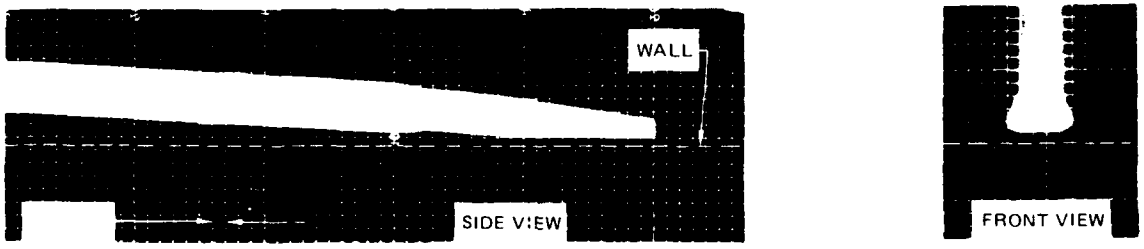

Figure 12. Typical Boundary Layer Pitot Probe Details

78-09-157-1

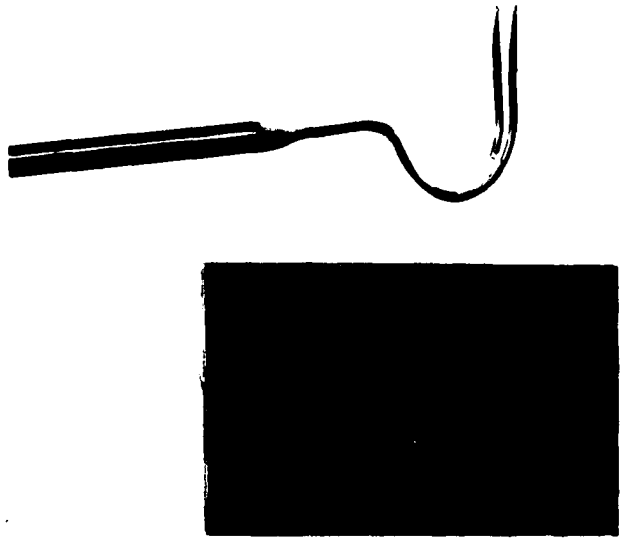

a) TEMPERATURE PROBE NO. 1

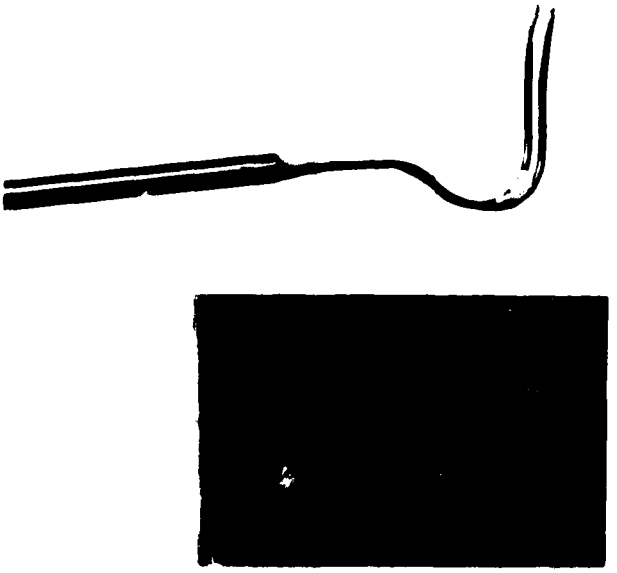

b) TEMPERATURE PROBE NO. 2

Figure 13. Typical Boundary Layer Thermocouple Probes

78-294-D
78-294-E

78-09-157-3

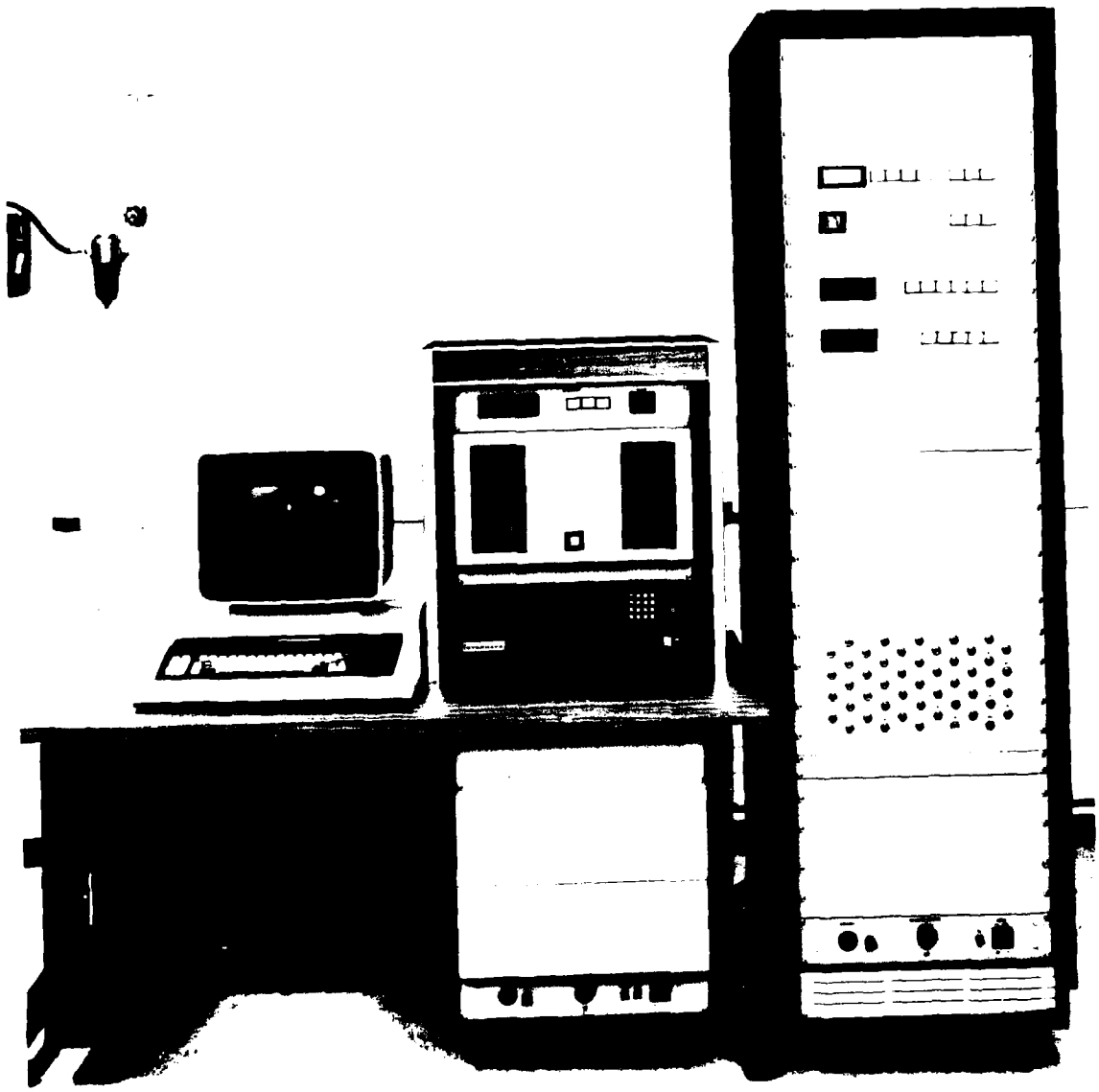

Figure 14. UTRC Boundary Layer Wind Tunnel Data Acquisition System

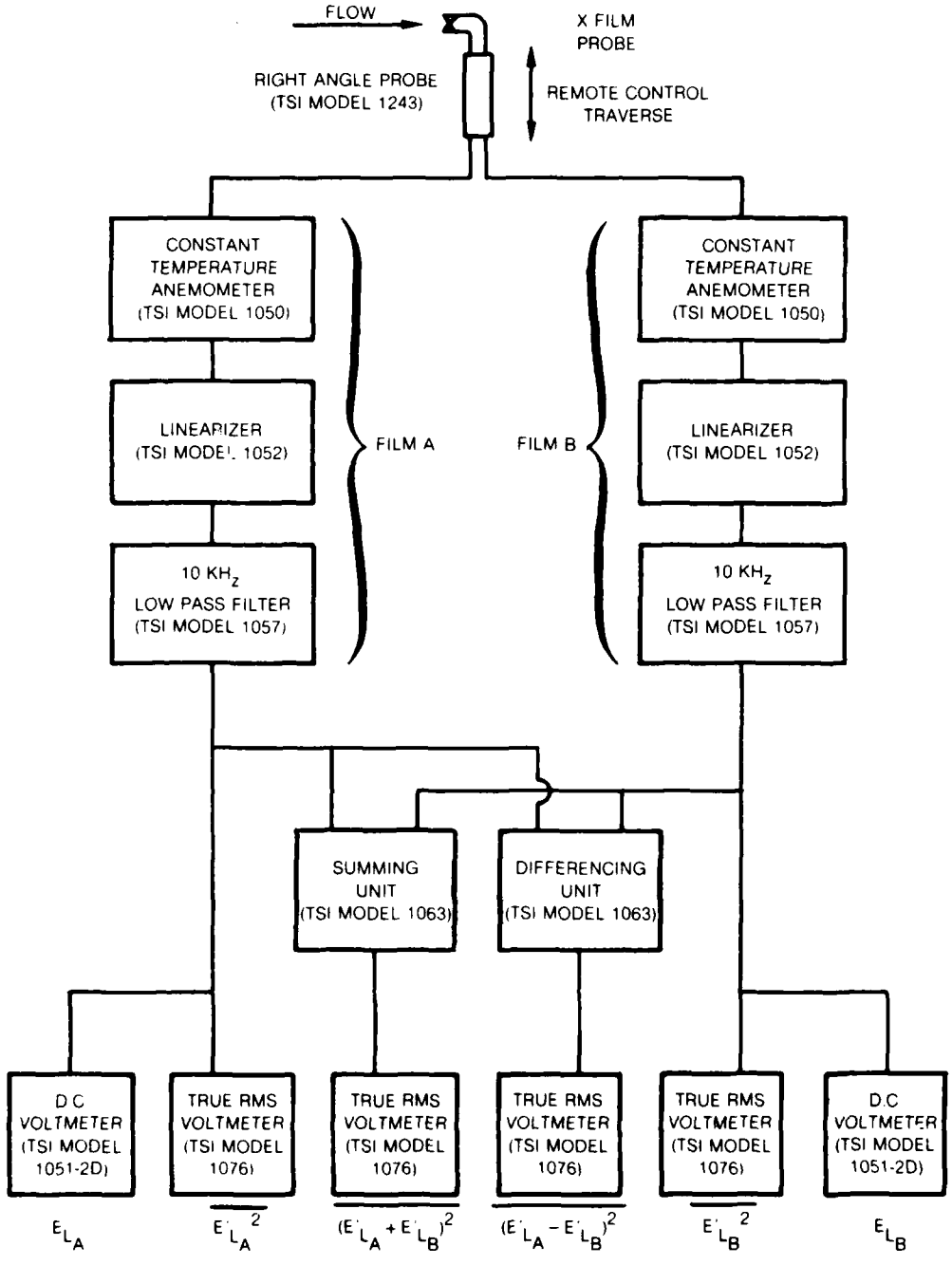

Figure 15. Block Diagram of Instrumentation Arrangement for Obtaining Multi-component Turbulence Measurements

80-2-72-7

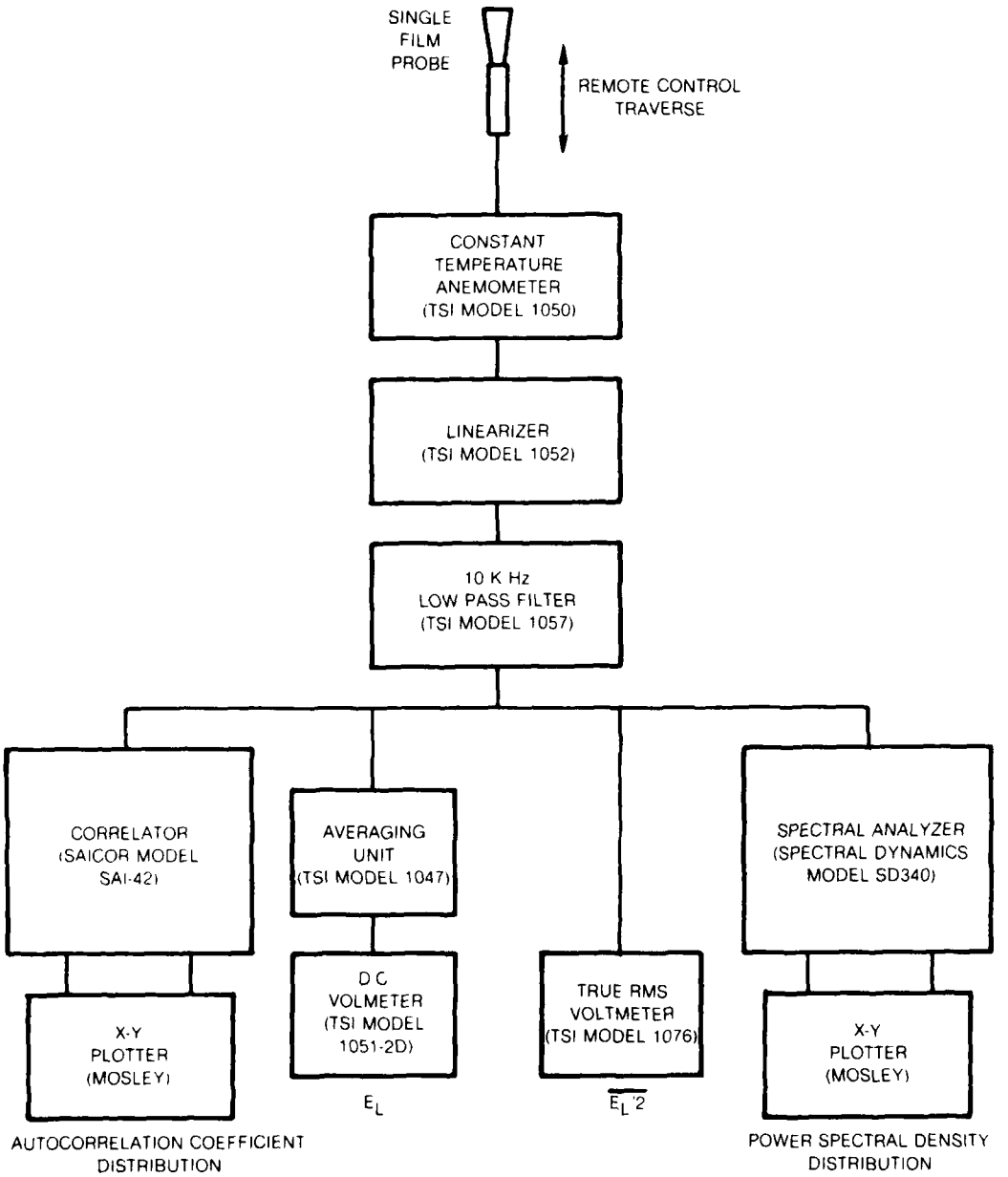

Figure 16. Block Diagram of Instrumentation Arrangement for Obtaining Length Scale and Spectral Distribution Data.

80-2-72-9

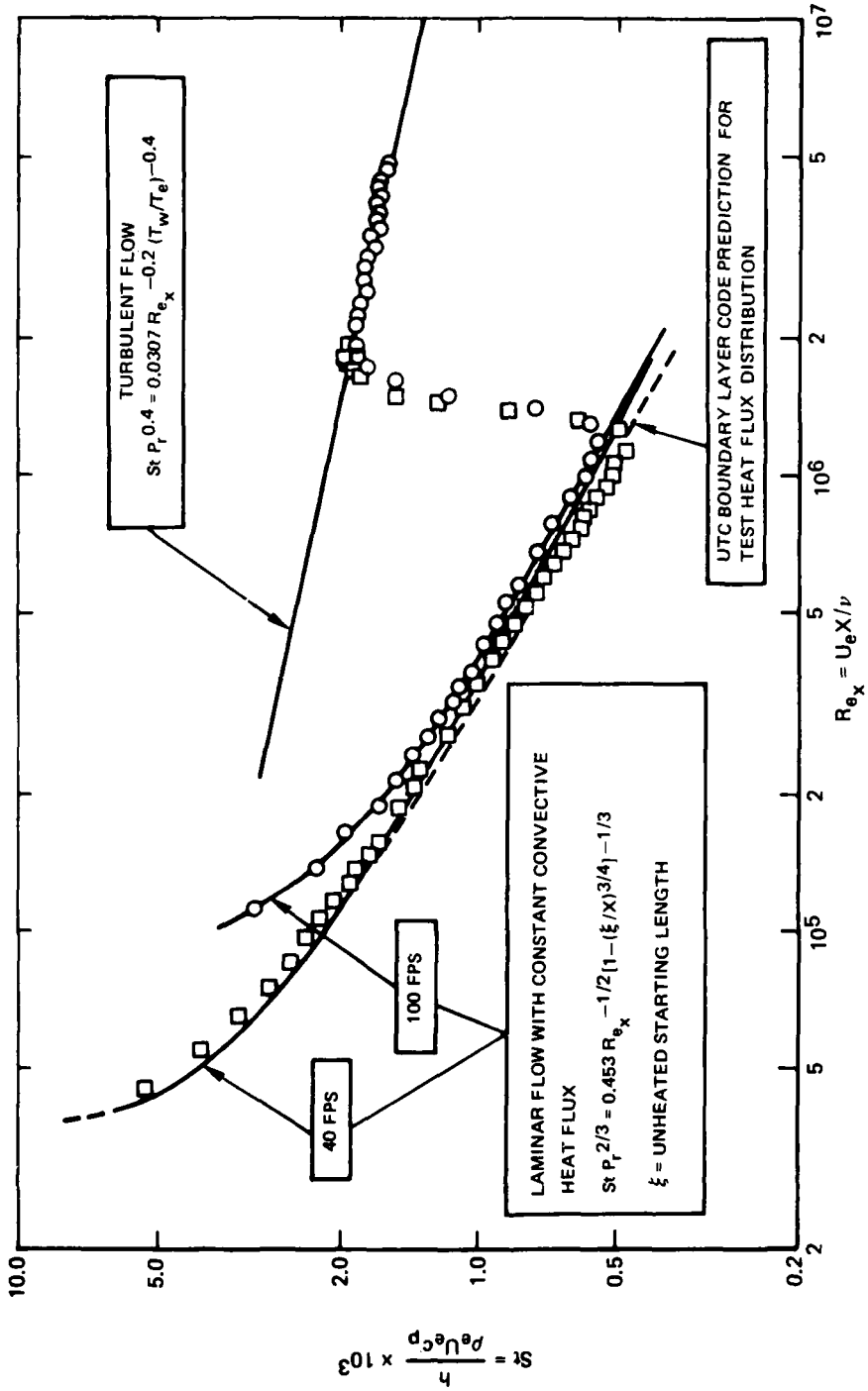

Figure 17. Heat Transfer Distribution Along the Uniform Heat Flux Test Wall For The Minimum Freestream Turbulence Configuration and Natural Transition of the Test Wall Boundary Layer

79-05-70-7

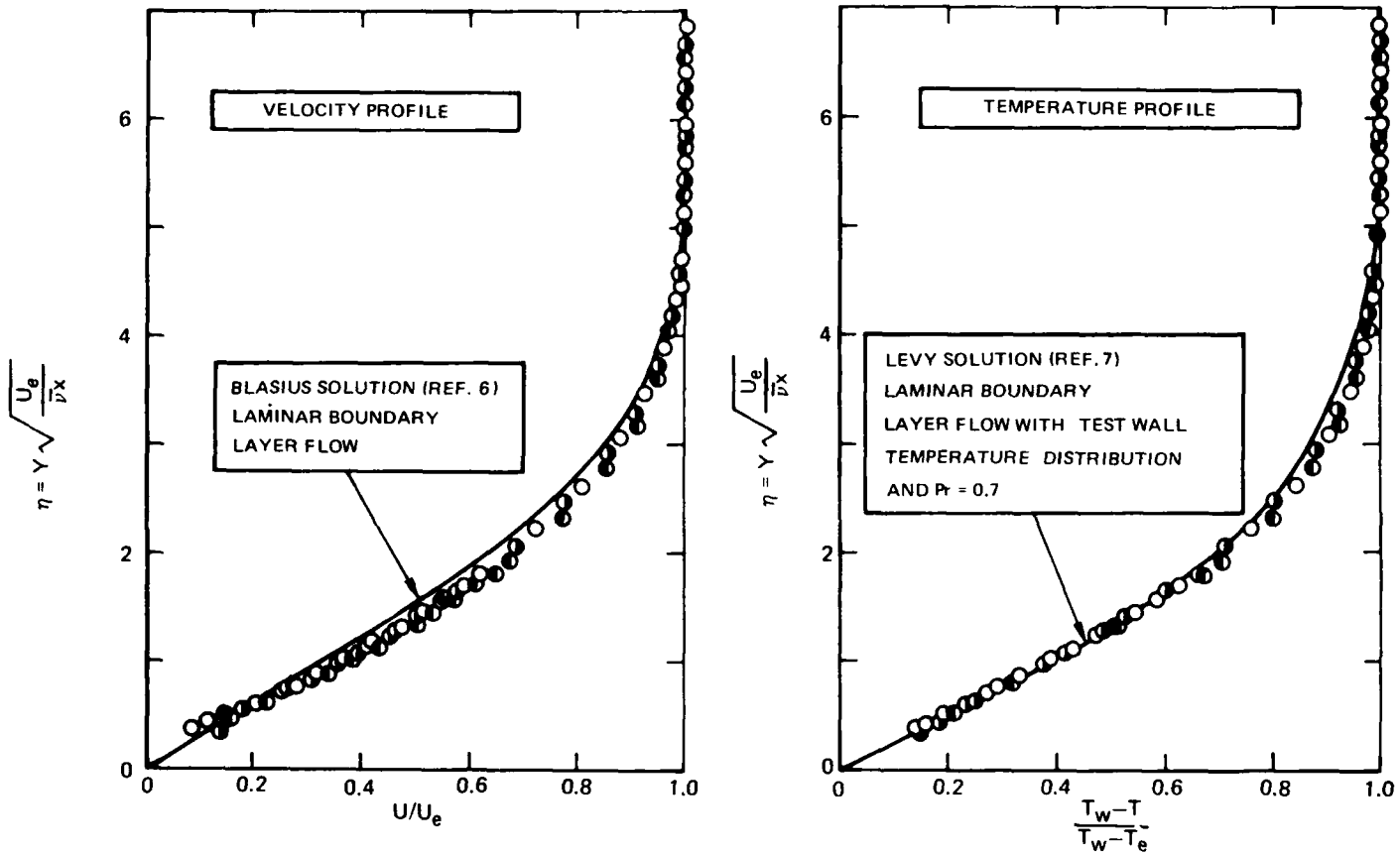

Figure 18: Velocity and Temperature Profiles Measured Upstream of Boundary Layer Transition For The Minimum Freestream Turbulence Test Condition ($Re_x = 0.63 \times 10^6$) at Three Transverse Locations ○ Tunnel C_L: ◐ Z = +6 Inches; ◑ Z = -6 Inches

79-06-70-6

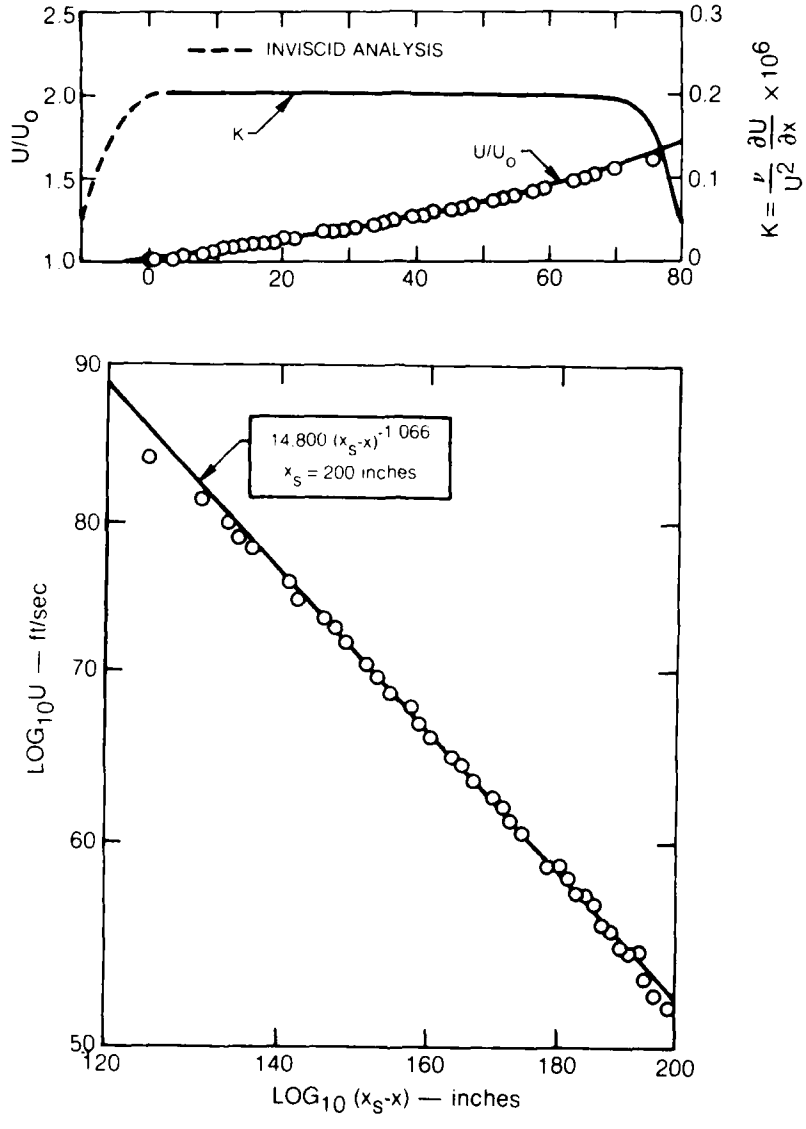

Figure 19: Velocity Distribution Along the Flat Test Wall With the 2.3° Angle Wedge (Wedge 1) and No Turbulence Grid

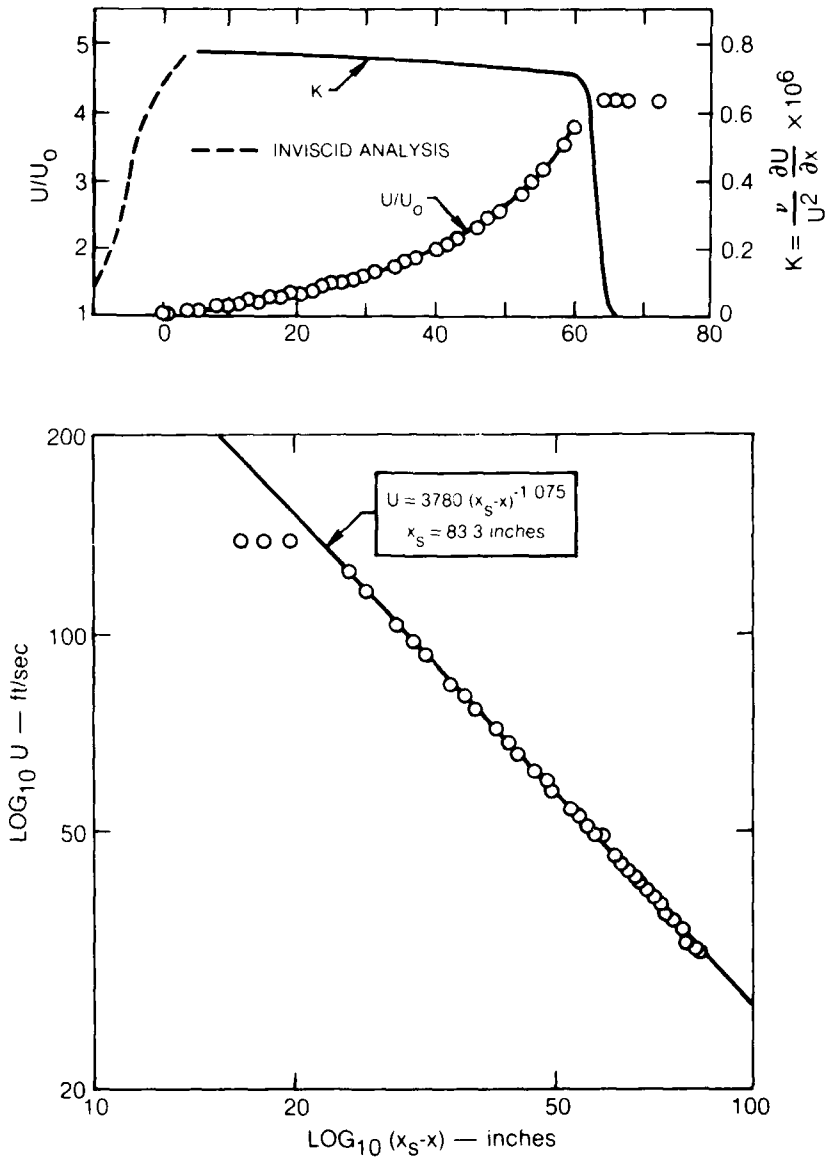

Figure 20: Velocity Distribution Along the Flat Test Wall With the 5.4° Angle Wedge (Wedge 2) and No Turbulence Grid

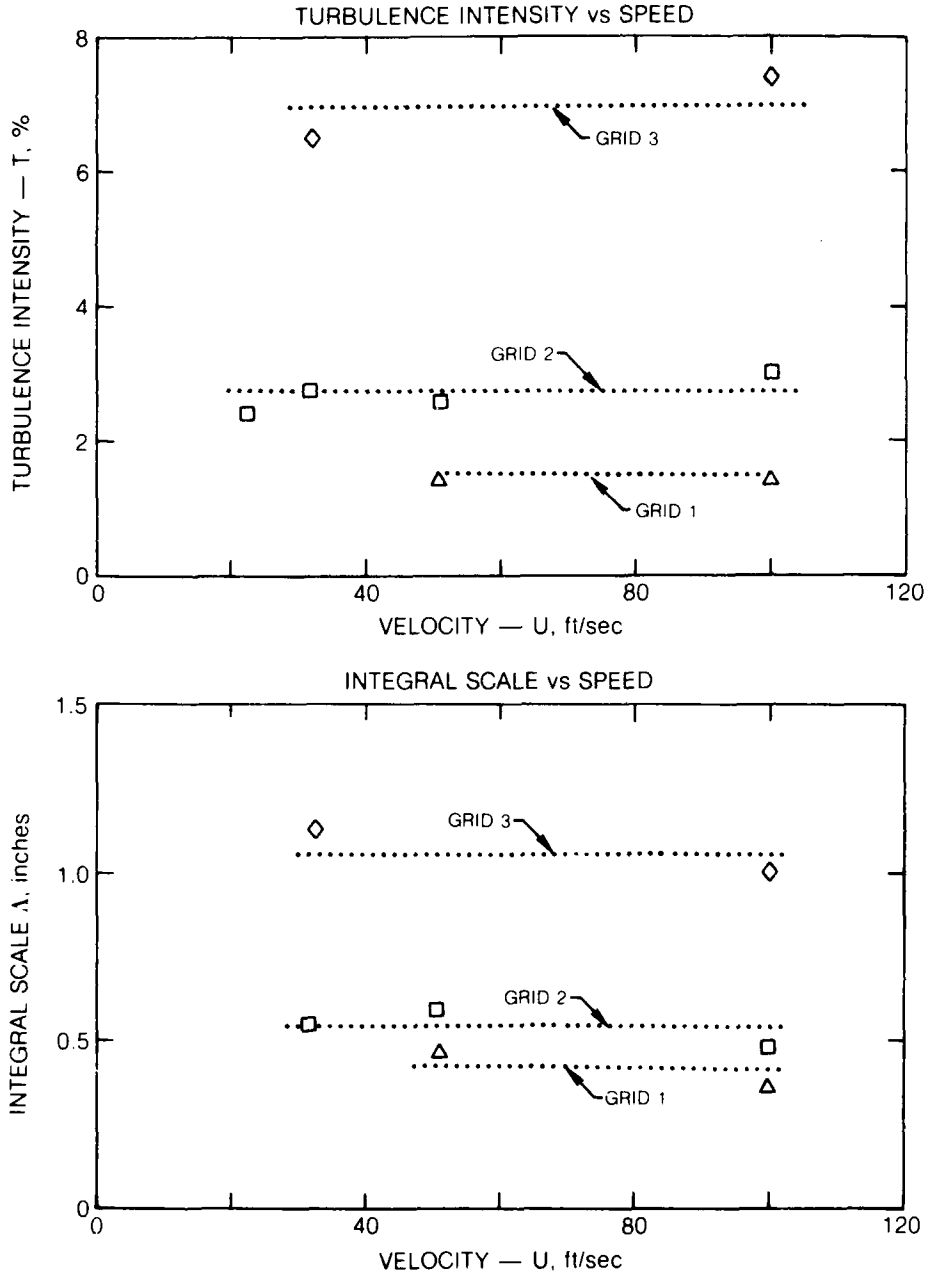

Figure 21: Turbulence Intensity and Longitudinal Integral Scale as a Function of Speed at the Entrance to the Tunnel Test Section - Turbulence Grids 1, 2 and 3

81-3-1-4

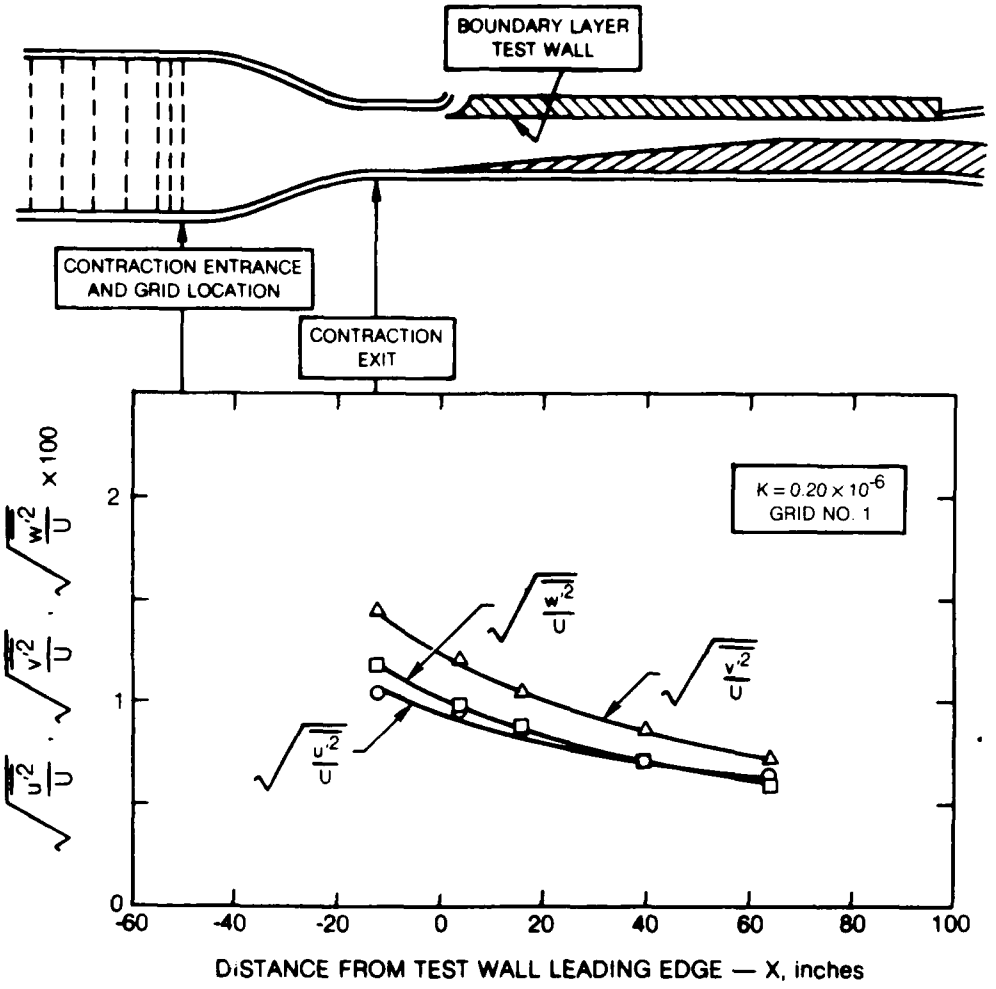

Figure 22: Distribution of the Components of the Turbulence In The Test Section for K = 0.20 x 10^{-6} and Grid 1

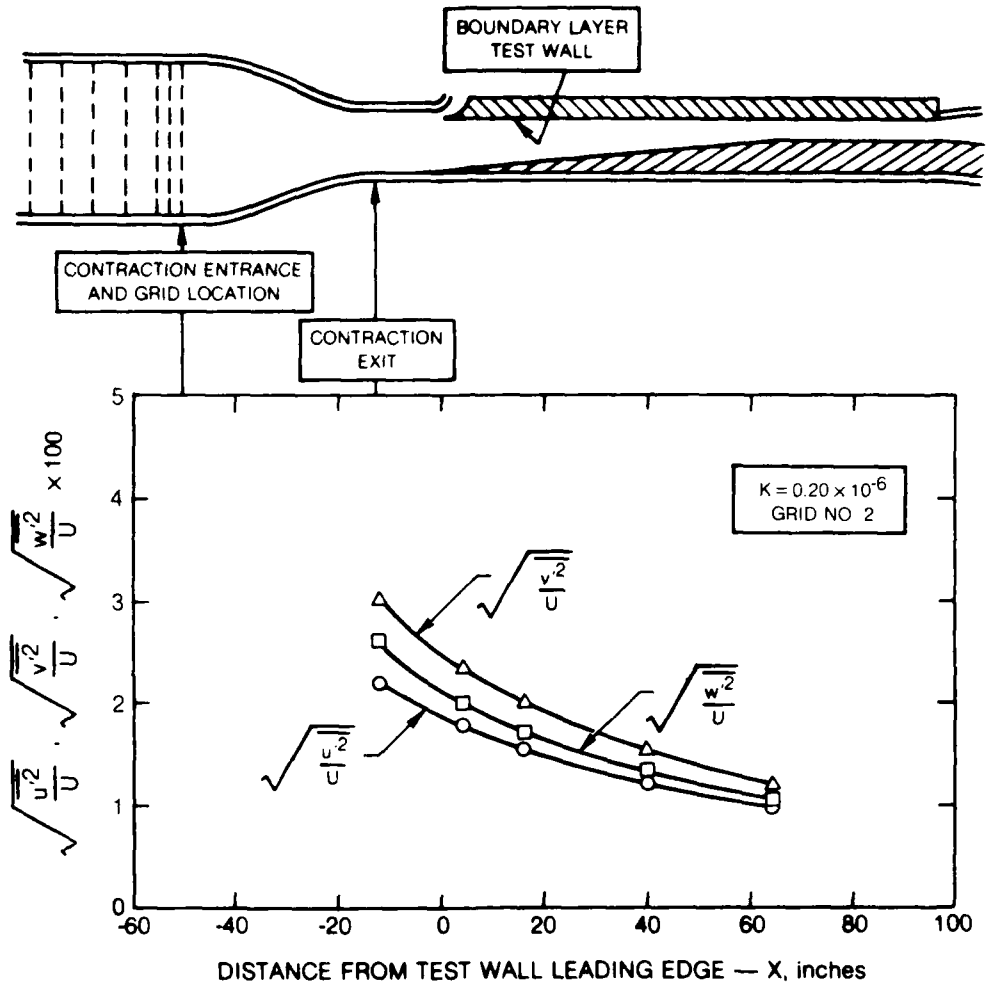

Figure 23: Distribution of the Components of the Turbulence In The Test Section for K = 0.20 x 10^{-6} and Grid 2

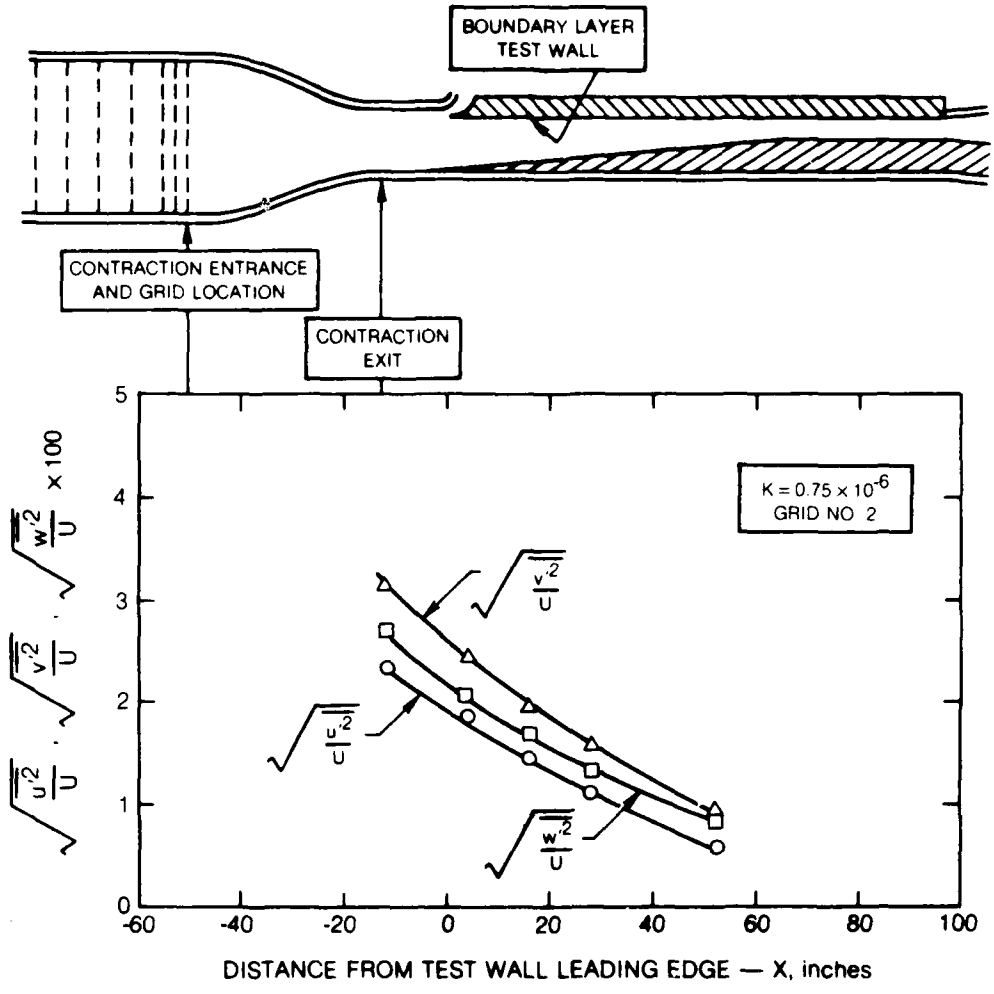

Figure 24: Distribution of the Components of the Turbulence In The Test Section for K ≈ 0.75 x 10^{-6} and Grid 2

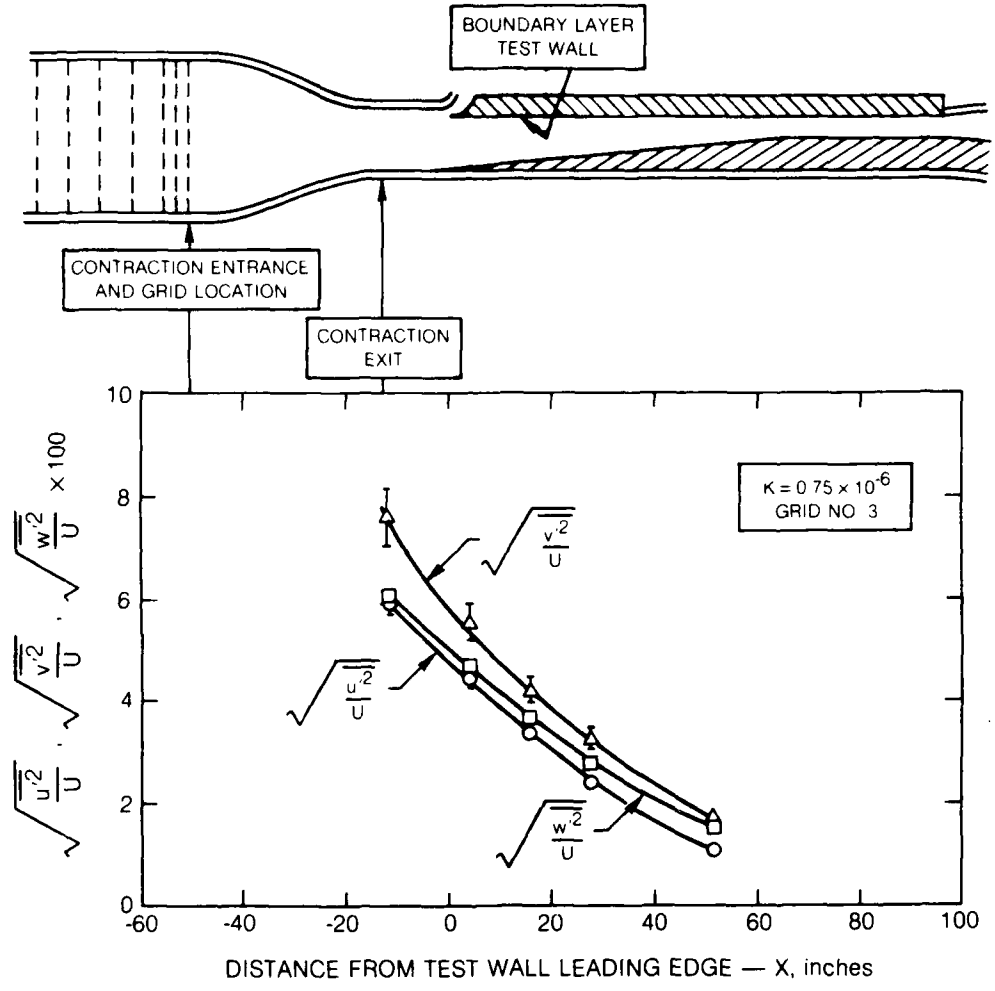

Figure 25: Distribution of the Components of the Turbulence In The Test Section for K = 0.75 x 10^{-6} and Grid 3

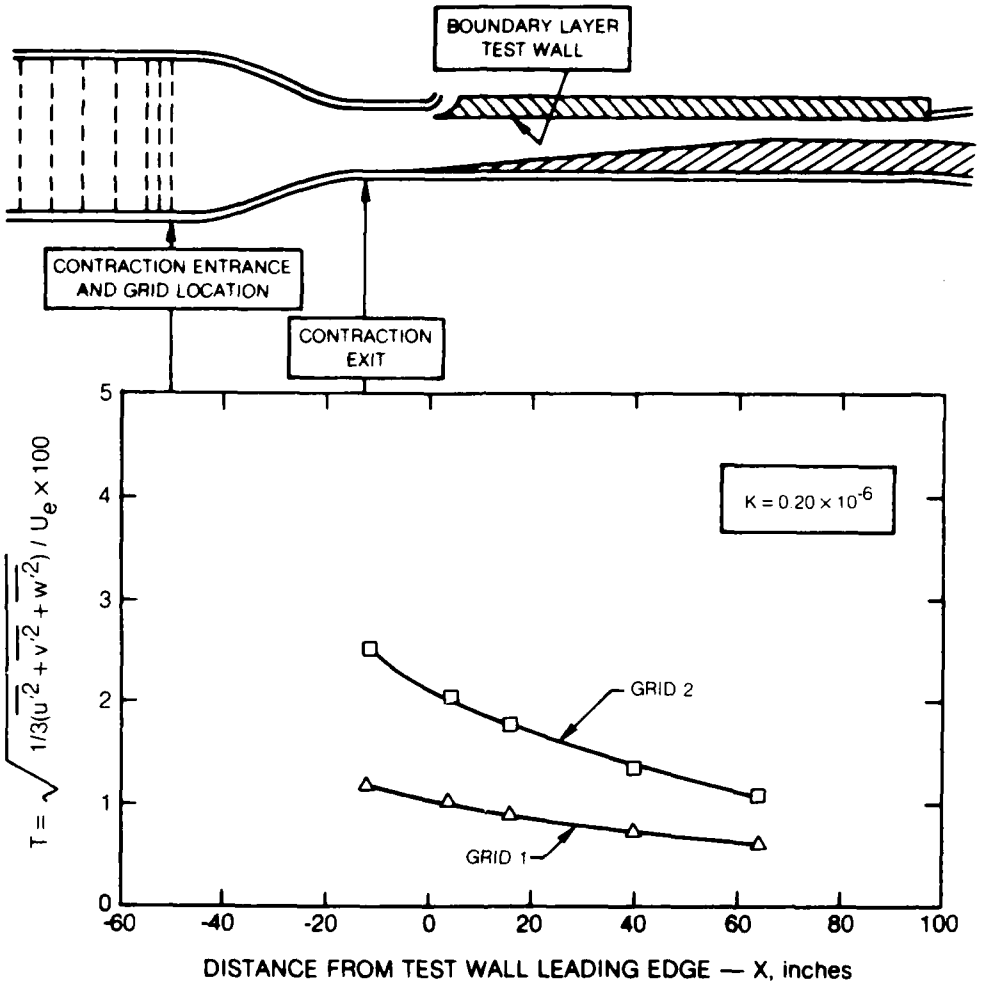

Figure 26: Distributions of Total Turbulence Intensity In The Test Section For $K = 0.20 \times 10^{-6}$

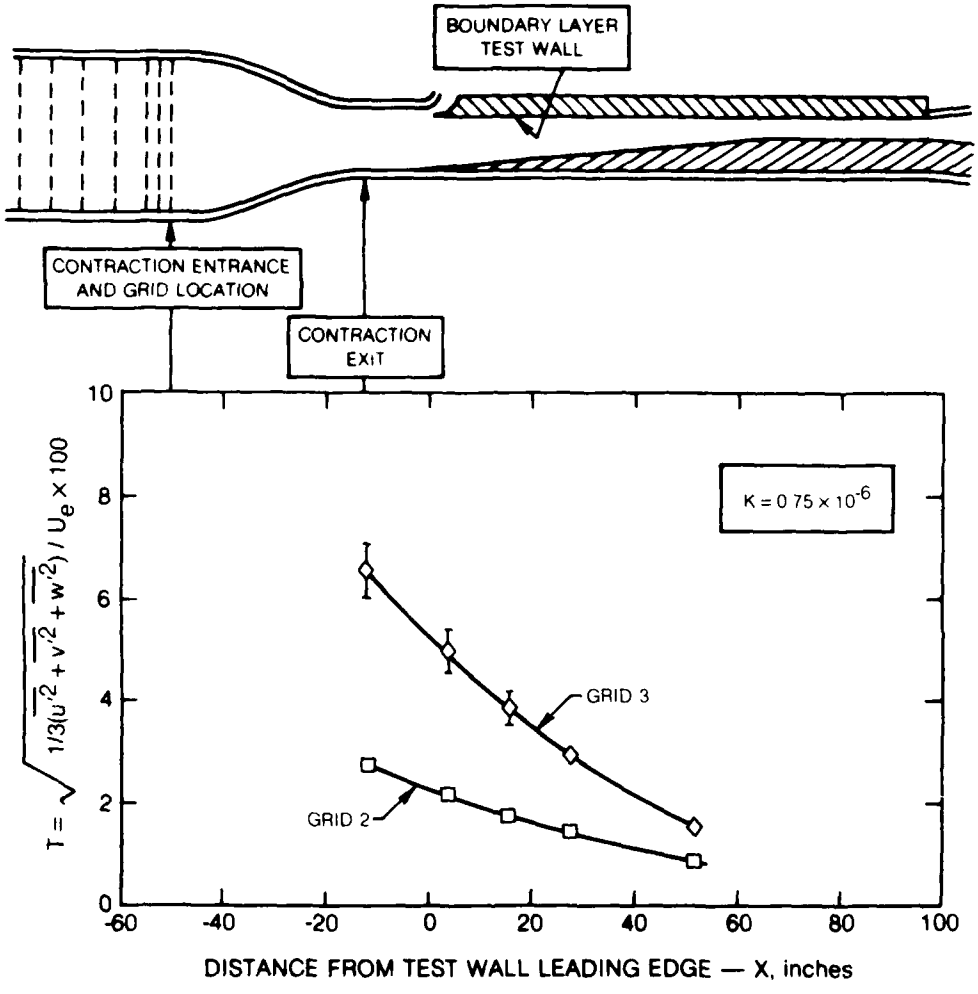

Figure 27: Distributions of Total Turbulence Intensity In The Test Section for K = 0.75 x 10^{-6}

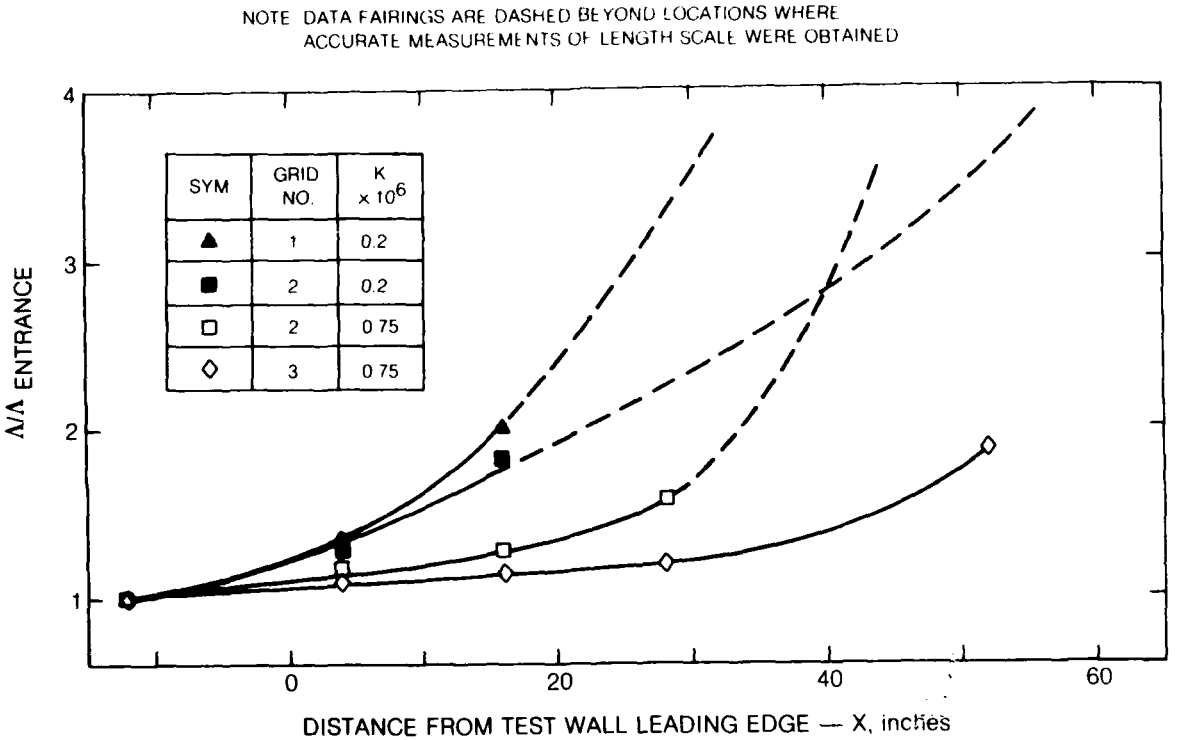

Figure 28: Distributions of the Streamwise Integral Length Scale In The Test Section for the Four Acceleration/Grid Combinations

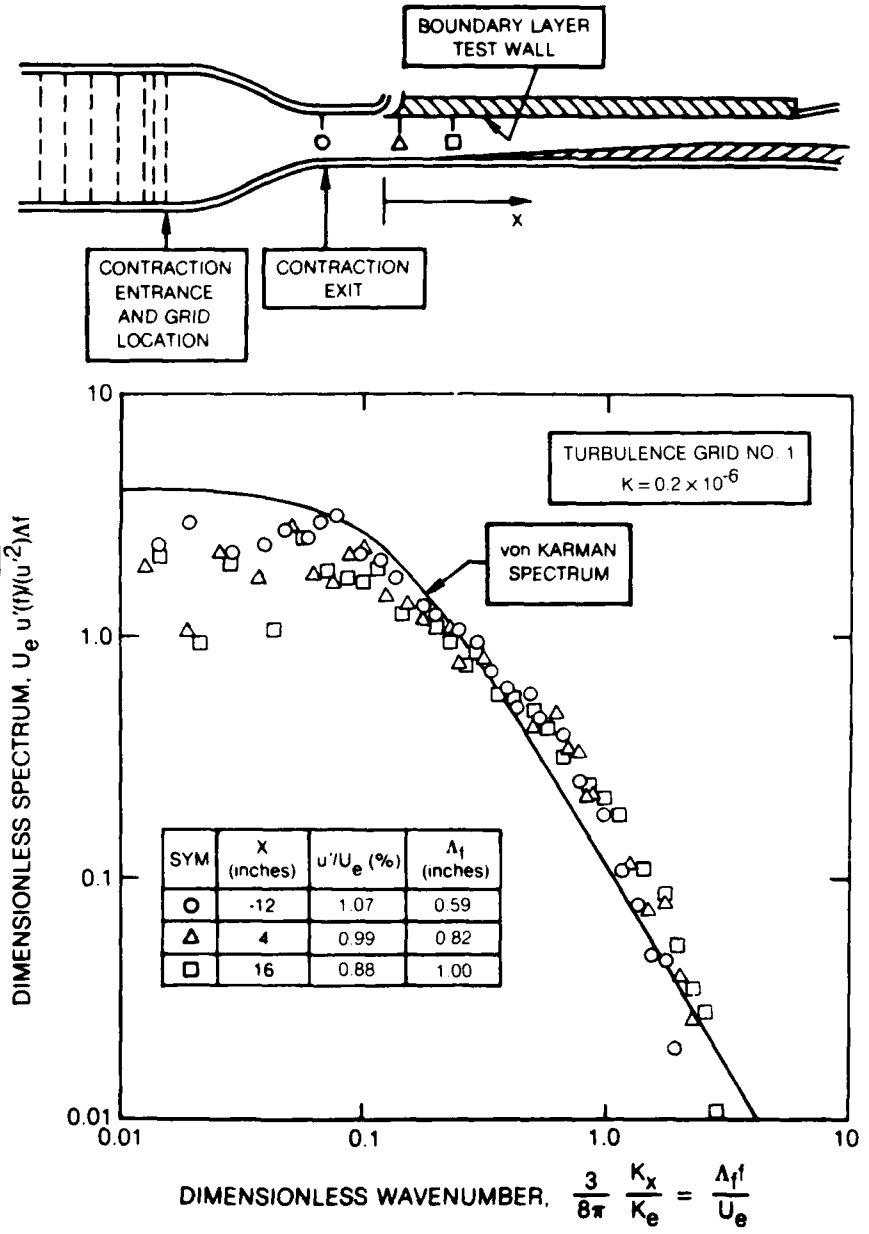

Figure 29: Free-Stream Power Spectral Density Distributions Measured at Various Streamwise Location in the Test Section
K = 0.20 x 10^{-6}; Grid 1

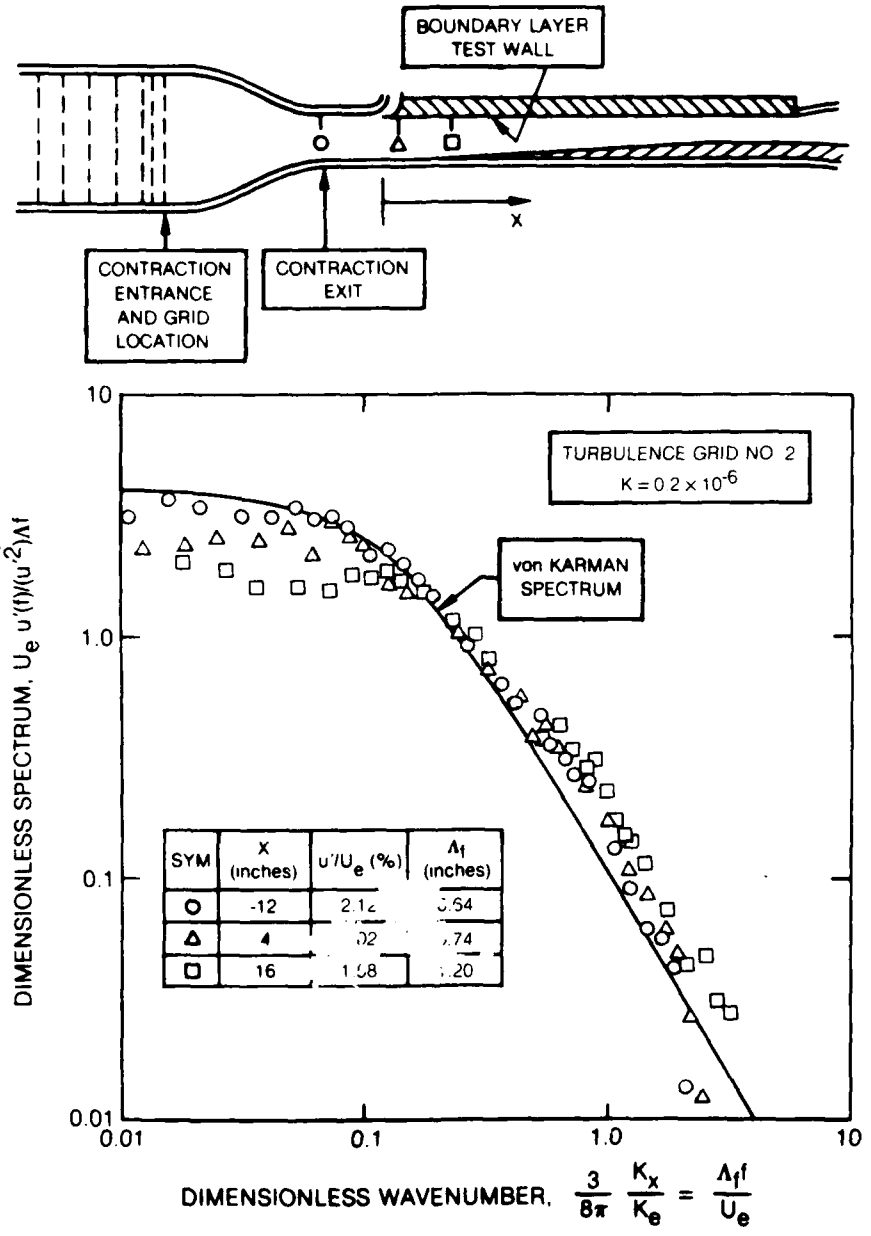

Figure 30: Free-Stream Power Spectral Density Distributions Measured at Various Streamwise Locations in the Test Section
K = 0.20 x 10^{-6}; Grid 2

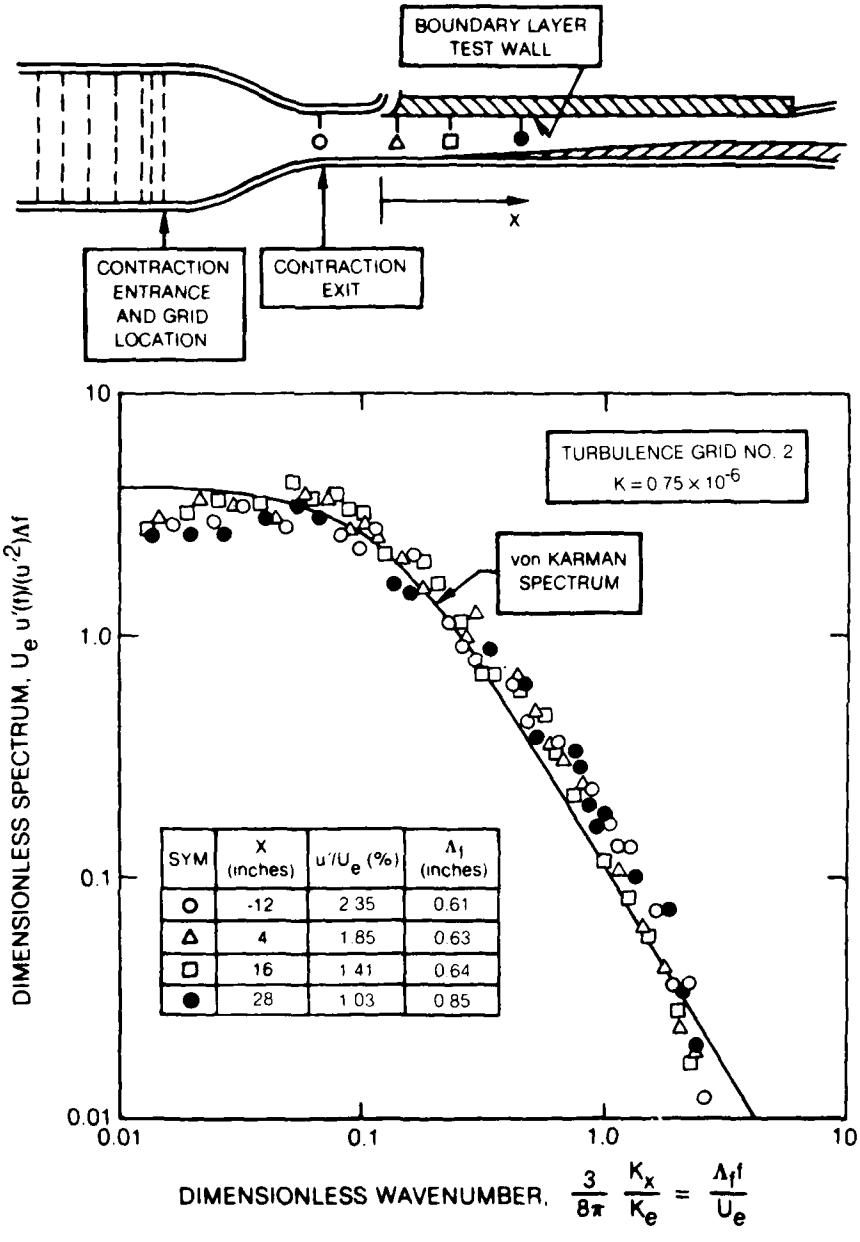

Figure 31: Free-Stream Power Spectral Density Distributions Measured at Various Streamwise Locations in the Test Section
K = 0.75 x 10^{-6}; Grid 2

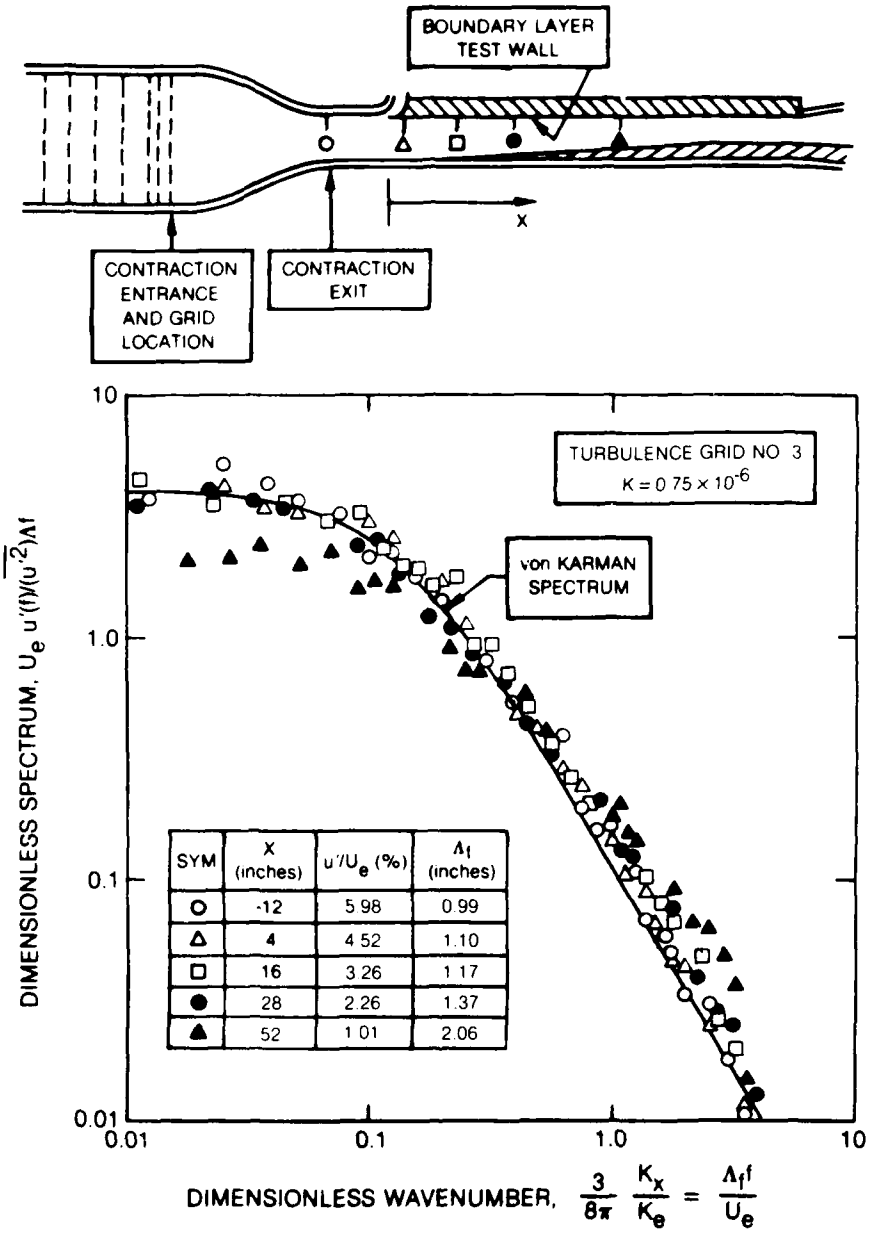

Figure 32: Free-Stream Power Spectral Density Distributions Measured at Various Streamwise Locations in the Test Section
K = 0.75 x 10^{-6}; Grid 3

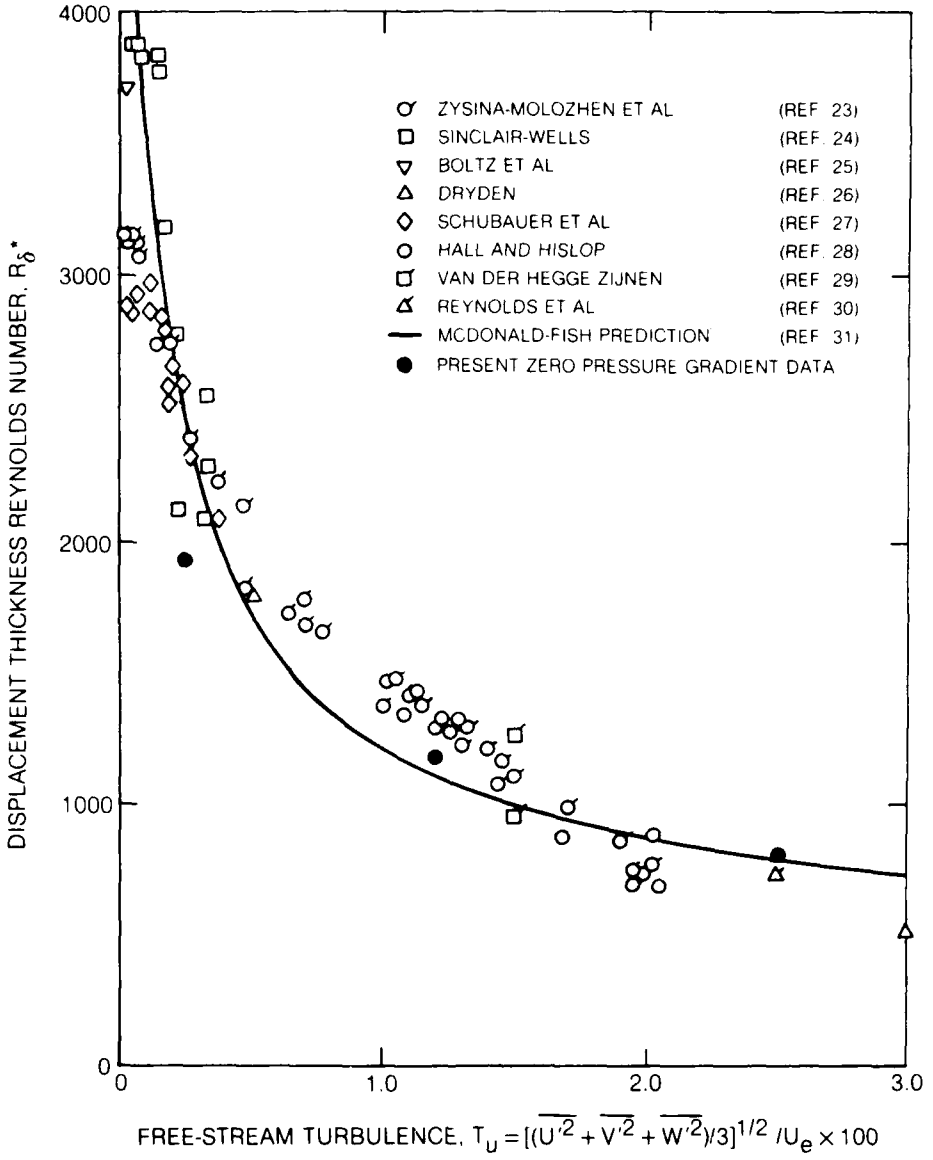

Figure 33: Effect of Free-Stream Turbulence Upon The Transition Reynolds Number For Zero Pressure Gradient Flow

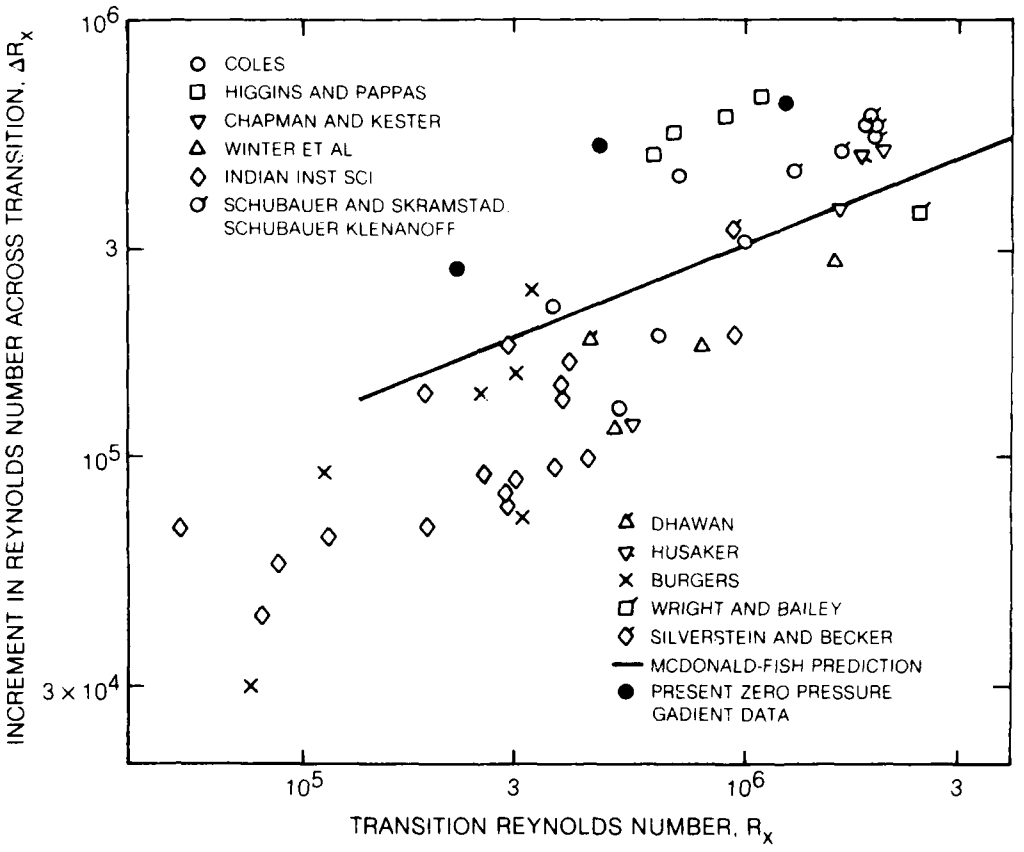

Figure 34: Variation of Transition Length With Transition Reynolds Number For Zero Pressure Gradient Flow

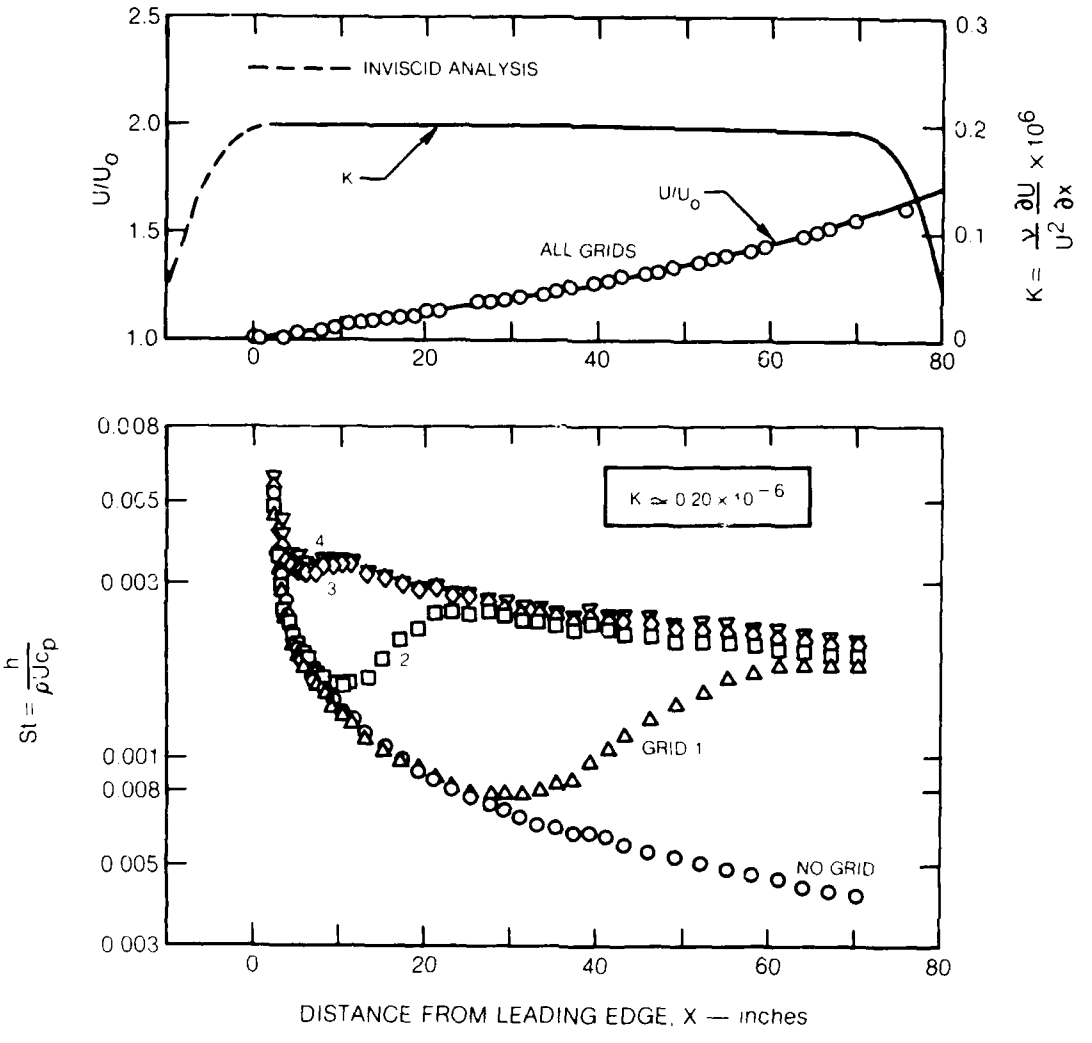

Figure 35: Acceleration and Heat Transfer Distributions for Wedge 1 With 5 Free-Stream Turbulence Levels

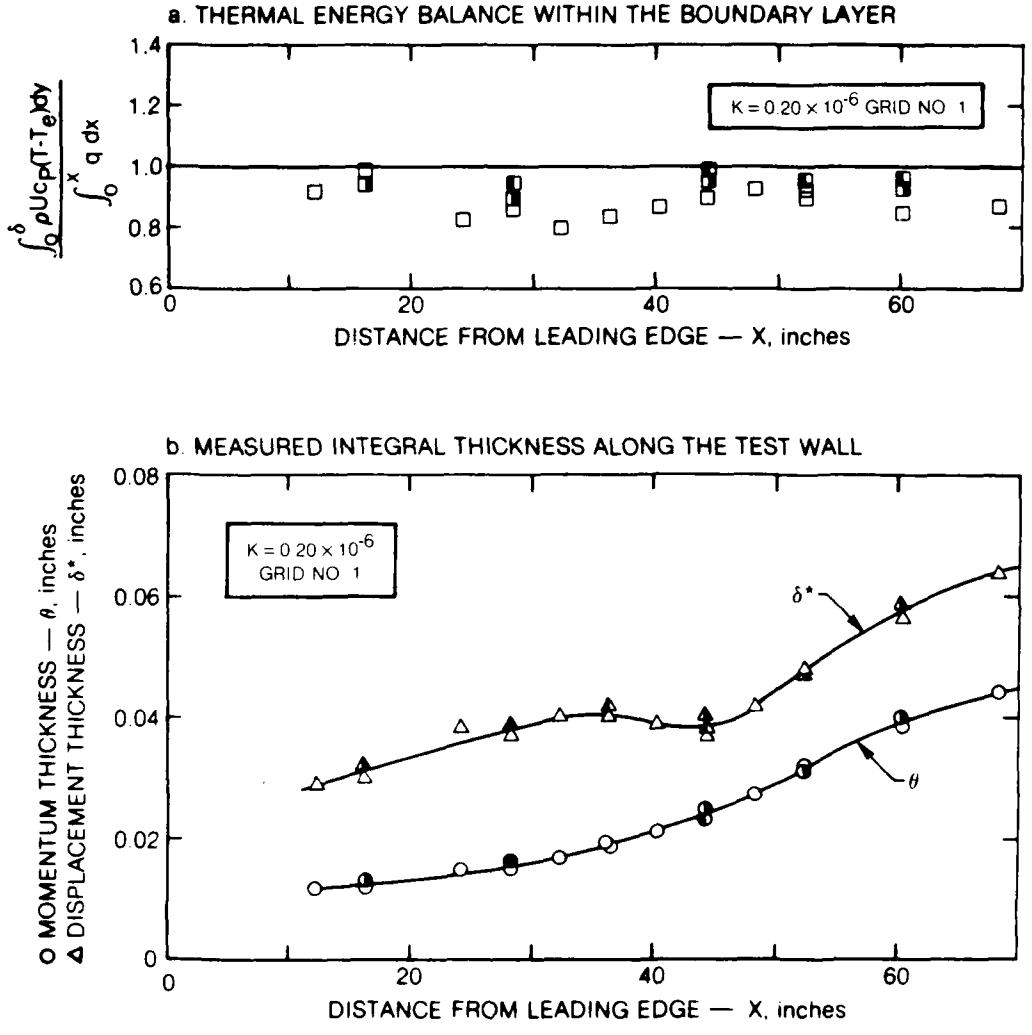

Figure 36: Boundary Layer Properties Measured With K = 0.20 x 10^{-6} And Turbulence Grid 1 O Tunnel C_L; ◑ Z = +6 Inches; ◐ Z = -6 Inches

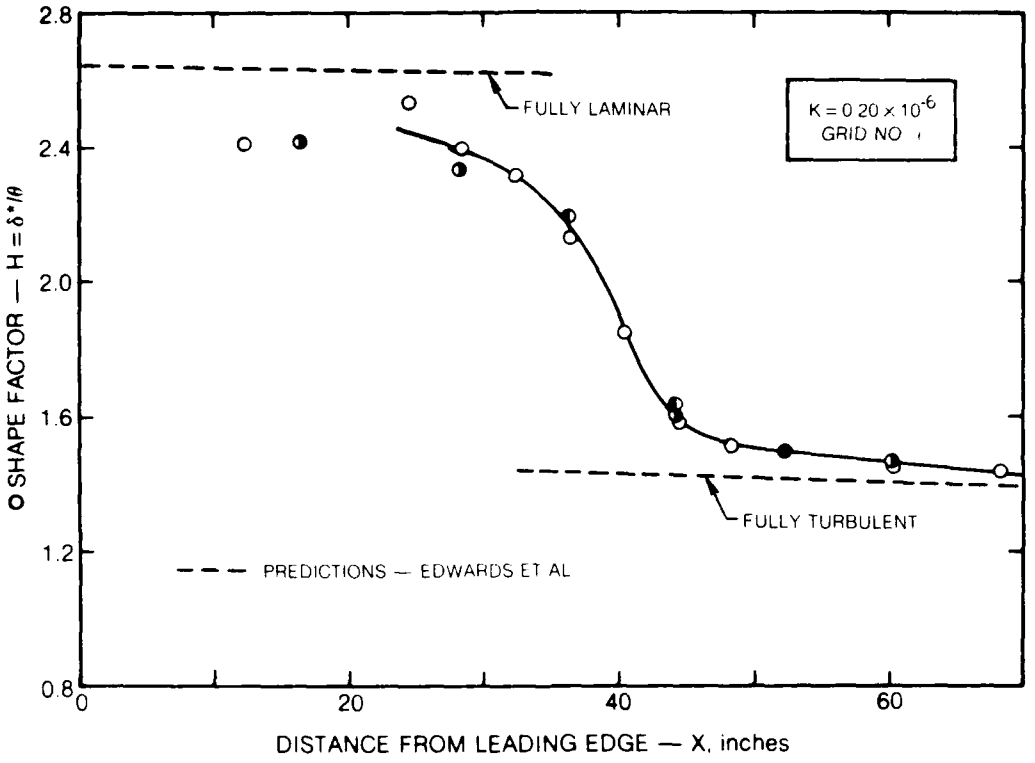

Figure 37: Boundary Layer Shape Factor Measured With K = 0.20 x 10^{-6} and Turbulence Grid 1 ○Tunnel C_L; ◑ Z = +6 Inches; ◐Z = -6 Inches

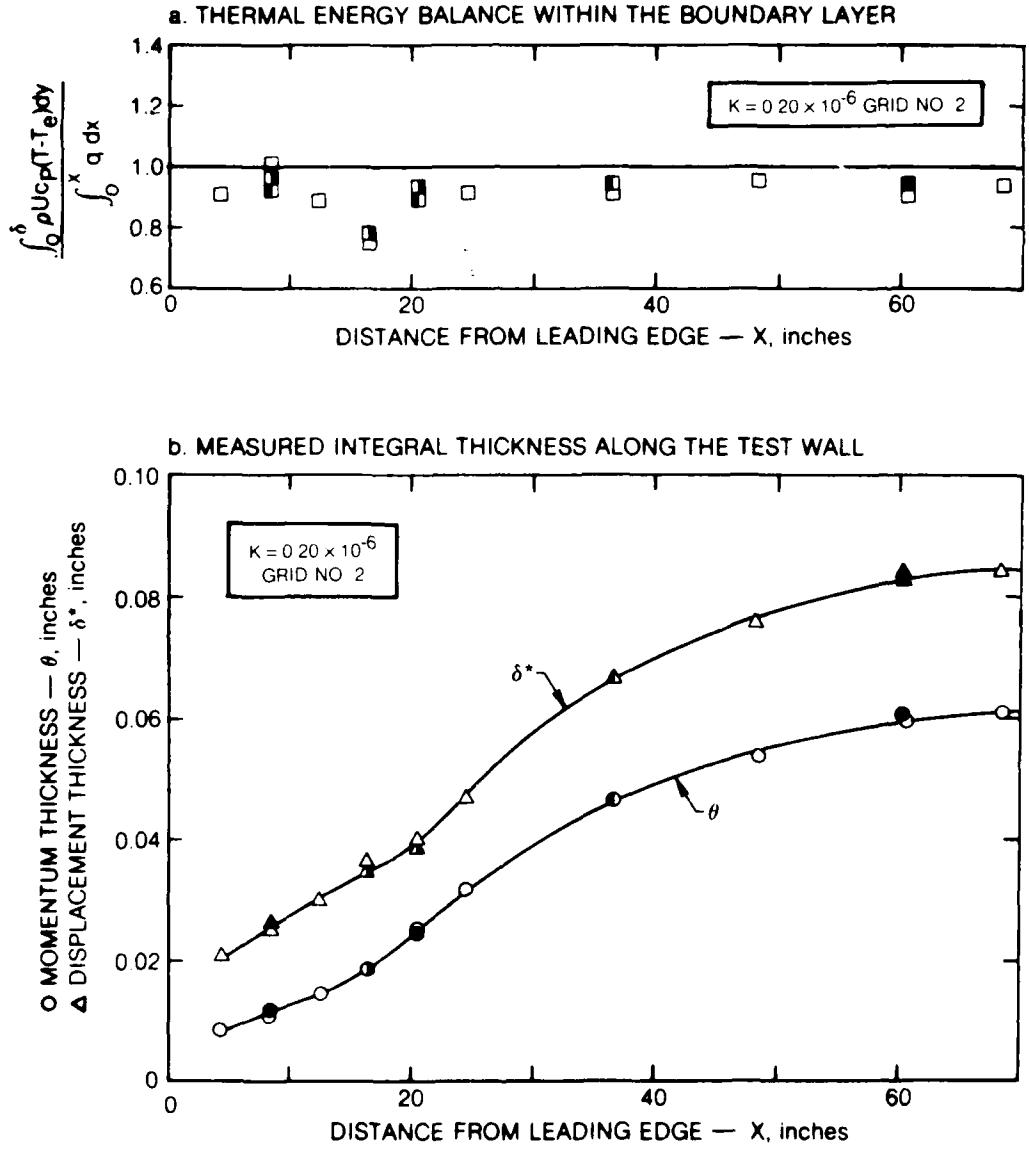

Figure 38: Boundary Layer Properties Measured With K = 0.20 x 10^{-6} And Turbulence Grid 2 ○ Tunnel C_L; ◑ Z = +6 Inches; ◐ Z = -6 Inches

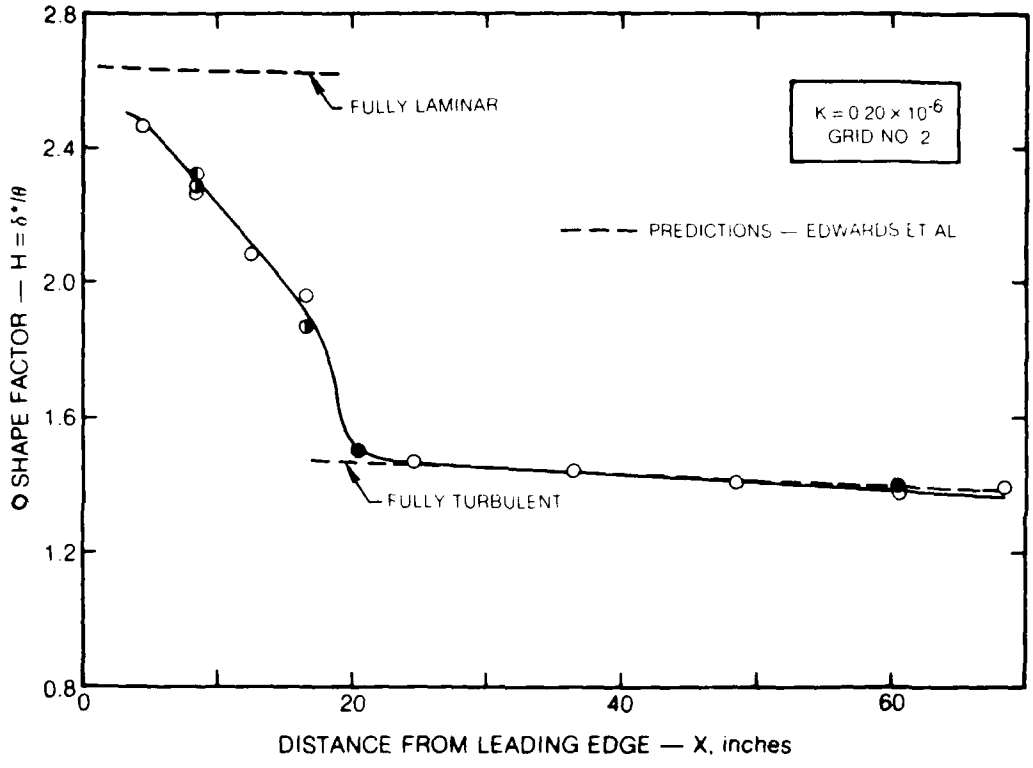

Figure 39: Boundary Layer Shape Factor Measured With K = 0.20 x 10^{-6} And Turbulence Grid 2 ○Tunnel C_L; ◑ Z = +6 Inches; ◐ Z = -6 Inches

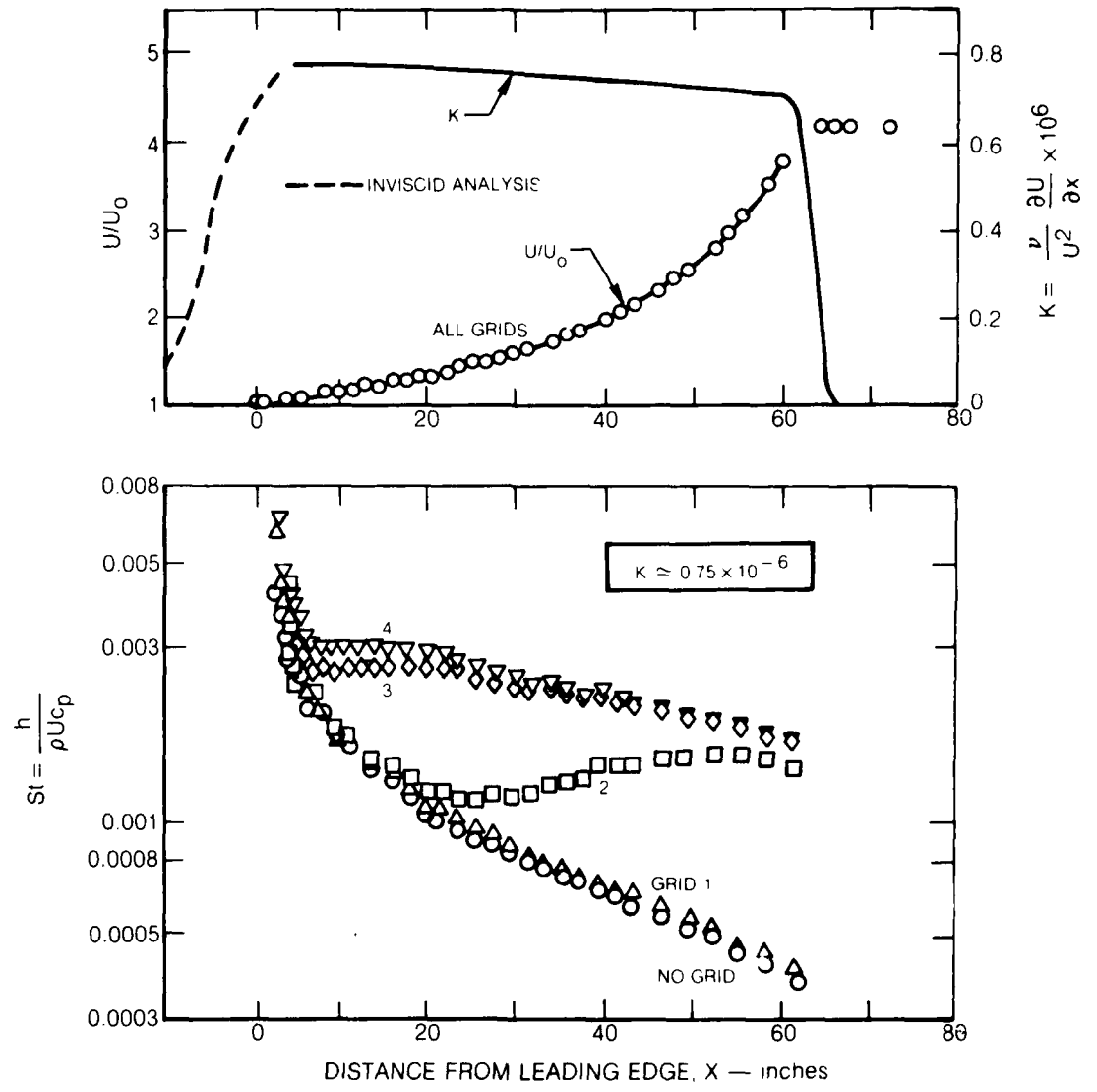

Figure 40: Acceleration and Heat Transfer Distributions For Wedge 2 and 5 Free-Stream Turbulence Levels

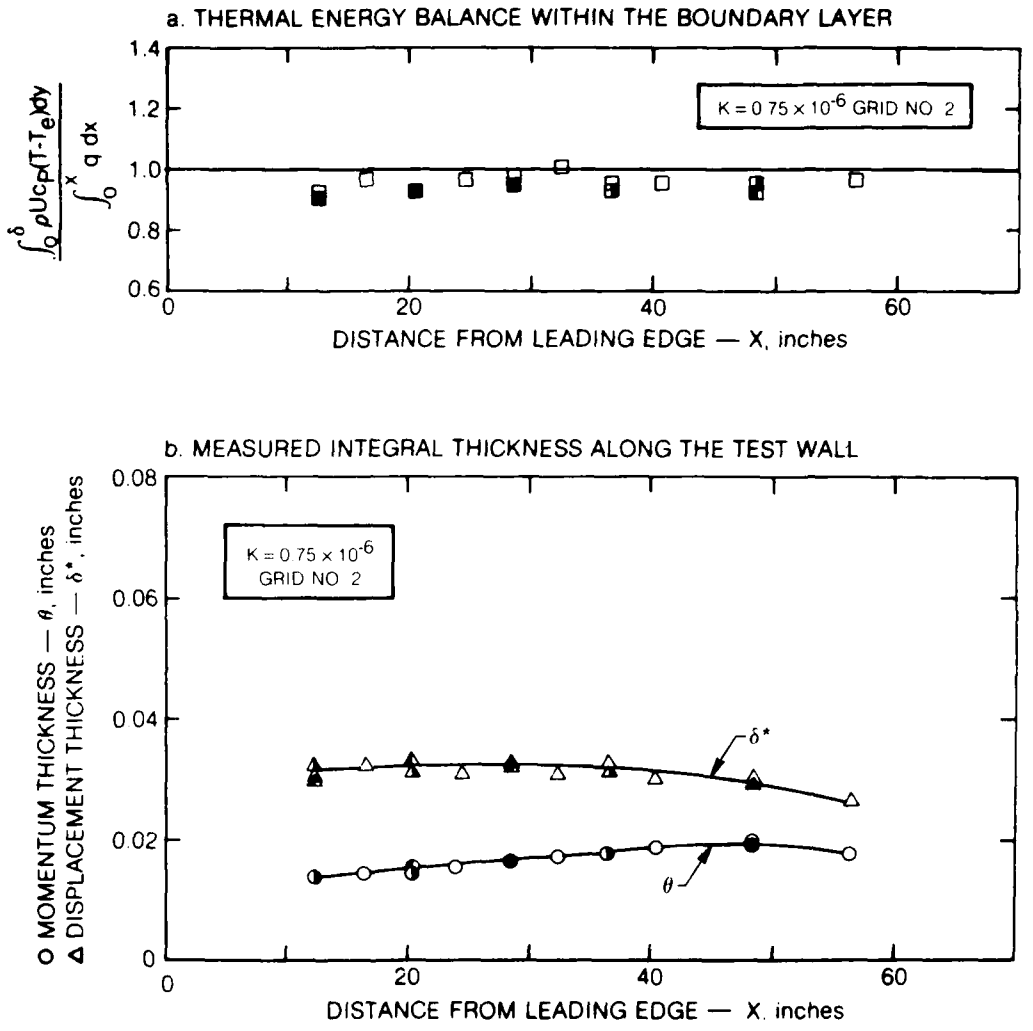

Figure 41: Boundary Layer Properties Measured With K = 0.75 x 10^{-6} And Turbulence Grid 2 ○ Tunnel C_L; ◑ Z = +6 Inches; ◐ Z = -6 Inches

81-3-1-14

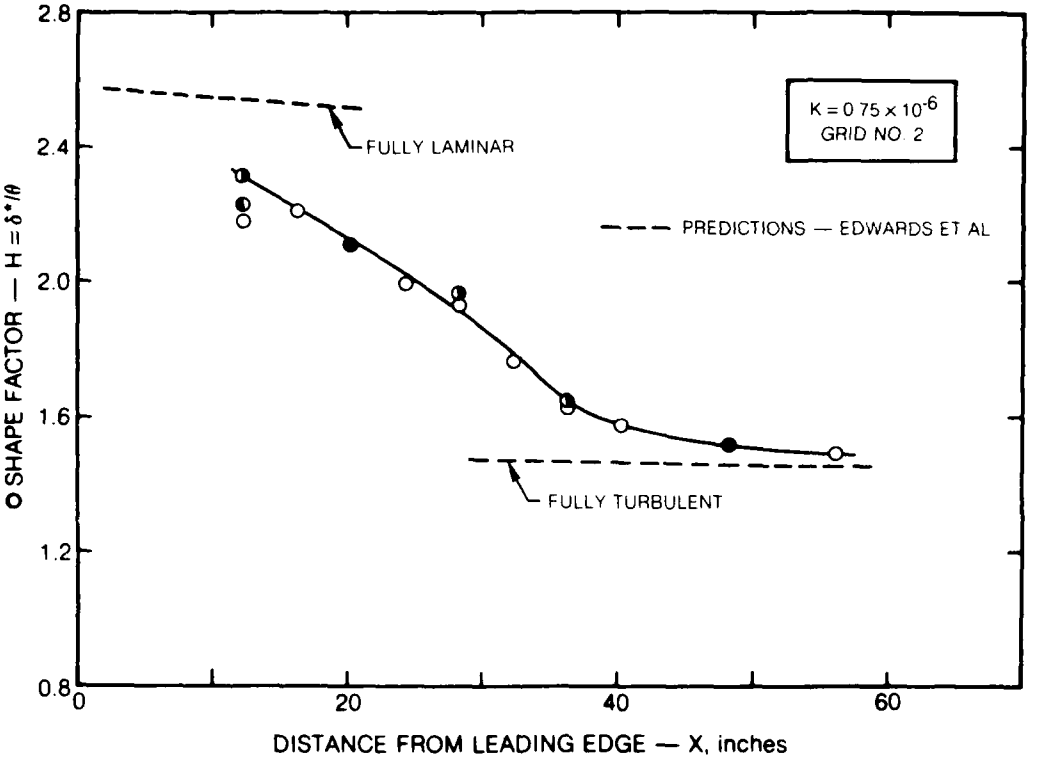

Figure 42: Boundary Layer Shape Factor Measured With K = 0.75 x 10^{-6} And Turbulence Grid 2 ○Tunnel C_L; ◑Z = +6 Inches; ●Z = -6 Inches

81-3-1-17

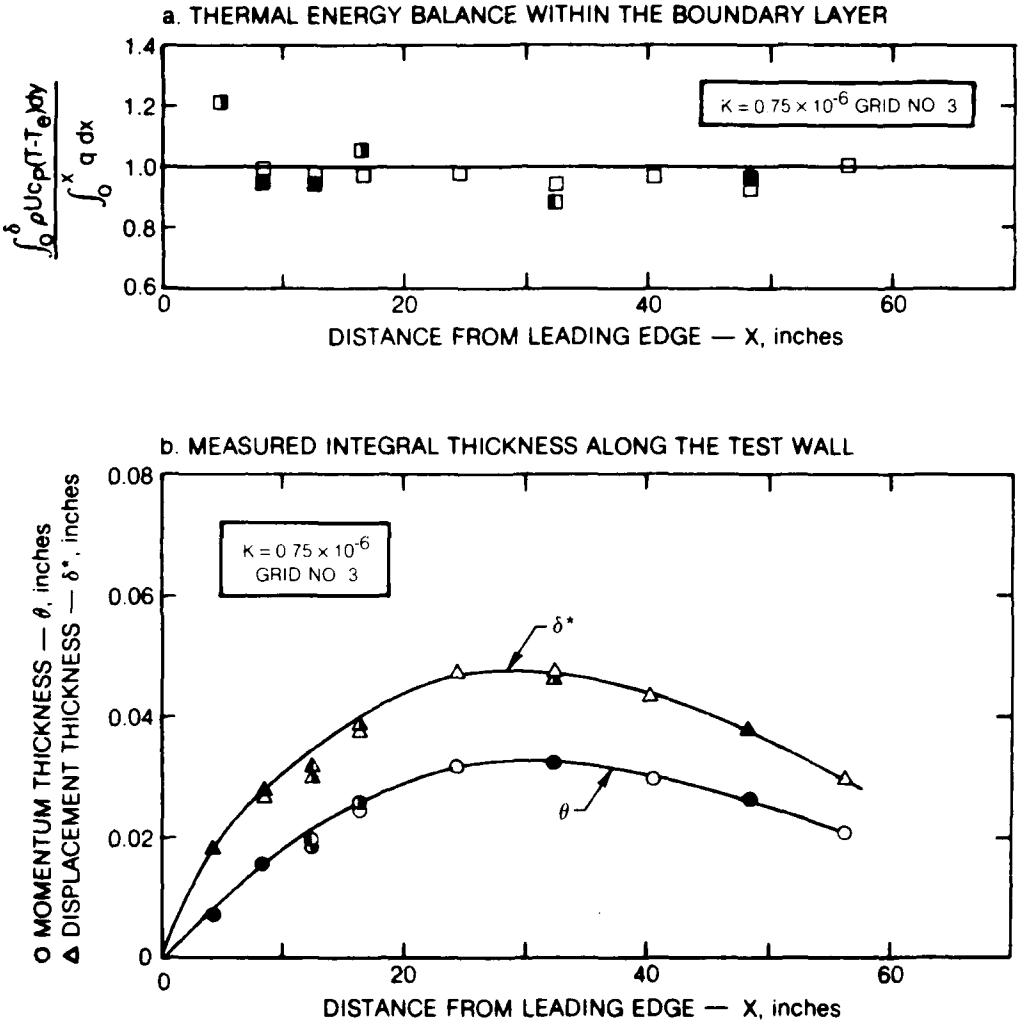

Figure 43: Boundary Layer Properties Measured With K = 0.75 x 10^{-6} And Turbulence Grid 3 OTunnel C_L; ◑Z = +6 Inches; ◐Z = -6 Inches

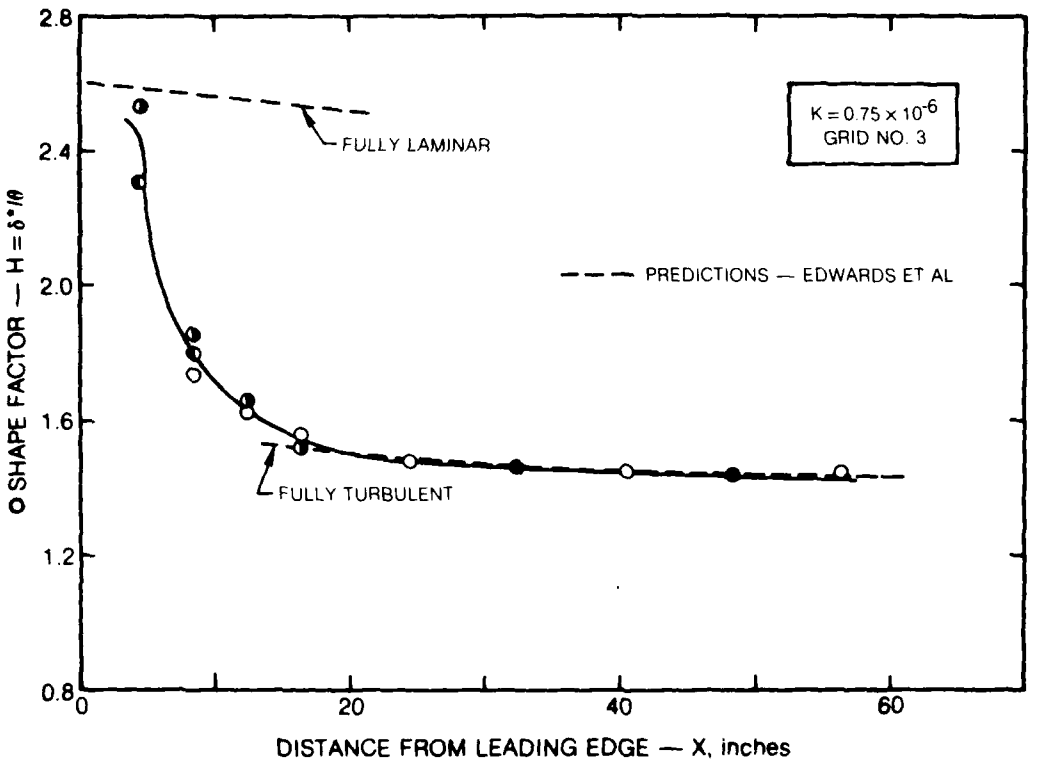

Figure 44: Boundary Layer Shape Factor Measured With K = 0.75 x 10^{-6} And Turbulence Grid 3 ○ Tunnel C_L; ◑ Z = +6 Inches; ◐ Z = -6 Inches

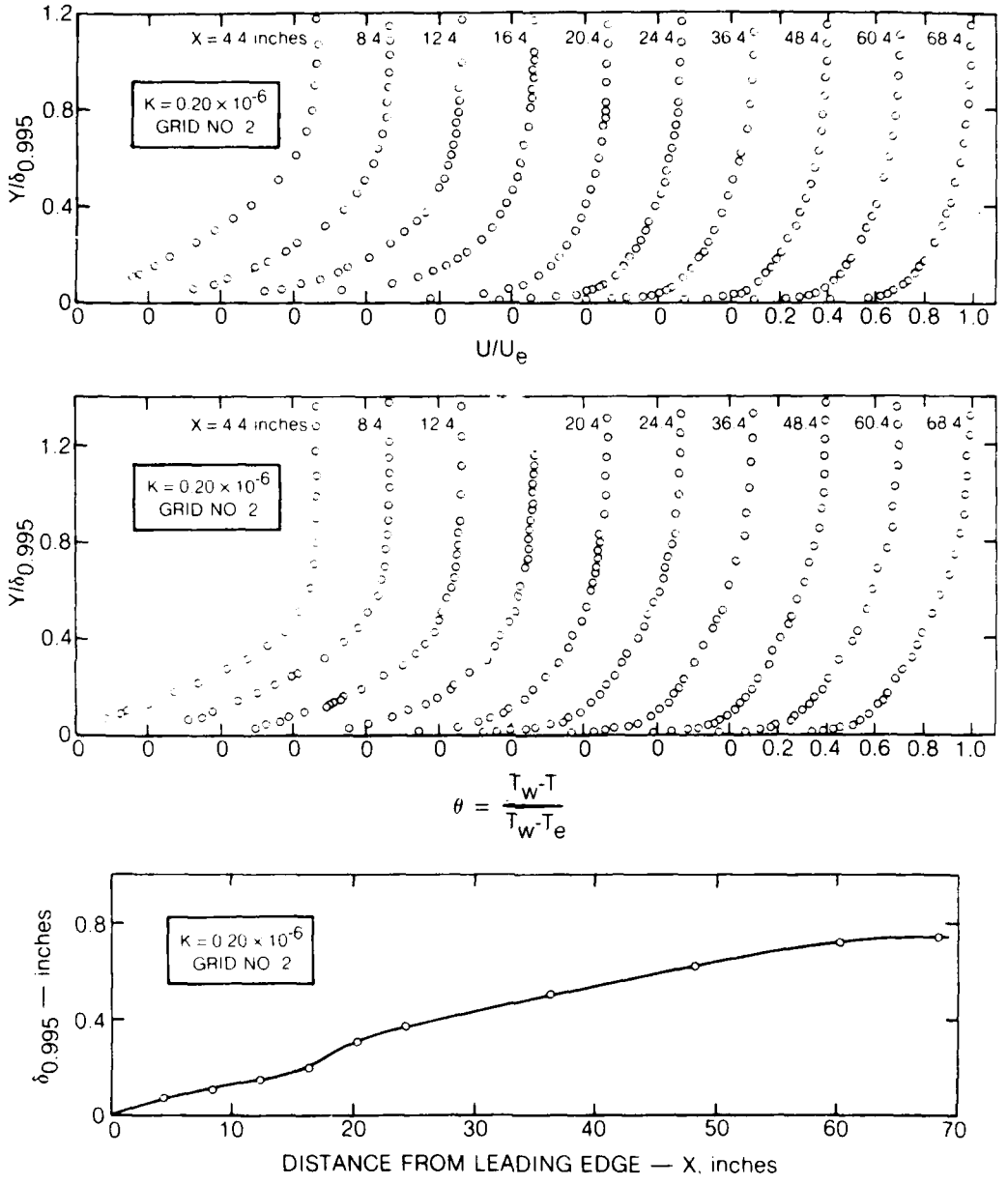

Figure 45: Development of the Mean Velocity and Temperature Boundary Layer Profiles With Distance For K = 0.20 x 10^{-6} And Grid 2

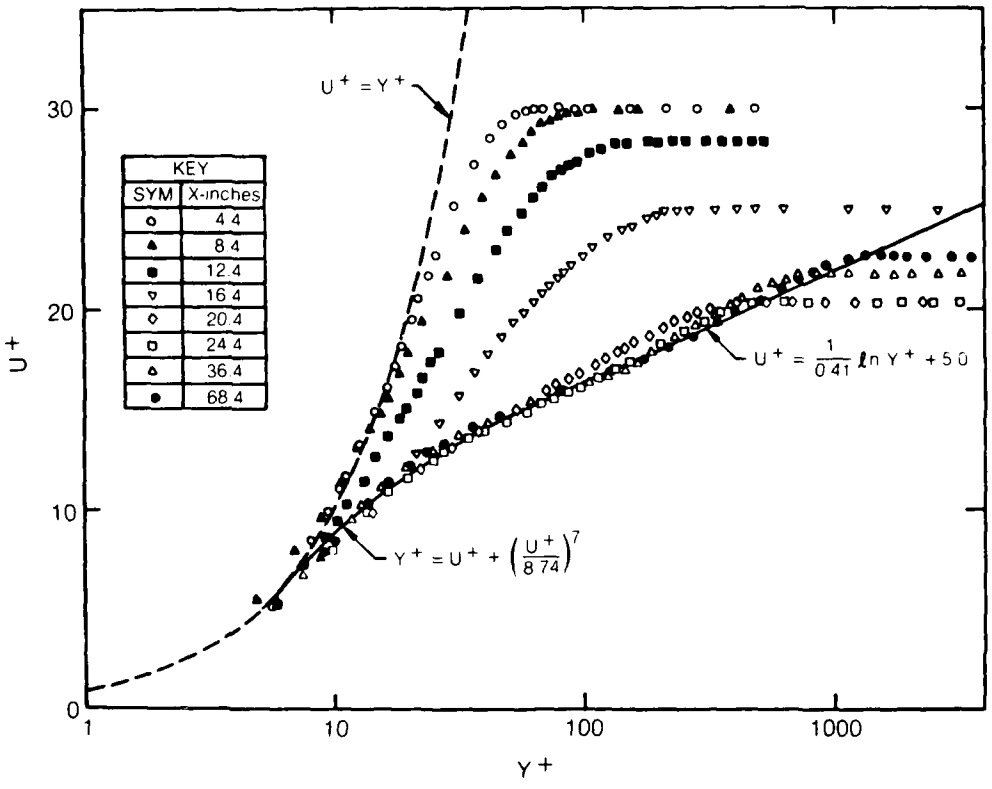

Figure 46: Development of the Mean Velocity Profiles Along the Test Wall For K = 0.20 x 10^{-6} And Grid 2 - Universal Turbulent Coordinates

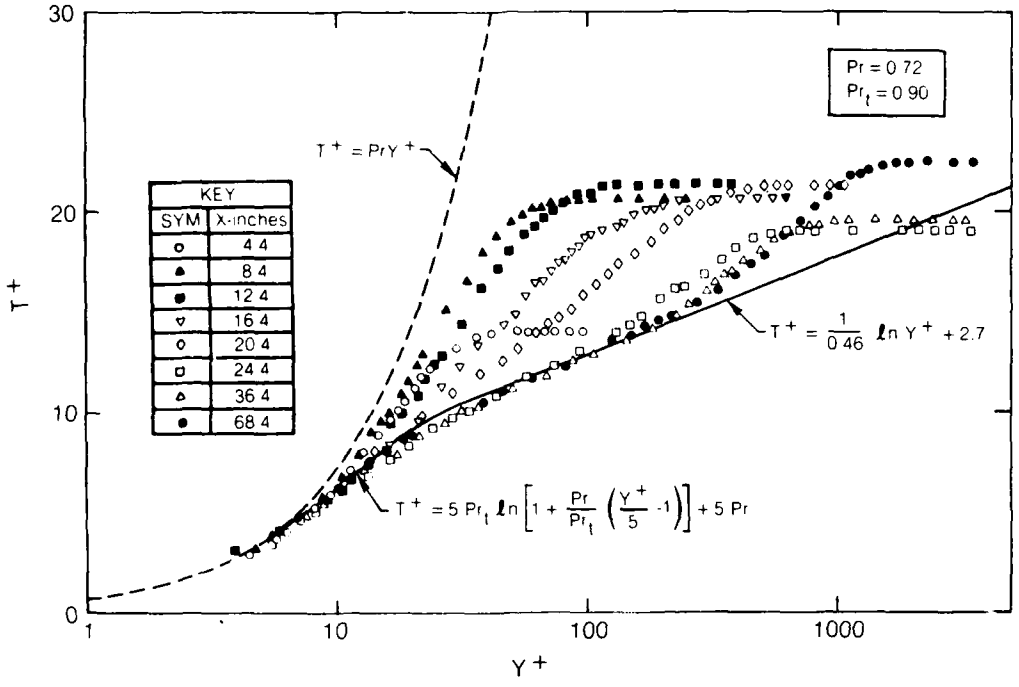

Figure 47: Development of the Mean Temperature Profiles Along The Test Wall For K = 0.20 x 10^{-6} And Grid 2 - Universal Turbulent Coordinates

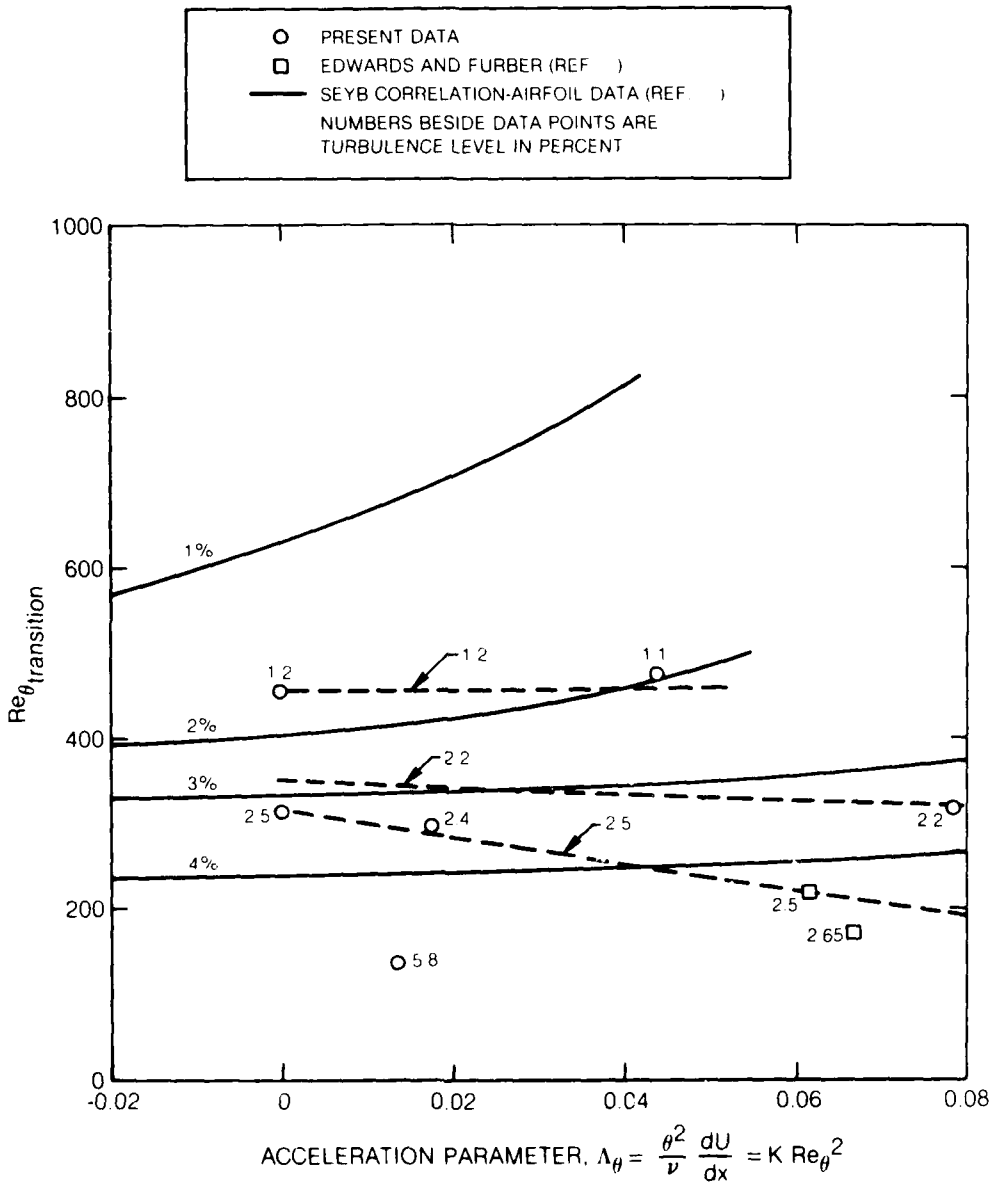

Figure 48: Combined Influence of Streamwise Pressure Gradient and Free-Stream Turbulence Intensity on Boundary Layer Transition

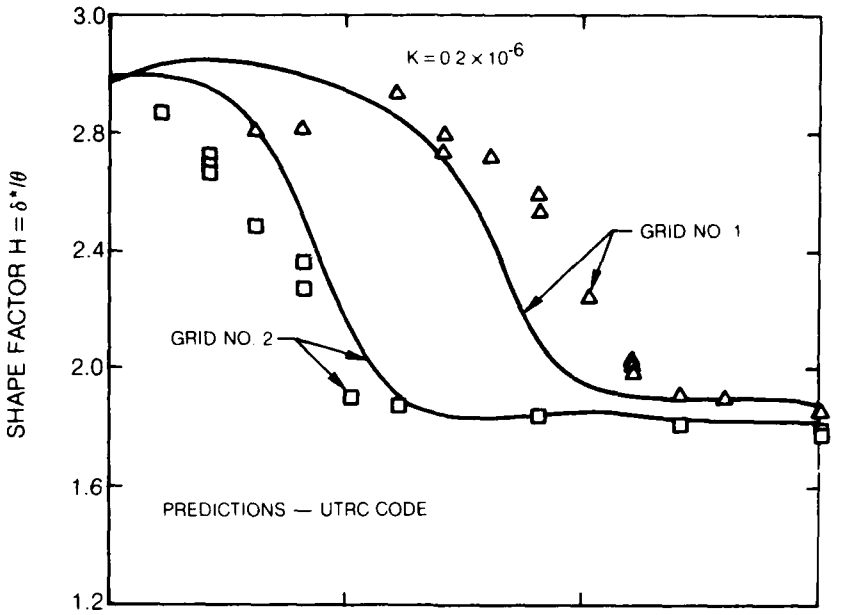

(a) PRESSURE GRADIENT NO. 1

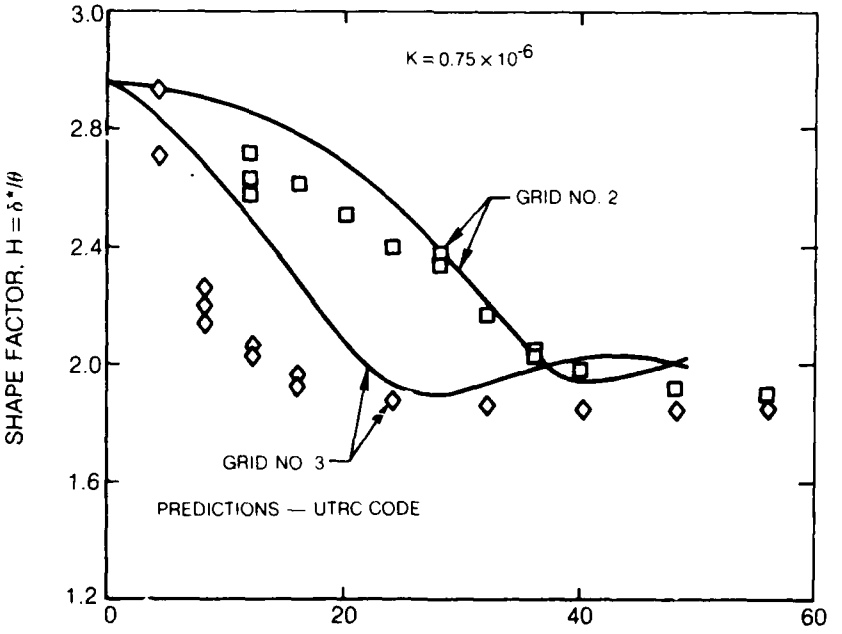

(b) PRESSURE GRADIENT NO. 2

Figure 49. Free Stream Turbulence Effects on Shape Factor

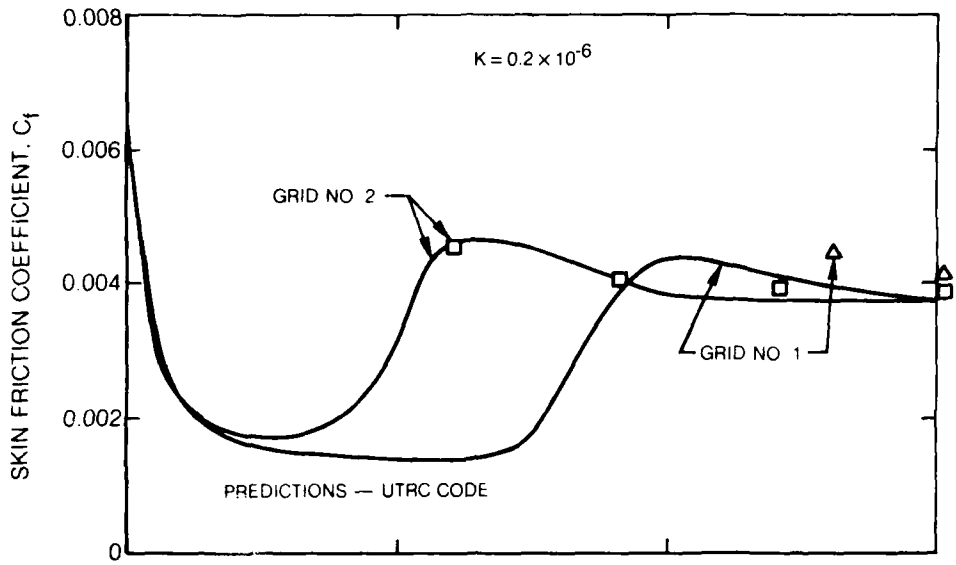

(a) PRESSURE GRADIENT NO. 1

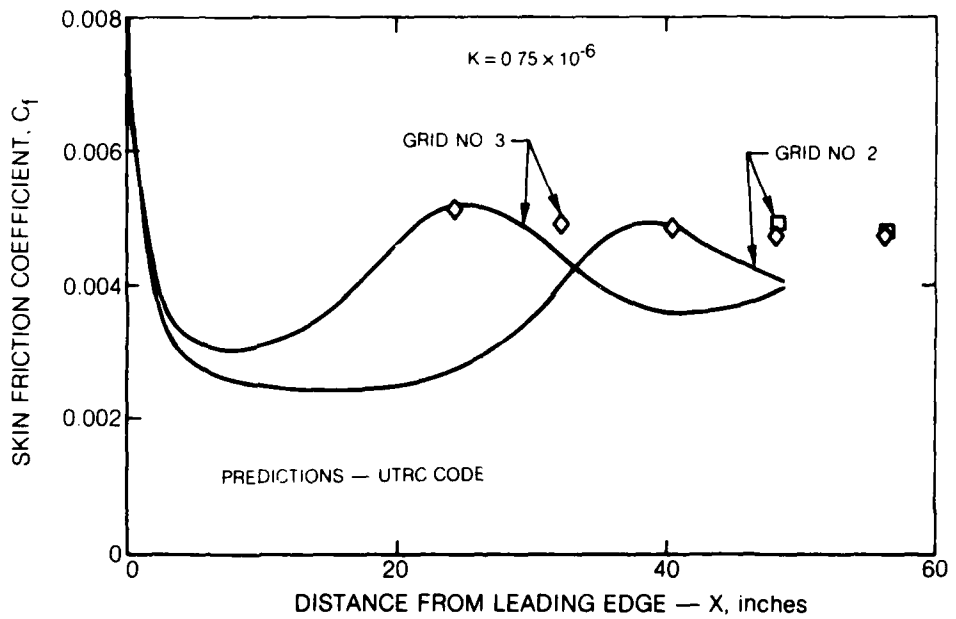

(b) PRESSURE GRADIENT NO. 2

Figure 50. Free Stream Turbulence Effect on Skin Friction

81-3-83-1

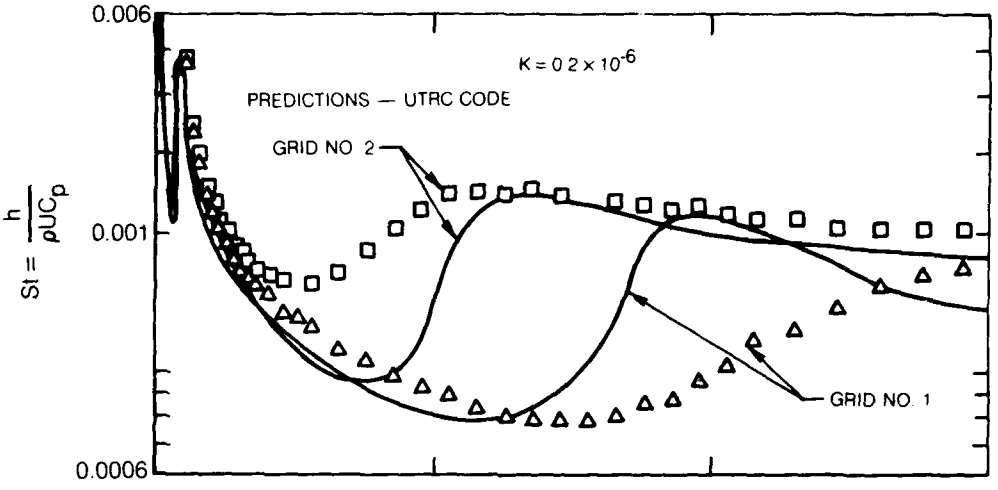

(a) PRESSURE GRADIENT NO. 1

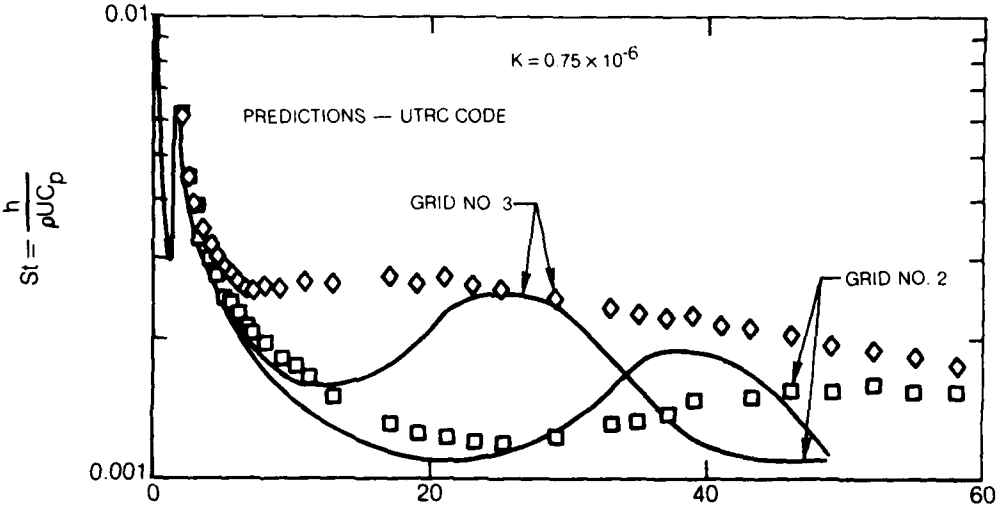

(b) PRESSURE GRADIENT NO. 2

Figure 51. Free Stream Turbulence Effect on Heat Transfer